Precision and reliability of cochlear nerve response in mice lacking functional synaptic ribbons

by

Bradley N. Buran

B.S. Physiology and Neurobiology and B.A. Anthropology
University of Maryland at College Park, 2003

SUBMITTED TO

THE HARVARD-MIT DIVISION OF HEALTH SCIENCES AND TECHNOLOGY IN PARTIAL FULFILLMENT OF THE REQUIREMENTS FOR THE DEGREE OF

DOCTOR OF PHILOSOPHY IN SPEECH AND HEARING BIOSCIENCE AND TECHNOLOGY
AT THE
MASSACHUSETTS INSTITUTE OF TECHNOLOGY

JUNE 2009

Signature of author: _____

Bradley N. Buran
Harvard-MIT Division of Health Sciences and Technology
May 18, 2009

Certified by: _____

M. Charles Liberman
Harold F. Schuknecht Professor of Otology and Laryngology, Harvard Medical School
Director of the Eaton-Peabody Laboratory, Massachusetts Eye & Ear Infirmary
Thesis Supervisor

Accepted by: _____

Ram Sasisekharan
Underwood-Prescott Professor of Biological Engineering
Director of the Harvard-MIT Division of Health Sciences and Technology

Precision and reliability of cochlear nerve response in mice lacking functional synaptic ribbons

by

Bradley N. Buran

Submitted to the Harvard-MIT Division of Health Sciences and Technology
on May 18, 2009 in Partial Fulfillment of the
Requirements for the Degree of Doctor of Philosophy in
Speech and Hearing Bioscience and Technology

Abstract

Synaptic ribbons are electron-dense structures surrounded by vesicles and anchored to the presynaptic membrane of photoreceptors, retinal bipolar cells and hair cells. Ribbon synapses are characterized by sustained exocytosis that is graded with stimulus intensity and can achieve high release rates. Leading hypotheses implicate the ribbon in maintenance of a large readily releasable pool (RRP) of presynaptic vesicles which enables rapid and precisely-timed exocytosis that supports instantaneous discharge rates of well over 1000 spikes per second.

To gain insight into the function of this specialized presynaptic molecular machinery, we characterized the response properties of single auditory nerve (AN) fibers in a mouse with targeted deletion of a presynaptic scaffolding gene, *bassoon*, in which ribbons are no longer anchored to the active zone. Since each mammalian AN fiber usually receives input from a single inner hair cell active zone to which a single ribbon is typically anchored, single-fiber recordings from bassoon mutants and control mice offer a sensitive functional metric of the contribution of individual ribbons to neural function.

Response properties of mutant AN fibers were similar, in many respects, to wild-type. Spike intervals remained irregular, thresholds were unaffected, dynamic range was unchanged, spike synchronization to stimulus phase was unimpaired, the time course of post-onset adaptation and recovery from adaptation were normal, and the ability to sustain discharge throughout a long-duration stimulus was unaffected. These data indicate that the presynaptic mechanisms which regulate precise timing of exocytosis, graded release rates and sustained neurotransmitter release were not impaired by loss of the ribbon.

However, reductions were seen in spontaneous and sound-evoked AN fiber discharge rates, coinciding with an increased variance of first spike timing to stimulus onset. Unlike fibers from wild-type mice, mutants failed to show increased peak rate as stimulus onset became more abrupt. The reduction of peak rates and increased first spike variance likely result from degraded reliability of discharge to stimulus onset via a mechanism such as reduced RRP size. Thus, the ribbon appears to support a large RRP that enables the rapid onset rates necessary for the auditory system to resolve stimulus features key for many perceptual tasks.

Thesis supervisor: M. Charles Liberman
Title: Harold F. Schuknecht Professor of Otology and Laryngology, Harvard Medical School

Contents

1 Acronyms and abbreviations used

ΔC_m	change in membrane capacitance
ABR	auditory brainstem response
AN	auditory nerve
AVCN	anteroventral cochlear nucleus
BK_{Ca}	large conductance voltage and calcium activated potassium
CAP	compound action potential
CDF	cumulative distribution function
CF	characteristic frequency
CN	cochlear nucleus
CNS	central nervous system
CtBP2	c-terminus binding protein 2
CV	coefficient of variation
DPOAE	distortion product otoacoustic emission
EM	electron microscopy
FSL	first spike latency
IHC	inner hair cell
ISI	interspike interval
LOC	lateral olivocochlear system
mEPSC	miniature excitatory post-synaptic current
mIPSC	miniature inhibitory post-synaptic current
MOC	medial olivocochlear system
MSO	medial superior olive
OHC	outer hair cell
PCR	polymerase chain reaction
PDF	probability density function
PST	post-stimulus onset time
PVCN	posteroventral cochlear nucleus
RP	refractory period
RRP	readily releasable pool
SAM	sinusoidally amplitude modulated tone
SEM	standard error of the mean
SI	synchrony index
sp/s	spikes per second
SR	spontaneous rate
SSC	semicircular canal
TH	tyrosine hydroxylase
VAT	vesicular acetylcholine transporter

2 Introduction

Synaptic ribbons are electron-dense structures surrounded by synaptic vesicles and anchored to the presynaptic membrane of hair cells, photoreceptors and retinal bipolar cells. Ribbon synapses are characterized by tonic exocytosis that is modulated by stimulus level, and are capable of sustaining high rates of exocytosis. However, the role of synaptic ribbons in neurotransmission remains unclear. Bassoon is a structural scaffolding protein found at many synapses throughout the central nervous system (tom Dieck et al., 1998; Richter et al., 1999) and appears to be required for anchoring the ribbon to the presynaptic membrane at some synapses. In a mouse with a targeted deletion of exons 4 and 5 of *bassoon*, a small fraction of synaptic ribbons remain at the active zone with most found floating freely in the cytoplasm of retinal photoreceptors (Dick et al., 2003) and hair cells (Khimich et al., 2005). In vitro studies used capacitance changes in whole-cell responses to voltage steps to infer the reduction of inner hair cell (IHC) exocytosis in these mutants (Khimich et al., 2005). Such measurements reflect the summed activity of roughly 20 afferent synapses onto each IHC, which are heterogeneous with respect to spontaneous and sound-evoked rates. Since each auditory nerve (AN) fiber receives input from a single IHC active zone to which a single ribbon is normally anchored (Liberman, 1980; Spoendlin and Schrott, 1988; Spoendlin, 1969, 1972), single fiber recordings offer a sensitive functional metric of the contribution of individual ribbons to neuronal function.

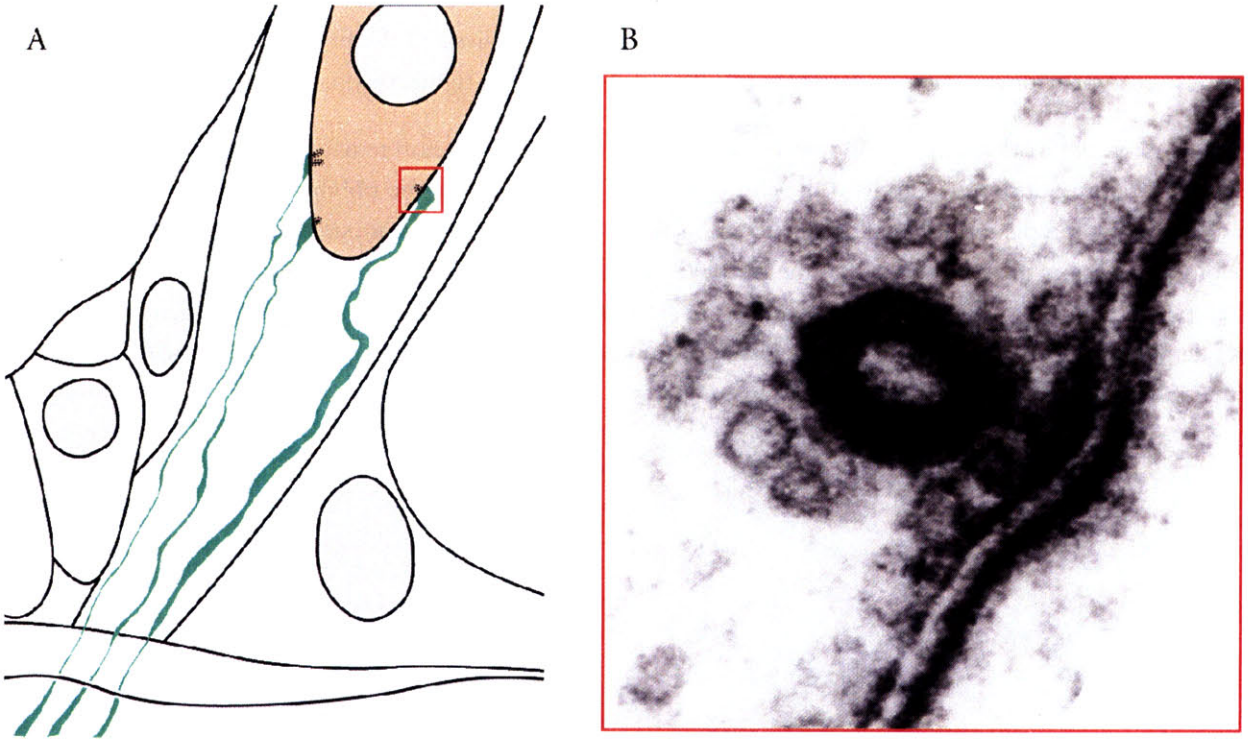

Figure 1 – A: A single AN fiber forms a single synapse with a single IHC as shown in this schematic. Only a subset of 10-20 AN fibers are shown for clarity. B: Electron micrograph of a section through an example IHC synapse. Micrograph is oriented according to the synapse highlighted by the red box in (A).

Each IHC active zone is capable of supporting extremely high rates of rapid exocytosis, driving the post-synaptic fiber at instantaneous rates of well over 1000 spikes per second (sp/s) in response to tone onset. Over a few milliseconds, this rapid exocytosis adapts into a sustained component that supports spiking

activity up to 400 sp/s. In addition to encoding intensity in firing rate, temporal fluctuations in the stimulus are encoded in the relative timing of spikes. Central auditory neurons are capable of using this precisely timed spiking activity to resolve temporal features in the acoustic signal on the order of tens of microseconds, an extraordinary feat considering the duration of an action potential is an order of magnitude longer (Bean, 2007).

Noninvasive assays of cochlear function such as auditory brainstem responses (ABR) and distortion product otoacoustic emissions (DPOAEs) are ambiguous since they reflect the summed output of cochlear generators. By sampling a subset of the population of AN fibers we can build a detailed picture of sensory transduction across the entire length of the cochlear duct. AN fibers have been well-characterized in a number of species including cat (Kiang, 1965), guinea pig (Evans, 1972) and mouse (Taberner and Liberman, 2005). The number of synapses onto each IHC varies along the tonotopic axis and between species, ranging from 5 to 30 synapses at the base of each IHC. AN fibers synapsing onto a single IHC are quite heterogeneous with respect to spontaneous rate (SR), the spiking activity that occurs in the absence of sound, and maximum driven rate. Some response properties of individual AN fibers, such as tuning, partially reflect auditory processing that arises from cochlear mechanics. However, many response properties of individual AN fibers, such as adaptation and forward masking, appear to reflect synaptic mechanisms. Some response properties are correlated with SR and may reflect underlying synaptic heterogeneity such as ribbon size (Merchan-Perez and Liberman, 1996): the ability to infer how synaptic drive is altered in the absence of the ribbon requires a representative sample across the range of SRs. Analysis of the fine timing patterns of these responses can provide insight into the processes involved in synaptic transmission.

Despite extensive work on the synaptic ribbon, its role in neurotransmission remains the subject of ongoing research. We present the first study of the contribution of individual synaptic ribbons to neuronal function using an in vivo preparation that allows us to assess synaptic function under physiologically realistic conditions. We test the hypothesis that the ribbon is required to stabilize a large readily releasable pool (RRP) by assessing AN fiber response under a variety of stimulus paradigms designed to assess RRP dynamics. Our data demonstrates a reduction in spontaneous and sound-evoked rates; however, many other response properties of AN fibers, such as spike timing, are intact.

3 Review of synaptic ribbon anatomy and physiology

3.1 Ultrastructure of ribbon synapses

Synaptic ribbons are quite diverse in shape, ranging from the uniform, spherical densities observed throughout hair cells of the saccule (Lenzi et al., 1999) to the elongate, ribbon-like structures observed in retinal bipolar cells and the horseshoe-shaped densities of rod terminals (Rao-Mirotznik et al., 1995; Sjostrand, 1958). The structure of the ribbon itself can be quite dynamic, at least in certain species, with changes in shape and size of ribbons in of cone and bipolar cells in teleosts correlated with calcium concentration or long-term fluctuations in light intensity (Vollrath and Spiwoks-Becker, 1996). Each ribbon is surrounded by a halo of 100-200 clear vesicles, each of which is connected to the ribbon by one or more thin filaments of unknown composition approximately 30 nm long (Lenzi et al., 1999).

In addition to photoreceptors, retinal bipolar cells and hair cells, ribbons have also been reported in pinealocytes (Ohshima et al., 1999), which are vestigial photoreceptors found in the pineal gland (Ekström and Meissl, 2003), as well as cutaneous receptors (Szamier and Wachtel, 1970) and electroreceptors (Szabo and Wersäll, 1970) of teleosts and skates (Sejnowski and Yodlowski, 1982). Although their classification is disputed, ribbon-like active zones have been described in the optic lamina and neuromuscular junction of invertebrates (Prokop and Meinertzhagen, 2006).

Mature IHCs of the cochlea typically have one ribbon per active zone, although up to three ribbons anchored to a single plaque have been reported in the apical region of cat and human cochleae (Merchan-Perez and Liberman, 1996; Liberman et al., 1990; Nadol, 1990). Such ribbons are roughly ellipsoid or fusiform in shape, ranging from 210 to 600 nm in length and 55 to 120 nm in width and height, with an inverse correlation between ribbon size and level of spontaneous activity (Merchan-Perez and Liberman, 1996). In contrast, ribbons are extremely rare at the afferent synapses of mature outer hair cells (OHCs) above the 1 kHz place in cat (Dunn and Morest, 1975; Liberman, 1980), although they appear to be much more common in humans, appearing at 35% of synaptic contacts (Nadol, 1990). The significance of the absence of the ribbon at many OHC afferent synapses is not clear: remaining ribbons may have some role in auditory function or simply reflect vestigial remnants of a specialized hair cell. AN fibers that innervate OHCs are unmyelinated, suggesting that they do not sustain the high rates of discharge (Quandt and Davis, 1992) or precisely timed spiking activity supported by their myelinated counterparts that innervate IHCs.

The synaptic circuitry of mammalian retina is more complex: a single retinal bipolar cell synapses onto multiple cone photoreceptors. Each photoreceptor, in turn, receives synapses from multiple bipolar cells (Sterling et al., 1988). Multiple bipolar cells converge onto a single retinal ganglion cell, which serves as the conduit from the retina to the central nervous system (CNS). Mammalian rod photoreceptors typically have a single ribbon which supplies up to four postsynaptic processes (Rao-Mirotznik et al., 1995, 1998), while cone photoreceptors contain many more ribbons (e.g. 11.6 ribbons/cell in cone receptors of the cat fovea) whose number varies with retinal location and species (Sterling, 2004).

While the conventional SNARE proteins integral to the exocytotic machinery of synaptic vesicles – SNAP-25, syntaxin 1 and synaptobrevin 1 – are expressed in IHCs (Safieddine and Wenthold, 1999), a number of other common synaptic proteins are absent throughout ribbon synapses. Of note is the lack of synapsins, a

class of proteins involved in synaptic vesicle mobilization, and synaptotagmins 1 and 2, which are calcium sensors involved in synaptic vesicle fusion ubiquitous throughout the CNS (Sudhof, 2004). This may indicate that there are isoforms of synapsins and synaptotagmins that have not been described yet, or that ribbon synapses utilize alternate mechanisms of vesicle priming and release. Otoferlin, which binds calcium and interacts with SNARE proteins, has been proposed as a putative calcium sensor at auditory ribbon synapses (Roux et al., 2006; Beurg et al., 2008).

A number of proteins are reported to be part of the molecular composition of the ribbon including RIM (Wang et al., 1997), which interacts with Rab3, a GTPase expressed on synaptic vesicles, and RIBEYE (tom Dieck et al., 2005), the only unique component of the ribbon to date. RIBEYE is a fusion of two domains, one unique to ribbons and the other identical to C-terminal-binding protein 2 (CtBP2), a transcriptional repressor related to 2-hydroxyacid dehydrogenases (Schmitz et al., 2000) which binds NAD^+ with high affinity. Some interesting hypotheses regarding the role of the ribbon have been proposed based on the presence of these proteins, such as a potential role in synaptic vesicle filling or priming based on motifs found in RIBEYE. Immunostaining evidence for KIF3A, a kinesin motor protein, led to the suggestion that the ribbon might be involved in active transport of synaptic vesicles to the membrane (Muresan et al., 1999; Parsons and Sterling, 2003) with the studded surface serving as an alternate substrate for KIF3A in the absence of any evidence for the presence of microtubule proteins (Usukura and Yamada, 1987). However, even in the presence of ATPγS, which does not support ATP-dependent motors such as kinesin and myosin, the full complement of synaptic vesicles are released in retinal bipolar cells with normal kinetics (Heidelberger et al., 2002).

Despite evidence that vesicle release occurs outside the zone of the ribbon, the synaptic structure appears specialized for transmission at the base of the ribbon itself. Immunogold labeling demonstrates that AMPA and NMDA receptors cluster at the postsynaptic density immediately opposite the ribbon synapse in cochlear hair cells (Matsubara et al., 1996). Live-cell imaging demonstrates hotspots of calcium influx at sites labeled with antibodies against RIBEYE (Zenisek et al., 2003) and CtBP2 (Zenisek et al., 2004), consistent with immunohistochemistry that demonstrates clustering of calcium channels at the base of ribbons (Brandt et al., 2005). Freeze-fracture EM reveals roughly 125 particles clustered at the base of the ribbon which appear to correspond with ~90 calcium and ~40 calcium-activated potassium channels in bullfrog saccular hair cells (Roberts et al., 1990).

The synaptic ribbon is covered by a monolayer of vesicles, many of which are physically tethered to it by a thin filament of unknown composition and function (Lenzi et al., 1999). Photobleaching experiments can be used to assess whether these tethered vesicles are mobile. By labeling the population of synaptic vesicles in the terminal with a dye and using a laser to selectively inactivate (i.e. photobleach) the dye in a small region, mobility can be assessed by observing the rate at which fluorescence recovers in that region as bleached vesicles are replaced with labeled ones. Such experiments reveal that ribbon-associated vesicles are tightly associated with the structure; however, under depolarizing conditions they have a much greater mobility and may participate in the RRP or exchange with cytoplasmic vesicles (LoGiudice et al., 2008). Further support come from total internal reflection microscopy, which eliminates the background generated by a cloud of fluorescently labeled vesicles by restricting excitation to a narrow ~100 nm thick slice immediately adjacent to the plasma membrane. This technique can be used to visualize the dynamics of vesicles immediately adjacent to the membrane. In bipolar cells, vesicles appear to preferentially dock near the ribbon, with vesicles at the

base of the ribbon being highly stable (i.e. motionless) over the course of several seconds at resting membrane potentials before rapidly being released in response to depolarization (Zenisek, 2008). In contrast, similar experiments in hair cells (Holt et al., 2004) and retinal photoreceptor terminals (Rea et al., 2004) suggest that the vesicles not tethered to the ribbon are highly mobile, consistent with the lack of synapsin which typically anchors vesicles to the cytoskeleton at many central synapses, and tend to dock intermittently at the membrane.

Comprehensive electron microscopy (EM) studies suggest that the population of synaptic vesicles at ribbon terminals can be grouped into several categories based on their relationship to the synaptic membrane and the ribbon (Lenzi et al., 1999), although the functional significance of these classifications remains a matter of debate.

- Docked-and-tethered – Consisting of the population of vesicles found at the base of the ribbon, which positions them in close proximity to multiple calcium channels and likely facilitates rapid exocytosis.
- Docked-but-not-tethered – A population of outlying vesicles that are not associated with the ribbon itself and rest somewhat further from calcium channels (up to 1000 nm from the ribbon). These vesicles may contribute to sustained exocytosis as calcium influx builds up sufficiently to drive neurotransmitter release at sites further from the ribbon.
- Tethered-but-not-docked – This population of vesicles may be involved in ribbon-mediated compound fusion (Matthews and Sterling, 2008) or serve as a reserve pool that replenishes the pool of docked vesicles at the base of the ribbon.
- Outlying vesicles – A cloud of vesicles floating freely in the cytoplasm that likely resupplies the other vesicle pools via diffusion.

3.2 Neurotransmitter release at the ribbon synapse

Unlike conventional synapses, transmitter release at ribbon synapses appears to be regulated by L-type voltage-gated calcium channels, a heterogeneous class characterized by slow inactivation and sensitivity to dihydropyridines (Lipscombe et al., 2004). The functional properties of different types of L-type calcium channels are primarily determined by expression of specific $\alpha 1$ subunits (Catterall, 2000). Two $\alpha 1$ subunits, $Ca_v1.3$ and $Ca_v1.4$, which share a high degree of homology, are found at hair cell and retinal bipolar cell synapses, respectively. In contrast to other L-type calcium channels, $Ca_v1.3$ and $Ca_v1.4$ are far less sensitive to dihydropyridines, have low activation thresholds and demonstrate very rapid activation kinetics on the order of 100 to 500 μs (Zidanic and Fuchs, 1995). There is some indication from bullfrog saccular hair cells that non L-type channels may be present as well (Rodriguez-Contreras and Yamoah, 2001). T-type calcium channels, which rapidly inactivate over the course of a few milliseconds, have been reported in the inner ear; however, it remains unclear whether these channels are expressed in hair cells, let alone localized to the ribbon synapse itself (Inagaki et al., 2008; Nie et al., 2008).

Whole-cell patch clamp techniques can be used to measure the membrane capacitance of isolated cells. The fusion of synaptic vesicles with the membrane increases the surface area, thus increasing the capacitance of the cell. Since retrieval of this membrane is relatively slow with a time constant of 7.5 s in hair cells (Moser and Beutner, 2000) and 1.3 s in retinal bipolar cells (von Gersdorff and Matthews, 1994), the increase in membrane capacitance on shorter time scales ($\leq$ 1 s) are considered a direct measure of exocytosis.

Exocytosis is typically induced by depolarizing voltage steps, which cause voltage-gated calcium channels to open, thus driving exocytosis. The number of synaptic vesicles which fused with the membrane during this depolarizing step can be inferred by immediately measuring the change in membrane capacitance (i.e. ΔC_m) following the voltage step. The change is then divided by the estimated capacitance of a single vesicle. Single vesicle capacitance is typically determined from the surface area of the vesicle as estimated from EM studies and ranges from ~24-37 aF (Lenzi et al., 1999; Moser and Beutner, 2000; Khimich et al., 2005). Since ΔC_m reflects the total number of synaptic vesicles exocytosed, the rate of change of ΔC_m reflects the rate of exocytosis, commonly expressed as vesicles/s. Estimates of the rate of exocytosis at ribbon synapses vary widely, ranging from 500 vesicles/s/synapse in retinal bipolar cells (von Gersdorff et al., 1996) to 2,000/s/synapse in IHCs (Moser and Beutner, 2000) and may possibly be as high as 5,000/s/synapse (Khimich et al., 2005). In contrast, maximal rate of release at a single hippocampal synapse is only 20/s (Stevens and Tsujimoto, 1995). However, measurement of ΔC_m often is very coarse and the assumptions used to determine the quantal size of exocytosis vary significantly, making such estimates a rough approximation of actual release rates.

Measures of ΔC_m reveal two phases of exocytosis, a rapid component that plateaus within 10 ms and a slower component that persists over several hundred milliseconds in retinal bipolar cells (Mennerick and Matthews, 1996; von Gersdorff and Matthews, 1994) and IHCs (Moser and Beutner, 2000). The rapid component appears to correspond with a small pool of 21 vesicles/ribbon in bipolar cells (Mennerick and Matthews, 1996), consistent with the number of vesicles anchored to the base of the ribbon (i.e. docked-and-tethered) as assessed by EM studies (von Gersdorff et al., 1996), and 18 to 64 vesicles/ribbon in IHCs released over 10 ms (Moser and Beutner, 2000; Khimich et al., 2005) [1]. Since the size of the rapid component is not affected by high concentrations of the slow calcium chelator, EGTA, which restricts the diffusion of calcium to vesicles not docked near the calcium channels, this component is believed to correspond with vesicles docked immediately adjacent to calcium channels (Moser and Beutner, 2000).

The nature of the slower component of exocytosis is less clear. In retinal bipolar cells it saturates after approximately 150 ms (von Gersdorff and Matthews, 1994), reflecting the complete exhaustion of a release-ready pool of 6,000 vesicles (110 per ribbon, 54 ribbons per cell). This estimate compares well with the number of ribbon-anchored vesicles reported in EM studies[2] (von Gersdorff et al., 1996) and led to the suggestion that the sustained component reflects mobilization of vesicles tethered to the synaptic ribbon (von Gersdorff, 2001). Although this suggests that vesicles tethered to the ribbon may constitute the RRP, analogous studies in IHCs indicate that the number of vesicles released prior to saturation of membrane capacitance is ten times larger than the number of ribbon-tethered vesicles (Eisen et al., 2004) and likely includes the release of vesicles not anchored to the ribbon. A significant component of the slow component

[1] The large range of estimates appear to arise from combined experimental error including difference in the estimate of the capacitance of a synaptic vesicle (37 aF for the former study versus 28 aF for the latter) and a slightly larger ΔC_m in the latter study.

[2] Such coincidences need to be interpreted with extreme caution, particularly when the numbers from the physiology and morphology correspond extremely well. Considering the large margin of error in estimating parameters such as single-vesicle capacitance, ribbon packing density, ribbon surface area, etc. it is possible to select "reasonable" numbers based on the data that give the answer one wishes to see (e.g. single vesicle capacitance values vary as much as 30% across studies).

of release may be dependent on diffusion of calcium to vesicles anchored far from calcium channels (Neher, 1998; Voets et al., 1999), at least in hair cells. This work is supported by total internal reflection fluorescence microscopy which demonstrates neurotransmitter release in regions far from the ribbon (Zenisek et al., 2003) as well as EM tomography of hair cell synapses, which show uniform depletion of vesicles docked at the plasma membrane regardless of distance from the ribbon in saccular hair cells (Lenzi et al., 2002). In contrast to exocytosis in retinal bipolar cells, which saturates after 150 ms in response to a strong depolarization, analogous measurements in IHCs show sustained exocytosis of up to at least 1 s with no evidence of exhaustion, reflecting an exocytotic rate of 6,030 vesicles/s (241/s/synapse). Despite these two competing hypotheses, one thing is clear: the slow component is significantly reduced by EGTA in both bipolar cells (Mennerick and Matthews, 1996) and hair cells (Moser and Beutner, 2000).

Tall hair cells[3] of the chick cochlea also show a component of exocytosis that saturates by 50 ms, corresponding with 1,000 vesicles per cell, an estimate that agrees well with the 984 vesicles (41 vesicles/ribbon, 24 ribbons/cell) estimated from morphological data (Spassova et al., 2004). Since the authors did not assess exocytosis for durations shorter than 50 ms[4], it is not clear how to compare these results to data from retinal bipolar cells and mammalian IHCs since the saturation of exocytosis by 50 ms may reflect a "slower" rapid component or a more "rapid" saturation of the sustained component of exocytosis. Regardless of these caveats, the release of 41 vesicles/ribbon within 50 ms is consistent with estimates of the number of vesicles released in the first 10 ms in bipolar cells and IHCs.

The calcium sensor in IHCs appears to require the cooperation (i.e. simultaneous binding) of 3 to 5 calcium ions to initiate vesicle release (Beutner et al., 2001; Goutman and Glowatzki, 2007). When multiple ions are required to drive exocytosis, the spatial relationship between the calcium sensor and nearby calcium channels determines the relationship between calcium channel opening and rate of exocytosis. Influx from a single calcium channel creates a nanodomain of extremely high calcium concentration sufficient to drive exocytosis of synaptic vesicles in the immediate vicinity ($\leq$ 50 nm). For vesicles docked further away, but within a fraction of a micrometer from a cluster of calcium channels, the spatial summation of influx from several of these channels is required to create a microdomain of sufficiently high concentration to drive exocytosis (for review, see Augustine et al., 2003). A nanodomain implies a linear relationship between $Ca_v1.3$ open probability and rate of exocytosis as recruitment of additional calcium channels would drive exocytosis of additional vesicles, while a microdomain model would have a power-law relationship since vesicle release depends on the probability of multiple channels opening simultaneously. Consistent with a nanodomain release model where the opening of one or a few calcium channels is sufficient to saturate the calcium sensor of a nearby vesicle, exocytosis is linearly correlated with modulation of calcium channel open probability using dihydropyridines to selectively inactivate a fraction of the pool of $Ca_v1.3$ channels (Brandt et al., 2005). Over the range of physiologically relevant IHC receptor potentials, the resulting calcium influx is linearly correlated with the post-synaptic current (Keen and Hudspeth, 2006; Goutman and Glowatzki, 2007).

[3] These cells are also known as neural cells and are considered the avian homologue of mammalian IHCs.

[4] A review paper suggested that the failure to assess exocytosis over shorter time scales may be due to the amplitude of the rapid component being so small that it is difficult to detect in these cells (Nouvian et al., 2006).

Patch-clamp recordings of hair cell afferent boutons reveal a range of highly variable miniature excitatory post-synaptic current (mEPSC) amplitudes up to a maximum of 800 pA. Interestingly, the modal mEPSC is 30 pA, which is consistent with the single-vesicle mEPSC observed at CNS synapses (Glowatzki and Fuchs, 2002). Although this mEPSC variability is attributed to coordinate multivesicular release, it is not clear whether it might be due to the simultaneous fusion of multiple vesicles with the membrane or homotypic fusion occurring before or during exocytosis (Parsons and Sterling, 2003), or even a mixture of both. In addition to the reported variability in amplitude, mEPSCs also appear to be heterogeneous with respect to shape, with local plateaus and peaks observed in individual traces presumably corresponding with imprecise temporal coordination of multivesicular release (Keen and Hudspeth, 2006). While an interesting proposal, there is little evidence for homotypic fusion in IHCs to date (but see Matthews and Sterling, 2008), although compound fusion appears to occur at the calyx of Held in the brainstem (He et al., 2009). There is, however, an inverse relationship between quantal size and rate, suggesting that accumulation of glutamate and potassium in the cleft may be an alternate source of observed quantal variability (Holt et al., 2006). Similar variable, large amplitude miniature inhibitory post-synaptic currents (mIPSCs) observed in Purkinje cells are also believed to be due to multivesicular release, and are regulated by intracellular ryanodine-sensitive calcium transients (Llano et al., 2000). Similar ryanodine-sensitive calcium-induced calcium release has been described in IHCs (Kennedy and Meech, 2002), but the role in release is unclear. Since the smallest mEPSCs observed, presumably corresponding to the release of a single vesicle, appear sufficient to elicit a spike outside of the refractory period (Siegel, 1992), multivesicular release could be used to drive spiking activity during the relative refractory period or enhance temporal precision (see section 6.2.2).

3.3 Presynaptic scaffolding protein bassoon

Bassoon is one of the largest proteins associated with the cytomatrix at the active zone identified to date ($\geq$ 400kD). The protein is localized at the active zone of excitatory (glutamatergic) and inhibitory (GABAergic) synapses throughout the CNS (Richter et al., 1999; Dick et al., 2003) where it interacts with other scaffolding proteins (Schoch and Gundelfinger, 2006). In retinal photoreceptors it localizes to the arciform density (Dick et al., 2003). Mice with a targeted deletion of exons 4 and 5 of *bassoon*, the central region involved in anchoring the ribbon to the cytomatrix at the active zone, have a larger fraction of inactive excitatory hippocampal synapses despite such synapses being indistinguishable from wild-type at the ultrastructural level (Altrock et al., 2003). However, the N-terminal zinc finger motif and C-terminal coiled-coil domain are still expressed and continue to be localized to the active zone (Leal-Ortiz et al., 2008). Only a very small fraction of synaptic ribbons remain present at active zones, with most found floating freely in the cytoplasm of retinal photoreceptors and hair cells; however, ribbon synapses appear intact in bipolar cells (Dick et al., 2003) which do not express Bassoon (Brandstatter et al., 1999). Abnormalities consistent with a deficiency in synaptic transmission are observed in electroretinograms (Dick et al., 2003). In vitro patch clamp recordings of isolated IHCs deficient for bassoon demonstrate a reduction in both the calcium current and ΔC_m (Khimich et al., 2005). Exocytosis remains deficient even when calcium current in mutant mice was increased to near wild-type levels by increasing extracellular calcium concentration. Bassoon-deficient mice also display abnormal brain structure and imbalanced patterns of brain activity that appear to result in epileptic seizures (Angenstein et al., 2008, 2007).

3.4 Summary and Significance

Various functional roles for the synaptic ribbon have been proposed based on morphological data and in vitro physiology. Evidence from whole-cell patch clamp measurements suggest that the ribbon may facilitate rapid exocytosis, possibly by stabilizing a large RRP at the base of the ribbon in the immediate vicinity of calcium channels. Through such a mechanism, the ribbon could support the precisely timed and reliable exocytosis required for temporal coding in mammalian AN fibers. Alternate hypotheses implicate the ribbon in resupply of the RRP, which may contribute to the ability of the synapse to maintain high rates of exocytosis over long-duration depolarizations.

Results from in vitro physiology, however, are difficult to interpret as they reflect the summed response of many synaptic ribbons and necessitate destroying cochlear function. Single-unit recording, on the other hand, offers a sensitive metric of the contribution of a single ribbon to the response of a single AN fiber. Many hypotheses of synaptic ribbon function can be addressed using appropriately crafted stimulus paradigms. Long-duration tone bursts can be used to reveal dynamics of sustained exocytosis while forward masking paradigms can be used to assess resupply of the RRP. Central to many discussions of the ribbon are its role in spike timing precision and reliability: by using acoustic stimuli designed to generate temporal fluctuations into the receptor potential of the IHC we can make inferences of the role the ribbon plays in temporal coding. A better understanding of how AN fiber discharge is altered in the absence of the ribbon will give us the framework necessary to make inferences as to why the ribbon might have evolved to support auditory processing.

4 Methods

4.1 Animals and groups

Experimental mice were bred from parents of the inbred C57Bl/6 and 129/Sv background heterozygous for the targeted deletion of exons 4 and 5 of the bassoon gene and genotyped using polymerase chain reaction (PCR). ABRs, DPOAEs and single-unit recordings from the cochlear nerve were done on mutant mice and their wild-type littermates between seven and eleven weeks of age. Due to the difficulty of eliciting sound-evoked responses from animals with high DPOAE thresholds, only animals with the best DPOAE thresholds were used for single-fiber recordings. All procedures were approved by the Institutional Animal Care and Use committee of the Massachusetts Eye and Ear Infirmary.

Both background strains, which these experimental animals are derived from, are associated with age-related hearing loss, which begins in the basal turn and progresses apically, due to their genetic background (Hequembourg and Liberman, 2001; Zheng et al., 1999). Elevated hearing thresholds first appear at high frequencies at approximately 12 weeks of age in C57Bl/6 mice. These elevated thresholds are correlated with basal-turn cochlear pathology that includes degeneration of fibrocytes in the spiral ligament and hair cells. This degeneration is progressive, spreading apically with advancing age. OHCs are lost first, later followed by loss of IHCs and secondary degeneration of AN fibers. Although it is possible to locate AN units that innervate high-frequency regions of the cochlea in this strain, their spatial receptive fields show degraded tuning consistent with OHC dysfunction. There appears to be additional, apical-turn pathology in C57Bl/6 mice that results in loss of up to 40% of AN fibers that innervate low-frequency regions despite an intact organ of Corti (Spongr et al., 1997; Hequembourg and Liberman, 2001).

Likewise, mice of the 129/Sv strain display similar high-frequency hearing loss as early as 8 weeks of age (Zheng et al., 1999). Although there are no studies of the morphological correlates of hearing loss in this strain, mice of the closely-related 129/SvEv strain show similar high-frequency hearing loss that accelerates with age. These mice show a very similar etiology to C57Bl/6 with basal-turn loss of OHCs as well as type IV fibrocytes in the spiral ligaments and supporting cell anomalies. Apical turns also showed some loss of fibrocytes (Ohlemiller and Gagnon, 2004).

Initial assays of cochlear function suggest that thresholds in this hybrid strain are close to normal until approximately eleven weeks of age. By limiting the age of experimental animals to six (age of maturation in the cochlea) to eleven weeks, thresholds should be sufficient to elicit stimulus-driven responses.

4.2 Genotyping of experimental animals

DNA for genotyping was extracted from tail digests using the DNeasy Blood & Tissue Kit (Qiagen, Valencia, CA). Using the following primers, a PCR was performed using the Taq PCR core kit (Qiagen, Valencia, CA) [5] using the mutant and wild-type primers below. Mutant primers yield an amplicon ~400 bp in size and the wild-type primers yield an amplicon ~600 bp (Figure 2).

[5] For unknown reasons, we have been able to get these primers to work only with the Taq DNA polymerase from Qiagen. The premixed Master Mix from Qiagen, which includes Taq polymerase, does not work either.

Wild-type primers:

AGT TGT CAA GCC TGT TCC AGA AGC

ACA CCG TCG GAG GAG TAG CCT GT

Mutant primers:

GGT ATC CTG TTC TGA AAG ACT TTC

AAG CTT GAT ATC GAA TTT GGC CTG

The incubation protocol for PCR involves an initial 5 min denaturation step at 95 °C, followed by 40 cycles of a denaturation step at 95 °C for 45 s, annealing at 66 °C for 45 s, and extension at 72 °C for 60 s. Once the 40 cycles are completed, we allowed a final extension step at 72 °C for 2 min. The PCR mix consists of 3.25 mM Mg^{2+}, 1x Qiagen PCR buffer, 10 mM each of the dNTPs, 10 μM of each primer, 1 μg template DNA, and 2.5 units Taq DNA polymerase.

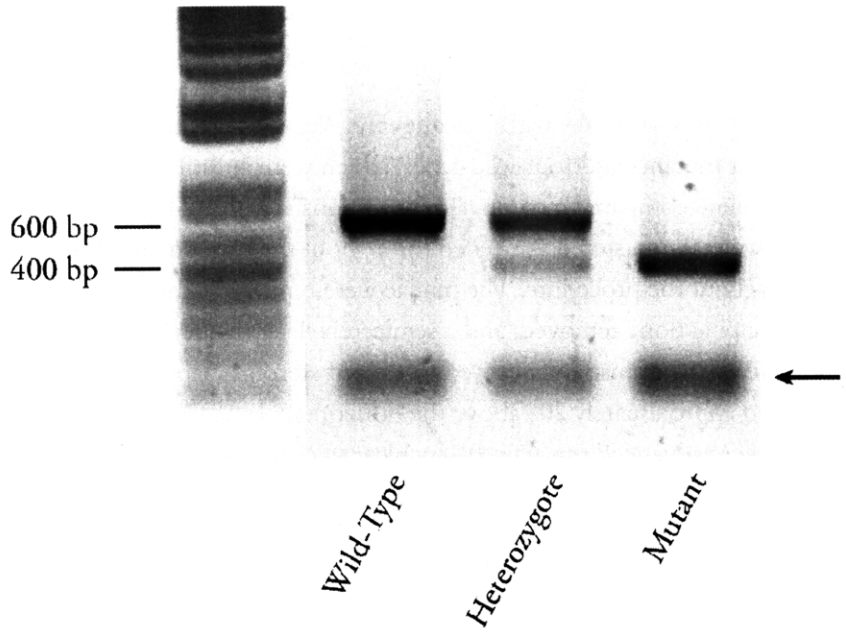

Figure 2 – Photograph of a 1% agarose gel stained with ethidium bromide used to visualize the PCR product from genotyping of three mice. PCR primers for the wild-type allele produce an amplicon of 600 bp while primers for the mutant allele produce an amplicon of 400 bp. A standard 1 kb ladder on the left is included for reference. The dark bands at the bottom of each of the three right-hand lanes are the PCR primer (arrow). As shown by the fainter bands of the amplicon from the mutant primer on this gel, the mutant primer appears to be less efficient than the wild-type primer. Indeed, in some PCRs, the mutant and wild-type primers had to be processed separately to ensure that the wild-type primer did not preferentially consume available reagents and mask amplification of the mutant allele.

4.3 ABR measurement

Mice were anesthetized intraperitoneally with ketamine (100 mg/kg) and xylazine (10 mg/kg). Needle electrodes were inserted at the vertex and pinna with a ground near the tail. ABRs were evoked with 4 ms tone pips (for all stimuli, duration is reported as the start of envelope onset to start of envelope offset) at a rate of 40/s using a 0.4 ms cosine tapered rise-fall envelope. The response was amplified, filtered and the first

8.5 ms digitized at 100 kHz and averaged across 512 presentations. Sound level was raised in 5 dB steps from 10 dB below expected threshold to 80 dB SPL. Digitized waveforms were filtered using a zero-phase first-order Butterworth filter with a pass band from 0.2 to 10 kHz and amplitude metrics were extracted for the first five waves using a semi-automated algorithm written in Python (Oliphant, 2007).

4.4 DPOAE measurement

DPOAEs at $2f_1$-f_2 were recorded in response to primary tones f_1 and f_2, with $f_2/f_1 = 1.2$ and f_2 level 10 dB < f_1 level in 5 dB steps. The ear-canal sound pressure waveform was amplified and digitally sampled at 4 μs intervals. Fast Fourier transforms were computed and averaged over 5 consecutive waveform traces prior to extraction of the $2f_1$-f_2 DPOAE amplitude and surrounding noise floor. Isoresponse contours were interpolated from the $2f_1$-f_2 amplitude versus sound level function with threshold defined as the f_1 primary level required to produce a DPOAE at 0 dB SPL.

4.5 In vivo single fiber recordings from the auditory nerve

In vivo recording of single units from the mouse AN were done as described previously (Taberner and Liberman, 2005).

4.5.1 Surgical approach

Animals were anesthetized intraperitoneally with xylazine (5mg/kg) and urethane (1.32 mg/kg), with the exception of a group of four mutants and four wild-types, which were anesthetized using the same protocol for ABR recordings to facilitate comparison of single-unit responses with ABR data. Boosters consisting of a third of the original dose were administered as needed throughout the experiment. Body temperature was maintained at 37° C throughout the procedure. The pinnae were removed, scalp reflected, portions of the lateral interparietal and occipital bone removed, and a semicerebellectomy performed to expose the dorsal cochlear nucleus. The head of the mouse was secured to a Kopf sterotaxic apparatus using a custom-designed head holder that is elevated approximately 20° above the horizontal plane. Glass electrodes filled with 2 M KCl and 4% methyl blue were advanced through the cochlear nucleus into the auditory nerve, angled 24° posterior from the coronal plane.

In the mouse, the cochlear nerve emerges horizontally from the fundus of the internal acoustic meatus and turns dorsally to innervate the cochlear nucleus (CN) lying immediately above the fundus. The length of the cochlear nerve that is not encased in the temporal bone is extremely short and thus provides a very small target for the recording electrode. The dorsal aspect of the semicircular canals (SSCs) are visible once the semicerebellectomy is performed and provides a landmark that can be used as a reference to assist in positioning the electrode. However, the appearance of the SSCs is slightly different from strain to strain of mouse, making it necessary to reestablish landmarks and coordinates for each new strain studied. In the C57Bl/6 strain there is a dark spot on the anterior semicircular canal just as it merges with the posterior duct to form the common crus. This mark is a reliable and consistent landmark from animal to animal. Trial surgeries on these mice indicate that positioning the electrode approximately 0.25 mm medial and 0.65 mm anterior to this landmark provides the best chance of hitting primary-like units between 800 and 1100 μm beneath the surface of the CN (Figure 3). The auditory nerve itself appears to lie between 1300 and 1700 μm re the surface of the CN as suggested by the high density of primary-like units and presence of gross

discharge[6] at this depth. In cat, the AN retains the tonotopy of the cochlear duct, making it possible to preferentially target units of a particular characteristic frequency (CF) based on stereotaxic coordinates (Kiang, 1965). There is little reason to think the mouse would not retain this tonotopic organization; however, the small size of the auditory nerve combined with the presence of the CN, which obscures our view of the auditory nerve and sometimes shift the position of the electrode slightly as it advances, makes it difficult to target a specific CF region. Regardless of this limitation, we found that more posterior passes tend to find fibers of lower CF than more anterior passes.

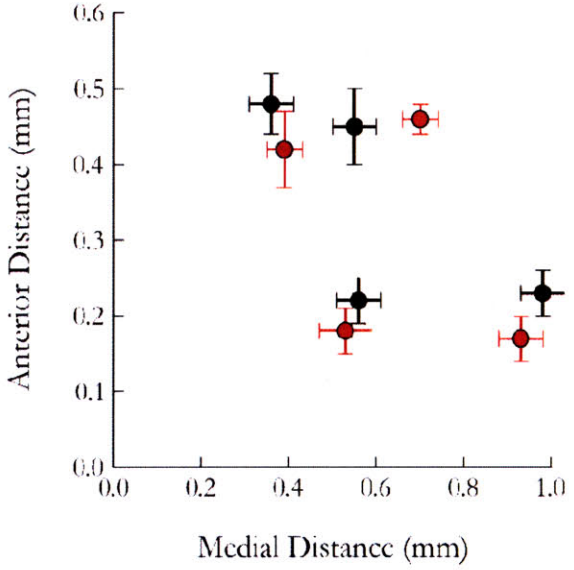

Figure 3 – Stereotaxic coordinates of the AN referenced to a landmark on the posterior semicircular canal in C57Bl/6 mice (see text for details). Immediately following conclusion of a single-unit recording experiment, the CN was aspirated to expose the AN and four locations representing the farthest extent of the AN in the anterior, medial, posterior and lateral directions were measured. These measurements were obtained to ensure that the electrode had been positioned properly during the single-unit experiment as well as to optimize positioning of the electrode in future experiments. Black indicates average coordinates for wild-type and red indicates coordinates for mutant. Bars indicate standard error of the mean (SEM).

4.5.2 Sound system

The sound system consists of dual electrostatic sound sources (Tucker-Davis Technologies ED-1) and a Knowles electret microphone coupled to a probe tube. The sensitivity of the probe tube microphone was calibrated between 0.1 and 73 kHz using a calibrated ¼ inch Brüel & Kjær condenser microphone in a coupler.

4.5.3 Stimulus response measures

50 ms noise bursts of 10 to 20 dB attenuation were used as a search stimulus. Tone bursts (50 ms, 2.5 ms $\cos^2$ tapered envelopes, 10/s) were used for all other sound-evoked measurements unless otherwise indicated.

---

[6] A small electric potential appearing at the onset of the search stimulus that appears to reflect farfield activity of multiple AN units.

Tuning curves represent isorate contours of 10 sp/s greater than SR, collected using a 2 alternate forced choice algorithm (Kiang et al., 1970). Samples of spontaneous activity were collected over durations of 10 to 150 s. Post-stimulus onset time (PST) histograms were created using tone bursts at CF, 30 dB above threshold. To facilitate comparison of single-fiber responses to the stimuli used to elicit ABRs, a subset of animals were anesthetized using the same regime as described for ABR measurement (ketamine and xylazine). For these animals, PST responses to on CF ABR tone pips (30 dB re threshold, alternating polarity, 4 ms duration, 0.4 ms cosine tapered window, 40/s) and condensation clicks (5 V, 50 μs, 10/s) were collected in addition to the other response metrics. Since we were primarily interested in units with CF < 16 kHz (due to potential basal-turn pathology as described in sections 5.1 and 5.3.2), we chose a click duration of 50 μs since the energy spectrum of this click has a zero at 20 kHz in contrast to the more conventional 100 μs click which has a zero at 10 kHz (Kiang, 1965).

Rate-level functions were measured at CF in 5 dB steps, presented in random order using 20-50 tone bursts per level and fitted using a modified version of a previously published model as described by Taberner and Liberman (2005). Dynamic range was defined as the level range between threshold and the saturation point. The threshold and saturation point were defined statistically as the level at which mean discharge rate was 1 standard deviation above SR and 1 standard deviation below maximum discharge rate, respectively (Winslow and Sachs, 1988). Calculations for dynamic range were based on the discharge rate computed from the fitted curve and the model-fit parameters for SR and maximum discharge rate. Trial-to-trial standard deviation of discharge rate was computed using the raw data and smoothed using a Bayesian adaptive regression spline (DiMatteo et al., 2001).

Recovery from adaptation was measured using a forward masking paradigm in which an on CF masker (100 ms, 2.5 ms $\cos^2$ tapered envelope, 30 dB re threshold) was followed at nine logarithmically-spaced intervals between 2 and 512 ms, presented in random order, by a short probe (15 ms, 2.5 ms $\cos^2$ tapered envelope) of the same frequency and level as the masker (Harris and Dallos, 1979). Synchrony was assessed using transposed tones, which were presented using an on CF carrier amplitude-modulated by a half-wave rectified sinusoid of 0.125, 0.5, 0.75 and 1 kHz in 5 dB steps. In contrast to the commonly-used computation for synchronization index (SI) described by Johnson (1980), which bins spike times into a positive zero crossing histogram prior to computing synchrony, we utilize a binless version by computing SI as the average of a vector sum where t_i is the time of the i^{th} spike in a train of n spikes and ω is the angular frequency of the modulator, $2\pi f$:

$$\mathrm{SI} = \frac{\left\| \sum_{i=1}^{n} e^{-j\omega t_i} \right\|}{n}$$

Statistical significance of synchronization was quantified using the Rayleigh statistic, which tests the null hypothesis that the time series is uniform throughout the cycle (Buunen and Rhode, 1978; Mardia and Jupp, 1999).

$$r = 2n\mathrm{SI}^2$$

SIs not meeting the criterion of $P < 0.001$ ($r \geq 13.8$) were discarded.

Short and long-range correlations of spiking activity were assessed from samples of spontaneous activity by computing the ratio of the spike count variance to the mean spike count for 100 logarithmically spaced counting windows, w, ranging from 1 ms to 10 s in width:

$$F = \frac{\sigma_w^2}{\mu_w}$$

Counts were generated by sliding each window in 1 μs increments along the spike train. For short-duration recordings, a simple algorithm that advances window across the sample in 1 μs steps, computing the spike count at each step, is sufficient. However, to speed up computation for large trains, we utilize a sparse counting technique as described in section 10.2.

4.5.4 Inclusion criterion

Since the electrode track passes through the CN en route to the cochlear nerve, a set of criteria first established by Taberner and Liberman (2005) were adopted to distinguish AN units from CN units. AN units typically have short response latencies of no longer than 5 ms which reflect a combination of delays such as propagation time of the traveling wave and synaptic vesicle exocytosis (Palmer and Russell, 1986; Temchin et al., 2005). Although CN units, at least in cat, can have response latencies shorter than 5 ms, most CN subtypes can be distinguished from AN fibers by their highly regular discharge and response pattern (Young et al., 1988). This discharge regularity is seen in the distribution of interspike intervals (ISIs), with AN units tending to have a much more variable ISI than CN units. The coefficient of variation (CV), or ratio of the standard deviation of the ISI to its mean, is a metric commonly used to assess regularity of spike discharge. AN units tend to have a CV_{ISI} greater than 0.5, while CN units tend to have a CV_{ISI} less than 0.5 (Young et al., 1988; Taberner and Liberman, 2005). Like the Fano factor, CV is a measure of the dispersion of a probability distribution. For a renewal process (of which the Poisson process is one), the CV is equivalent to the square root[7] of the Fano factor computed over time windows that approach infinity (Cox, 1962). Furthermore, many CN units have PST responses that can easily be distinguished from those of AN fibers (for review, see Rhode and Greenberg, 1992).

Spherical and globular bushy cells of the anteroventral CN (AVCN) are an exception since they preserve many of the response characteristics of their primary inputs from the AN including irregular discharge and PST response (Young et al., 1988; Blackburn and Sachs, 1989; Rhode and Smith, 1986; Smith and Rhode, 1987), although they have enhanced synchrony relative to AN fibers (Joris et al., 1994b, 1994a). At present there is no reliable method of distinguishing the primary-like responses of these CN units from AN fibers. However, the region populated by spherical bushy cells is much smaller in mouse compared to other mammals and tends to be located in the anterior-most portion of the AVCN. Since the track of the electrode passes through the dorsal CN and posteroventral CN (PVCN) prior to entering the cochlear nerve, spherical bushy cells likely reflect a very small fraction of our database. In contrast, globular bushy cells appear to straddle the region between the AVCN and PVCN and are interleaved with large bundles of the ascending AN fiber as it bifurcates into the AVCN and PVCN (Webster and Trune, 1982): there is a good chance that globular bushy cells, due to their location at the root of the AN, will be classified as AN fibers.

[7] Fano factor is the ratio of the variance to the mean, while CV is the ratio of the standard deviation to the mean, hence the squared relationship.

PST responses from globular bushy cells typically are primary-like with a notch occurring 1-2 ms after the initial peak, presumably due to refractoriness following a precisely-timed onset spike. However, this notch is not a reliable metric for distinguishing globular bushy cells since it is not always present at the stimulus levels (30 dB re threshold) used in this study (Blackburn and Sachs, 1989). Due to the relatively high thresholds in many of the experimental animals, we could not assess PST responses to higher-level tone bursts without risk of acoustic trauma. In a single fiber study from cat, CN units with primary-like responses in the PVCN were typically found in the vicinity of CN units with other response patterns such as onset and onset choppers (Godfrey et al., 1975). This suggests that the best approach to minimizing the number of globular bushy cells in our analysis is to exclude all primary-like units when found in the immediate vicinity of other CN units.

Units were included in analysis if they had a primary-like PST histogram, response latency less than 5 ms, CV_{ISI} greater than 0.5 and were recorded at an electrode depth greater than 1000 μm re surface of the CN. Response latency was computed from the mode of the first spike latency (FSL) distribution binned at 0.1 ms. Although primary-like CN units faithfully replicate many response properties of AN fibers, their enhanced synchrony was of some concern when analyzing phase-locking. Thus, particularly stringent criteria were required for experiments where we were collecting phase-locking data. Specifically, all primary-like units within ~100 μm of a CN unit that could be recognized based on other response properties (e.g. CV_{ISI}, PST response, response latency) were discarded.

To monitor cochlear stability, DPOAE thresholds were measured at seven half-octave spaced intervals spanning 5.6 to 45.2 kHz prior to opening the skull to establish a baseline. Thresholds were reassessed periodically throughout the experiment and units were discarded if the threshold of the DPOAE test frequency nearest CF had increased by more than 10 dB re baseline. At high stimulus levels ($\geq$ 75 dB SPL), distortion products generated by the acoustic system became visible and imposed a ceiling on the maximum threshold we could assess in our experimental setup. Due to this ceiling, only test frequencies for which the baseline threshold was at least 10 dB below the ceiling were used to assess cochlear stability.

Following each experiment, the CN was aspirated to expose the AN and the coordinates of each electrode pass were checked to ensure the electrode had been in the AN. During early experiments, there was some concern that the mutant phenotype might alter fundamental response properties of AN fibers in a way that would make these criteria invalid. However, careful analysis of all units collected during early experiments revealed that the shortest response latencies of mutant fibers were similar to wild-type and AN spike discharge retained its irregularity (Figure 8C). Stereotaxic measurements revealed no abnormalities in cranial anatomy in the vicinity of the temporal bone that may affect AN depth or location (Figure 3). Consequently, this study maintains the criterion established by Taberner and Liberman (2005).

4.6 Immunohistochemistry

4.6.1 Histological processing for ribbon analysis

Two wild-type and four mutant animals were anesthetized with ketamine and xylazine and perfused intracardially with 4% paraformaldehyde in phosphate buffered saline for histological assessment via organ of Corti whole mounts immunostained for calretinin and CtBP2 to label the inner hair cell and synaptic ribbon respectively. Cochleae were decalcified, dissected into half-turns and incubated in 5% normal horse serum with 0.03% Triton X-100 in phosphate buffered saline for 1 hour. This was followed by incubation in primary antibodies (rabbit α-calretinin from Millipore, Billerica, MA and mouse α-CtBP2 from Santa Cruz, Santa

Cruz, CA) for 19 hours, followed by secondary antibody (biotinylated donkey α-mouse from Jackson ImmunoResearch, West Grove, PA and Alexa Fluor-488 chicken α-rabbit from Invitrogen, Carlsbad, CA) for 60 min.

4.6.2 Analysis of synapse-attached ribbons

Cochlear half-turns were wet mounted in Vectashield (Vector Laboratories) and placed on glass slides for examination using a Leica confocal microscope with a 100x oil-immersion lens. In seven selected regions spaced approximately half octave from each other, focal z-series (0.25 μm step size) were obtained. The frequency of each location was estimated using a modified version of the physiological place-frequency map for CBA mice as recommended by Taberner and Liberman (2005). Amira, a three-dimensional visualization program (Zuse Institute Berlin, Berlin, Germany), was used to perform three-dimensional Gaussian filtering and transformations. Resulting images were cropped down to the IHC region and passed to Blob3D (University of Texas, Austin, TX), a three-dimensional quantitative software, to count the number of synaptic ribbons.

5 Results

5.1 Gross measures of cochlear response

Two minimally invasive measures of cochlear response, DPOAEs and ABRs, can be combined to provide a differential diagnosis of cochlear dysfunction.

DPOAEs are acoustic signals that arise from mechanical distortions in the cochlear response to two continuous tones. These distortion products, at frequencies not present in the input stimulus, are transmitted back into the ear canal where they can be measured with a sensitive microphone. Since they are amplified by biological motors in the OHCs and are unaffected by loss of IHCs or AN fibers (Liberman et al., 1997), they offer a sensitive metric of cochlear function (Lonsbury-Martin and Martin, 1990). The observation that DPOAE thresholds in bassoon mutants were indistinguishable from wild-types (Figure 4A) shows that many aspects of the auditory periphery, including sound transmission through the middle and inner ear, as well as mechanoelectric transduction by the OHCs, were functioning normally in the absence of bassoon. The background strain of this mutant line shows progressive cochlear degeneration, beginning at the high-frequency (basal) regions and progressing towards lower frequency regions (apically along the cochlear spiral) as the animal ages. This basal-turn degeneration of OHCs (Hequembourg and Liberman, 2001) is modest at the age of the mice we studied (6-11 weeks), but contributes to the threshold elevation for test frequencies $\geq$ 16 kHz.

ABRs represent the summed activity of neurons in the ascending auditory pathway, evoked by short tone bursts and measured by averaging the evoked electrical response from needle electrodes in the scalp. ABR thresholds in mutants were elevated 10 to 15 dB across most test frequencies (Figure 4B): the convergence of the threshold curves at high frequencies arose because of the basal-turn OHC degeneration. The amplitude of the first ABR wave (Figure 4C), which reflects summed activity of the AN, is reduced by a factor of 5.4 in mutants across all input sound pressure levels (Figure 4D). This reduction suggests a decrease in sound-evoked discharge rates or in the degree of response synchronization in the AN fibers activated by the tone pip. The combination of the decreased wave 1 and a normal DPOAE is consistent with dysfunction restricted to synaptic transmission at the synapse between inner hair cells and cochlear neurons. Indeed, the small plateau before wave 1 (arrow in Figure 4C) is identical in wild-types and mutants and may represent the summed receptor potentials of IHCs.

The later ABR waves arise from synchronous neural activity of brainstem nuclei in the ascending auditory pathway. Wave 2 in cats, for example, is dominated by the response of globular bushy cells in the cochlear nucleus (Melcher and Kiang, 1996), each of which receives afferent input from multiple AN fibers (Spirou et al., 2005). The smaller effects on later ABR waves in the mutants suggest that there is some degree of central compensation for the degradation of AN response.

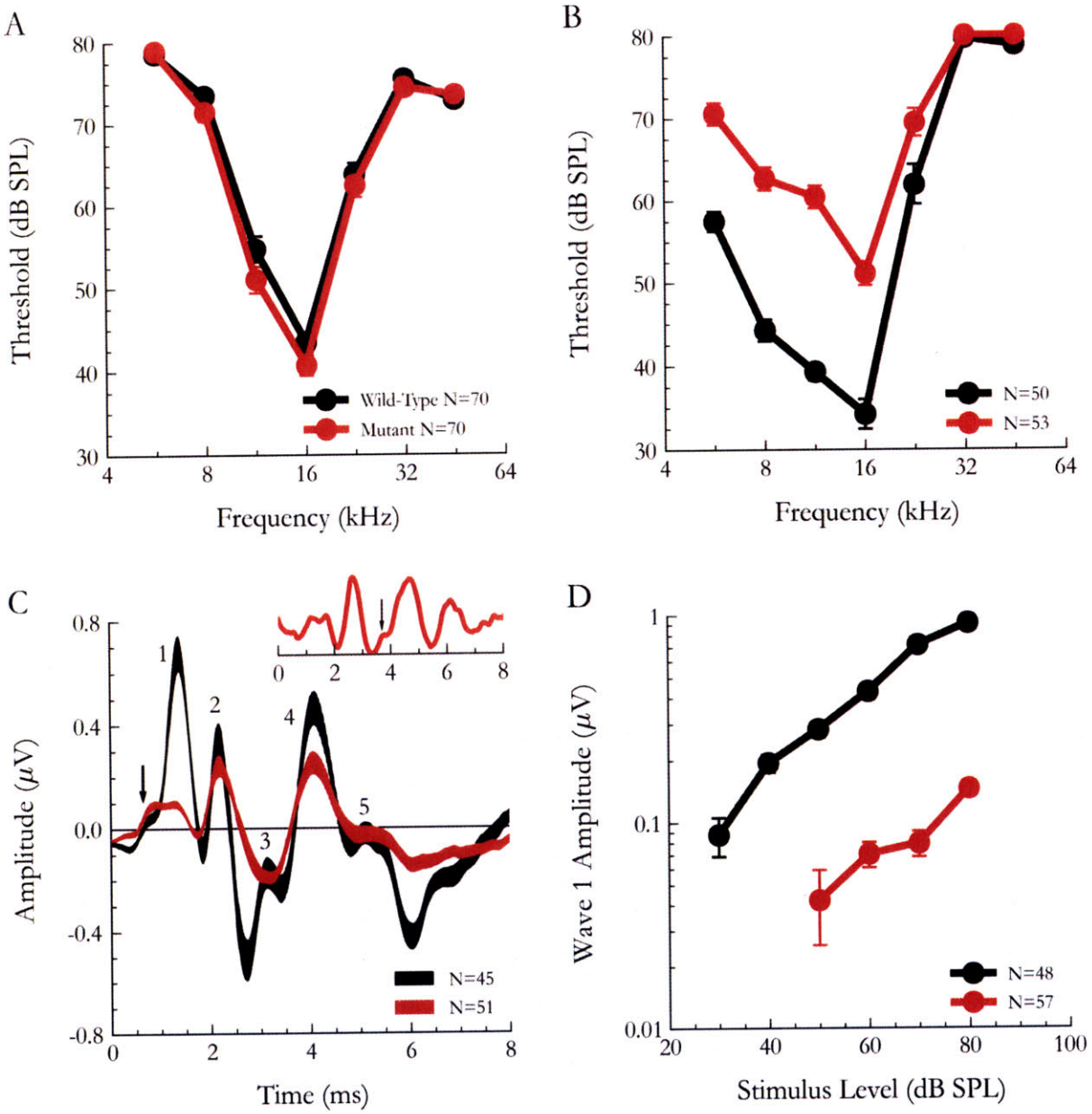

Figure 4 – Synaptic transmission was impaired in bassoon mutants. A and B: Mutant DPOAE thresholds were similar to wild-type (A) while ABR thresholds were elevated 10 to 20 dB across all stimulus frequencies (B). Thresholds for heterozygotes were identical to wild-type (data not shown). C: Grand average of ABR waveforms evoked by 80 dB SPL 16 kHz tone pips. Numbers indicate the corresponding waves and the arrow indicates putative summating potential. Thickness of the trace indicates ± SEM. Inset: Single ABR waveform from a mutant ear showing the presence of wave 3 (arrow). D: Amplitude of wave 1 re baseline as a function of stimulus level. Since there is some inter-ear variation in peak latency, amplitudes of individual waveforms were measured prior to averaging, hence, the data at 80 dB SPL cannot be compared to the peak of wave 1 from the grand average (C). Baseline is defined as the mean of the first 0.3 ms of the waveform. Data is expressed as mean ± SEM. Data from ears with no measurable DPOAE response at 16 kHz are not included. In this and all subsequent figures, black is used to indicate wild-type and red is used to indicate mutant.

5.2 Cochlear Immunohistochemistry

All of the myelinated AN fibers synapse exclusively onto IHCs of the organ of Corti (Figure 1). In the mammalian ear, virtually all AN fibers contact a single IHC via a single terminal swelling that forms a single synaptic contact with one synaptic ribbon.

To assess the number and distribution of synaptic ribbons in the absence of bassoon, sensory epithelia from four mutant and two wild-type mice with representative ABR and DPOAE thresholds were immunostained for the ribbon marker, CtBP2 (Khimich et al., 2005), and an IHC label, calretinin, to assess the proximity of ribbons to the IHC membrane. The number and distribution of ribbons in wild-type ears was consistent with known IHC innervation patterns and estimates of synaptic numbers from electron microscopic data (Francis et al., 2004; Stamataki et al., 2006): i.e. an average of 12.5 in the basal and apical turns with a maximum of 18 per IHC in mid-turns. In mutants, ribbons were larger, farther from the basal pole of the IHC and reduced in number throughout the cochlea (Figure 5), ranging from a minimum of 2 in mid-turns to an average of 4 per IHC in the basal turn (Figure 6). Furthermore, only 10% of these ribbons were touching the basal membrane where AN fibers typically form synapses. The remaining ribbons were either floating in the cytosol (10%) or in supranuclear regions (Figure 5). These findings are consistent with EM evidence from the apex of the cochlea demonstrating that, although some ribbons remain near the active zone, a large fraction is found floating in the cytosol (Khimich et al., 2005).

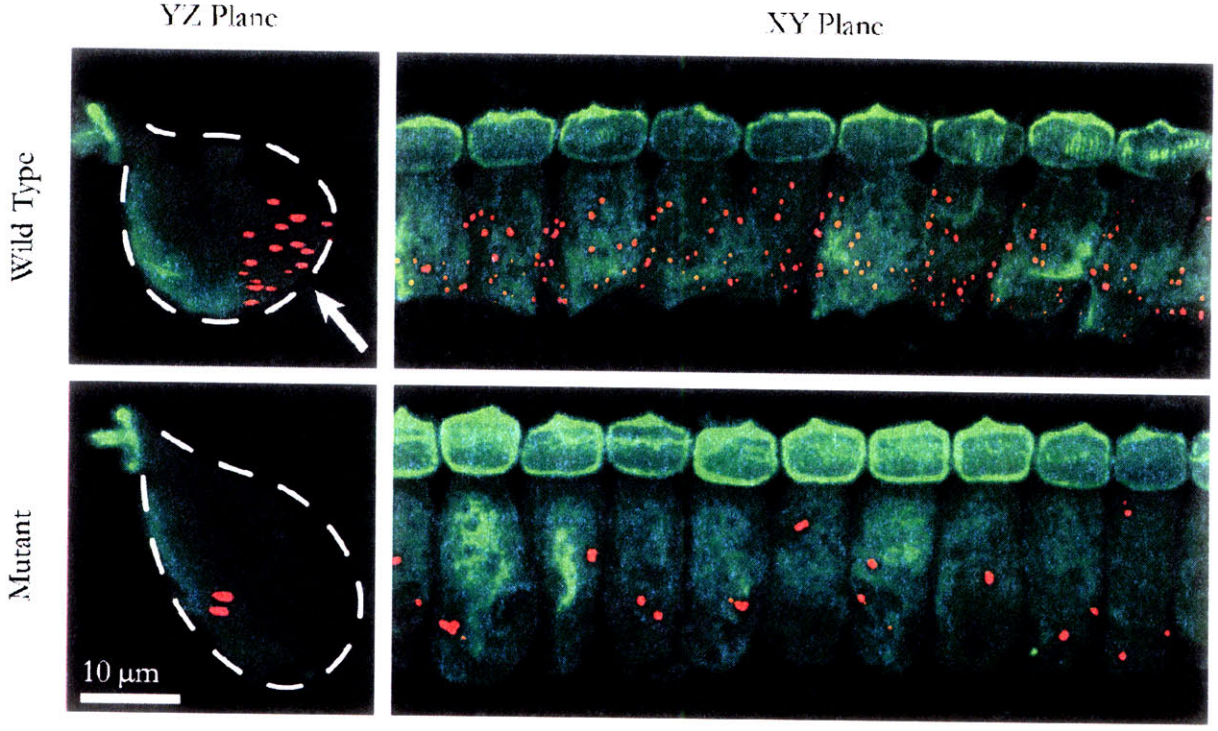

Figure 5 – Ribbons in mutant cochleae are larger in size, farther from the basal pole and reduced in number. Confocal projection of the 16 kHz place of cochlear whole-mounts from 8 week old animals immunostained with ribbon-specific α-CtBP2 (red) and an IHC label α-calretinin (green). Scale bar is 10 μm. White dashed line indicates outline of IHCs, arrow indicates basal pole. The YZ plane (left) is a side view of a single wild-type and mutant IHC. The XY plane represents a view from a perspective above the apical surface of the organ of Corti.

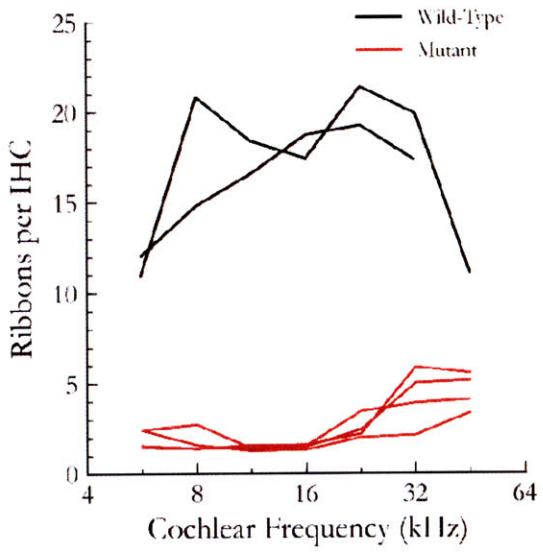

Figure 6 – Number of ribbons per IHC as assessed by counts from whole-mount preparations as shown in Figure 5.

5.3 Auditory nerve fiber responses

These results are based on recordings from 185 AN fibers from 27 wild-type mice and 78 AN fibers from 19 mutant mice. AN fiber response in the mammalian cochlea depends on CF, which reflects the mechanical tuning of the region of the cochlear duct where the fiber originates and SR, spike activity in the absence of sound, with high SR fibers showing lower thresholds and smaller dynamic ranges than low SR fibers (Liberman, 1978; Taberner and Liberman, 2005; Sachs and Abbas, 1974; Schalk and Sachs, 1980; Palmer and Evans, 1980). To thoroughly characterize the range of AN response, we sampled across the entire range of CFs and SRs in both wild-type and mutant ears (Figure 7A, Figure 8A).

5.3.1 Tuning and thresholds

Tuning curves of AN fibers are iso-response contours that reflect the mechanical tuning of the cochlear partition. Normal tuning curves show a sharp tip, defining the CF (black arrow in inset to Figure 7B) and a broad low-frequency tail. AN fibers from wild-types and mutants showed a similar range of CFs and thresholds (Figure 7A). Increasing AN thresholds for CFs > 16 kHz (open circles in Figure 7) in both genotypes reflect the basal-turn OHC degeneration seen in the DPOAEs (Figure 4A): in this and all subsequent analyses we separately consider the data from high CF AN fibers to remove the complication of OHC degeneration.

The exquisite frequency selectivity in the cochlea requires the normal functioning of OHCs, and their mechanical feedback that amplifies cochlear vibrations (Liberman et al., 2002). Since this motor function of the OHCs does not require synaptic transmission (Brownell et al., 1985), we expected AN frequency selectivity to be normal in bassoon mutants. Sharpness of tuning is often quantified using a metric known as the Q factor, defined as the ratio of CF to bandwidth at a particular level re threshold (usually 10 dB). In both mutants and wild-types, sharpness of tuning increased from 2, at low CFs, to 10, before falling off above 16

kHz (Figure 7B): these values are consistent with prior studies of normal mice of the CBA/CaJ strain (Taberner and Liberman, 2005).

The normality of tuning in mutants is consistent with intact OHC function and indicates that additional mechanisms that may further sharpen their frequency response are intact.

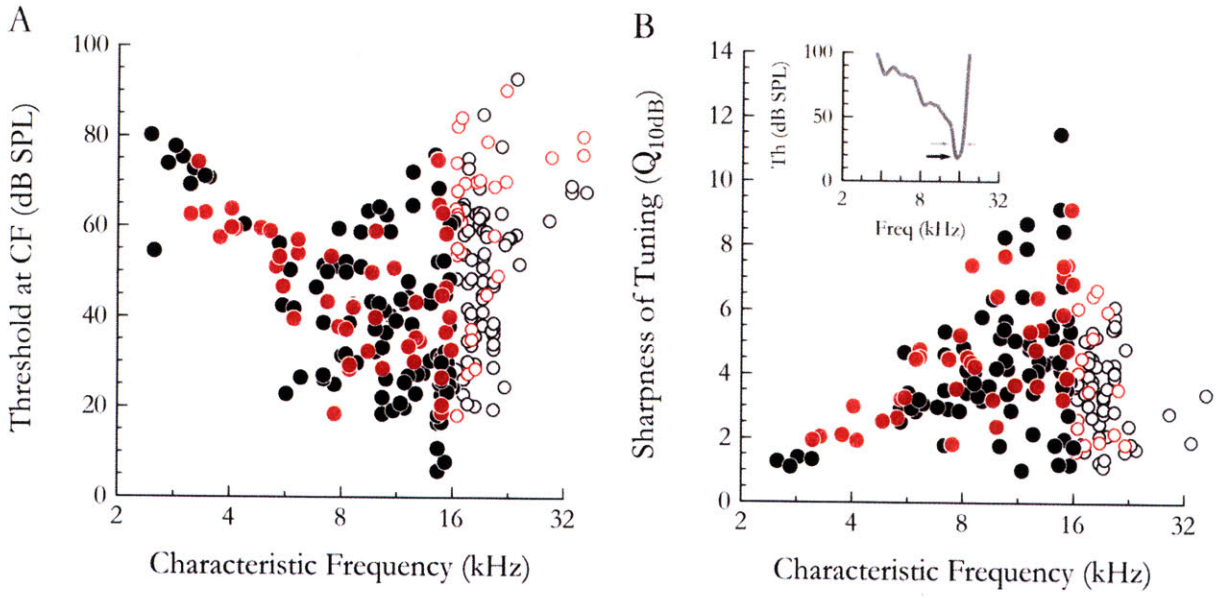

Figure 7 – Cochlear tuning was unaffected. The range of thresholds at CF (A) and sharpness of tuning (B) for mutant ears were similar to wild-type. B - inset: Example tuning curve (gray line) from a single fiber. Black arrow indicates the tip that defines CF and threshold and the gray arrows indicate bandwidth at 10 dB re threshold. In this and all subsequent figures, high CF fibers are plotted with hollow circles.

5.3.2 Spontaneous discharge - rate and regularity

Mammalian AN fibers have spontaneous activity in the absence of sound (Kiang, 1965): in mouse, SRs range from near-zero to 183 sp/s. In mutant fibers, SR never exceeded 81 sp/s: on average SR was reduced by 4.0 re wild-type (Figure 8A). Consistent with prior data from mouse (Taberner and Liberman, 2005) the SR distribution is skewed towards zero sp/s in both mutant and wild-type (Figure 8A) and high SR fibers tended to have lower thresholds than low SR fibers of similar CF (Figure 8B).

AN fiber discharge, whether spontaneous or sound-evoked, is highly irregular, with the distribution of interspike intervals approximated by an exponential distribution with a dead time (Li and Young, 1993; Young and Barta, 1986). This fundamental irregularity of AN response was not altered by loss of synaptic ribbons, as seen by the similarity of interval histograms from wild-type and mutant fibers of similar SR (Figure 8C). To systematically assess differences in response regularity, we split AN fibers into groups of similar SR (within 2 sp/s), discarded high CF ($\geq$ 16 kHz) fibers and fibers with significant ($P \leq 0.05$) fluctuations in rate (Heil et al., 2007), and performed a statistical test on each group: out of 10 groups containing at least one wild-type and one mutant fiber none had interspike interval distributions that differed significantly ($P \leq 0.05$) as assessed by the 2-sample Kolmogorov-Smirnov test, a nonparametric test that assesses whether the two samples are drawn from populations with the same probability distribution.

The variance of the spike count, or its predictability, is an essential component of signal detection theory (for review, see Delgutte, 1996; Green and Swets, 1974) and may define the lower bound of psychophysical performance limits (Heinz et al., 2001). In normal AN fibers, variance increases with mean rate such that a given rate change in a low SR fiber has greater "significance" than a similar rate change in a high SR fiber. To assess whether variance in mutants is reduced commensurately with the reduction in mean rate, we compared the Fano factor (ratio of variance to mean rate) for samples of spontaneous discharge from wild-types and mutants by sliding a 10 ms window, a value relevant for perceptual discrimination tasks (Plack and Moore, 1990; Moore et al., 1988; Delgutte, 1996), across the spike train to generate a series of counts. The Fano factor is clearly correlated with SR (Figure 8D) with refractory periods tend to regularize the spike train at higher rates (e.g. by placing an upper bound on how many spikes can occur in the counting window). However, no difference between genotypes was observed, ignoring a cluster of high CF wild-type fibers (black open circles in Figure 8D) with unusually large variance, presumably reflecting basal-turn pathology in the background strain: throughout our results, all ratios and values reported in the text exclude high CF fibers unless otherwise indicated.

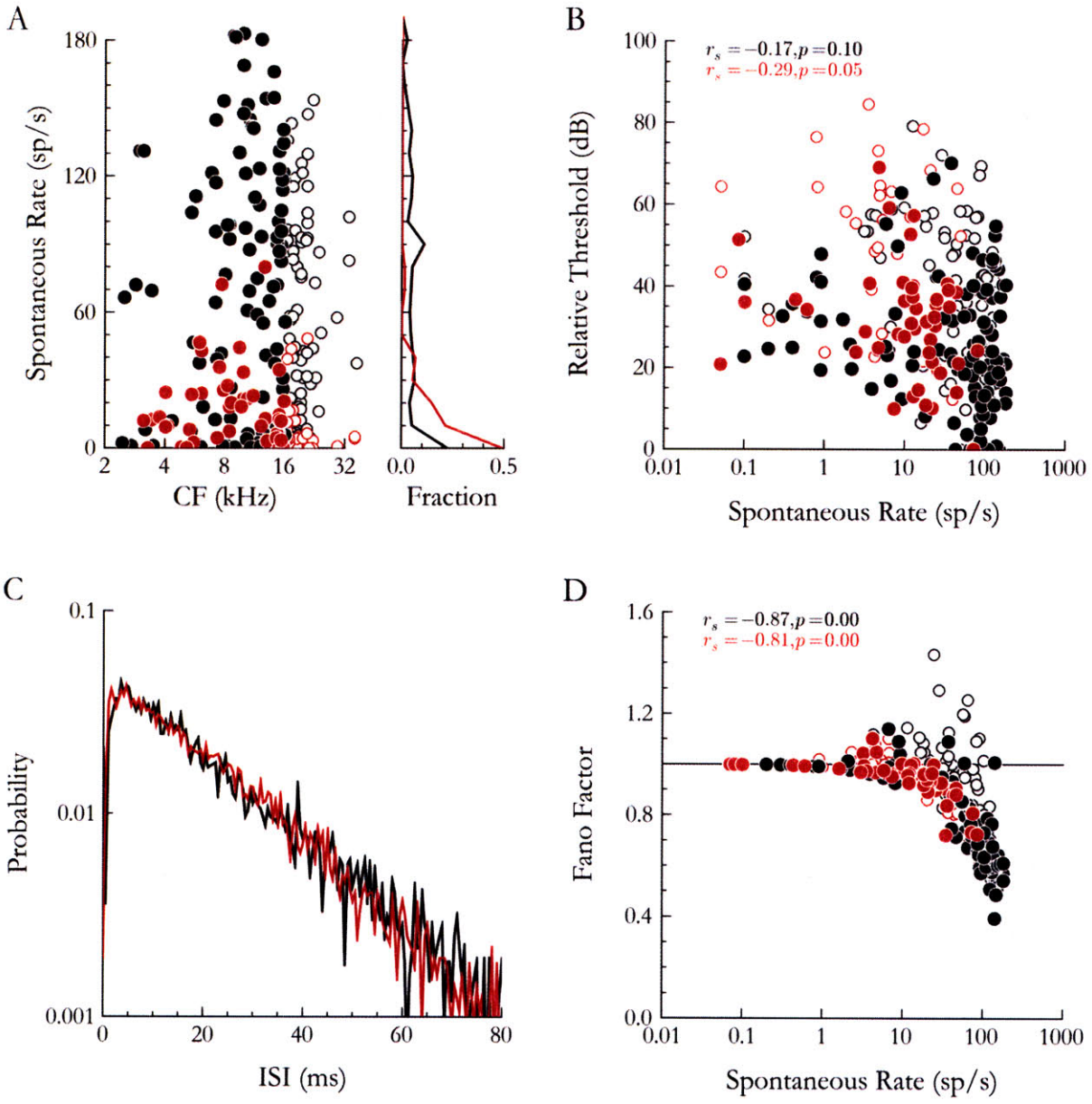

Figure 8 – A strong reduction in SRs across all CFs was observed in mutants although discharge irregularity was preserved. A: SR as a function of CF, with the histogram to the right showing the distribution of observed SRs using a bin width of 10 sp/s. B: Relationship between threshold sensitivity and SR. Relative threshold was computed by grouping AN fibers into octave-spaced bins and subtracting the minimum threshold found in each bin. C: Histograms of ISIs computed from pooled data from all fibers with SR between 40 and 50 sp/s. These histograms were normalized by the total spike count such that they reflect an estimate of the probability density function (PDF). Bin width is 0.5 ms. D: Relationship between SR and the Fano factor (ratio of the variance of the spike count to spike count mean) for a counting window of 10 ms. A Fano factor greater than 1 indicates a highly unpredictable spike count. Horizontal line indicates a Fano factor of 1, the value expected for a Poisson process. For all figures, only samples of spontaneous activity of at least 10 s were included. For this and all subsequent figures, SRs of zero are plotted at 0.05 when log scales are used. For this and all subsequent figures, Spearman rank-order correlation coefficient (r_s) between SR and the ordinate value is indicated along with its p-value where relevant. Fibers with CF $\geq$ 16 kHz were not included in assessment of correlation strength. For this and all subsequent figures that show data averaged across multiple units (e.g. average PST histograms), data from fibers with CF $\geq$ 16 kHz are excluded from the average.

5.3.3 Sound-evoked discharge rate and adaptation.

AN fibers respond to tone bursts with a spike rate that exponentially declines from a maximum at tone onset (i.e. peak rate) to an adapted rate (inset to Figure 9A). For 50 ms tone bursts, this post-onset adaptation can be described by the sum of two time constants (Westerman and Smith, 1984) of roughly 0.65 and 10 ms (Figure 10), although additional, longer time constants have been reported for long-duration ($\geq$ 5 min) tone bursts (Kiang, 1965). Since a similar post-onset decrease is not observed in the IHC receptor potential (Russell and Sellick, 1978; Palmer and Russell, 1986) and the reduction in calcium current or post-synaptic AMPA receptor desensitization (Goutman and Glowatzki, 2007) are minimal, adaptation is thought to arise mainly in synaptic transmission: for example, via exhaustion of the RRP of pre-synaptic vesicles (Furukawa and Matsuura, 1978; Moser and Beutner, 2000; Goutman and Glowatzki, 2007), with a prominent role for the synaptic ribbon in maintaining this pool (Khimich et al., 2005; Hull et al., 2006).

Sound-evoked discharge rates, both peak (Figure 9B) and adapted (Figure 9C), were reduced in the mutants by factors of 2.47 and 1.80, respectively. Instantaneous peak rates ranged from 155 to 1590 sp/s in wild-types and 80 to 620 sp/s in mutants. Adapted rates ranged from 33 to 286 sp/s in wild-type and 31 to 187 sp/s in mutant fibers. Peak rates are normally correlated with SR, thus a reduction in peak rate associated with the reduction in SR is expected in mutants. However, even when matched for SR, the peak rates in mutants were reduced relative to wild-type (Figure 9B). Nevertheless, the mean ratio of peak rate to adapted rate was reduced only slightly by the loss of bassoon (Figure 9D).

The time constants of adaptation were difficult to quantify in individual fibers because sample times from spiking activity were not sufficient to produce PST histograms of the requisite smoothness. Instead, fibers were grouped by SR into low, medium and high SR groups (Figure 10A, B and C, respectively) and the average PST histogram was computed for each group. All wild-type fibers with SR greater than the highest SR mutant fiber ($\geq$ 81 sp/s) were analyzed separately (Figure 10D). Regardless of whether adaptation was better described with one or two time constants, the slow time constant (τ_2) in mutant fibers was on a similar order to that of wild-type, ranging from 11 to 15 ms, although the amplitude of the slow component was reduced by a factor of ~1.8 for medium and high SR fibers and 3.02 for low SR fibers. The somewhat longer time constant of 32 ms in medium SR wild-type fibers may simply reflect the difficulty of accurately estimating the slow time constant from relatively short tone bursts. To ensure that estimates of the amplitude of each component was not skewed by deviations in estimates of the time constant, curve fitting was repeated for each histogram with the rapid time constant constrained to 0.65 ms and the slow constant to 10 ms. There was no significant difference in the estimate of the component amplitudes when constraining the time constants of adaptation, suggesting that our estimates are valid. The rapid component (τ_1) was not present in low and medium SR mutant fibers, but was present in high SR mutant fibers with a time constant on a similar order to that of wild-types of similar SR; however, the size of the component was reduced by a factor of 3.83 re wild-type (4.08 when τ_1 = 0.65 ms for both). The absence or greatly reduced amplitude of the rapid component in mutant AN fibers suggests that the vesicle pool that contributes to exocytosis $\leq$ 1 ms is greatly reduced at mutant synapses; however, the normal time course of adaptation suggest that the machinery governing release kinetics that underlie the various components is unaffected by the loss of bassoon.

The synaptic ribbon is hypothesized to play a role in rapid resupply of vesicles to the readily releasable presynaptic pool (Sterling and Matthews, 2005; Holt et al., 2004). Assuming that rapid adaptation and recovery from adaptation reflect depletion and refilling of the RRP, respectively, we used a forward masking

paradigm first described by Harris and Dallos (1979) to assess the recovery of the RRP following adaptation. In this paradigm (inset to Figure 11B), a 100 ms tone burst serves as a masker to adapt the response of the AN fiber. The masker tone-burst is followed, at varying intervals from 2 to 512 ms, by a 15 ms tone burst at the same frequency and level to probe the recovery of responsiveness of the neuron. At masker-probe intervals up to 8 ms the fiber's peak response to the probe is 81% of the response to the masker; whereas by 512 ms after the masker, the response to the probe has fully recovered in both genotypes (Figure 11A). No difference was observed in the amount of masking or time course of recovery to the last 5 ms of the probe (Figure 11B). The delayed recovery of the peak response to the probe suggests impaired resupply of the RRP at mutant synapses.

Central auditory neurons pool inputs across multiple AN fibers, requiring coincident, precisely-timed spikes to fire. The distribution of FSLs, collected from many trials, is a metric of the degree to which AN fibers fire synchronously in response to a stimulus (inset to Figure 12A). The mode of the distribution is a measure of response latency and generally decreases with increasing stimulus level (Heil and Irvine, 1997; Krishna, 2002) and more abrupt onsets (Heil et al., 2008). Distributions with large variance reflect less reliable firing in response to tone onset while smaller variances indicate a neuron that tends to reliably produce a spike on almost every trial. Although the range of response latencies (i.e. FSL modes) was similar between wild-type and mutant (Figure 12B), mean response latency was 0.4 ms longer for mutant AN fibers (inset to Figure 13B). FSL variance in mutant fibers, on the other hand, ranged from 3.35 to 137.22 ms^2 while wild-type fibers had variances ranging from 0.14 to 104.93 ms^2: this reflects an increase in mean FSL variance by a factor of 4.91 re wild-type. Minimum FSL variances observed in wild-type AN fibers are similar to that reported in the AN of cat (Heil et al., 2008).

The numbers of units responding at stimulus onset and the synchrony in discharge across these units are thought to be the major determinants of the amplitude of ABR wave 1 (Goldstein and Kiang, 1958). However, the reduction in mean peak rate by a factor of 2.47 cannot account for the much larger reduction of 5.4 in wave 1 amplitude (Figure 4D). This discrepancy may be related to the slower gating of the tone burst stimuli conventionally used in AN fiber recordings (2.5 ms cos^2 gated ramps) in contrast with the 0.4 ms cosine ramp used for ABR tone pips. To assess whether ribbons might increase the reliability and precision of a spike to different stimulus onsets, we compared AN fiber responses to moderate-level tone pips, gated by a 0.4 or 2.5 ms envelope, and clicks. There was a large increase in peak rate for the most rapid onsets in wild-type fibers (Figure 13A). In contrast, peak rates in mutant fibers were relatively uniform across all stimuli used. In both mutant and wild-type fibers there was a similar reduction in response latency with more rapid onsets, although mutant fibers had longer response latencies (Figure 13B). This data suggests that a component of the synapse required for rapid, reliable onset response is absent in mutants.

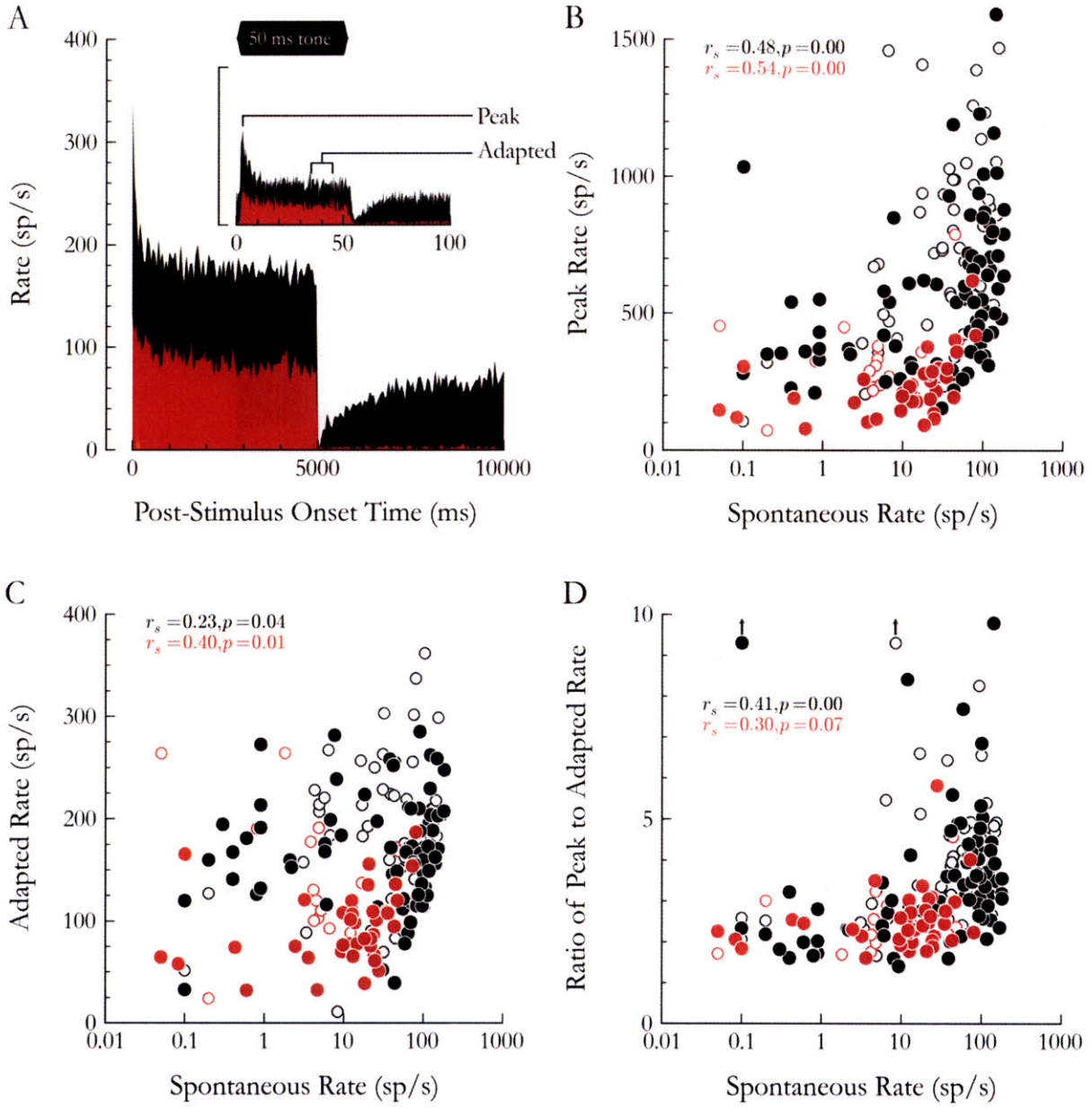

Figure 9 – Sound-evoked rates are significantly reduced. A: Representative PST histograms from a single wild-type and mutant fiber based on 20 repetitions of a 5 s CF tone at 30 dB re threshold. Bin width is 50 ms. Inset: Example mutant and wild-type PST histograms based on 200 to 1000 repetitions of a 50 ms CF tone at 30 dB re threshold. Bin width is 0.25 ms. Peak rate is defined as the instantaneous rate at stimulus onset, using a bin width of 0.5 ms, while adapted rate is the average rate over 35 to 45 ms following the peak response. B and C: Relationship between SR and peak (B) and adapted (C) rates. D: Response adaptation as a function of SR. Arrows indicate outliers with ratios, from left to right, of 31.5 and 37.3.

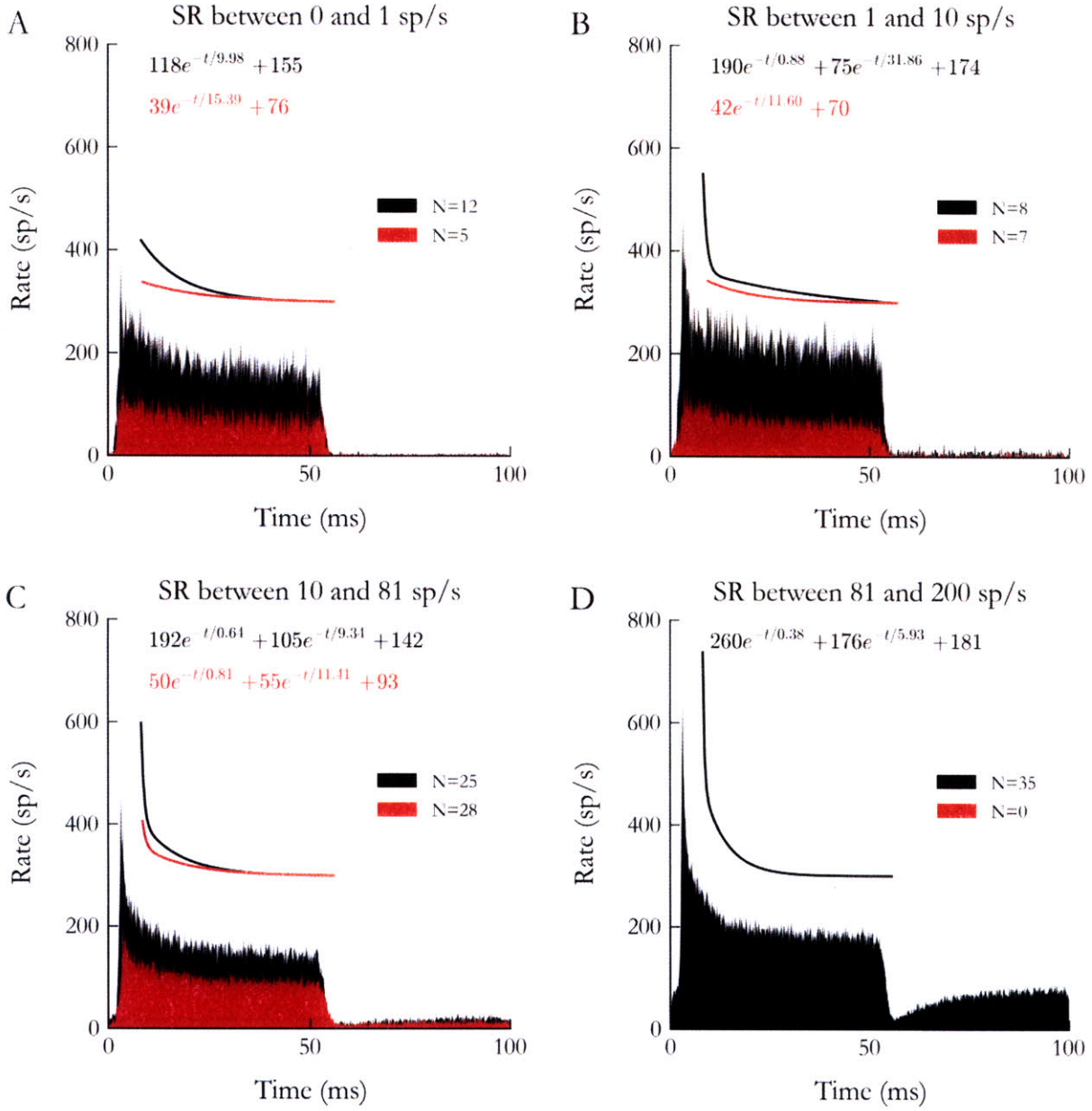

Figure 10 – Averaged PST histograms based on 200 to 1000 ms tone bursts gated by a 2.5 ms $\cos^2$ onset ramp using a 0.1 ms bin width. Prior to averaging individual histograms, they were corrected for response latency by aligning the peaks so that they were equal to the mean peak latency of their respective genotype. Each histogram was fitted to an exponential equation with two time constants. If the value of the rapid time constant was unrealistic (e.g. smaller than the bin size), then the histogram was fit to a single time constant instead. The resulting fit for the mutant histogram is overlaid on the wild-type fit to facilitate comparison of the time course of adaptation. Equations in the upper left hand corner indicate the best fit for each genotype in the format $Ae^{-t/\tau}$ where A is the rate in sp/s of the component and τ is the time constant of the component in ms. The last term is the adapted (i.e. steady-state) component. Fibers with CF $\geq$ 16 kHz are excluded. The upper bound of 81 sp/s in C was chosen as that reflects the highest SR mutant fiber in our database.

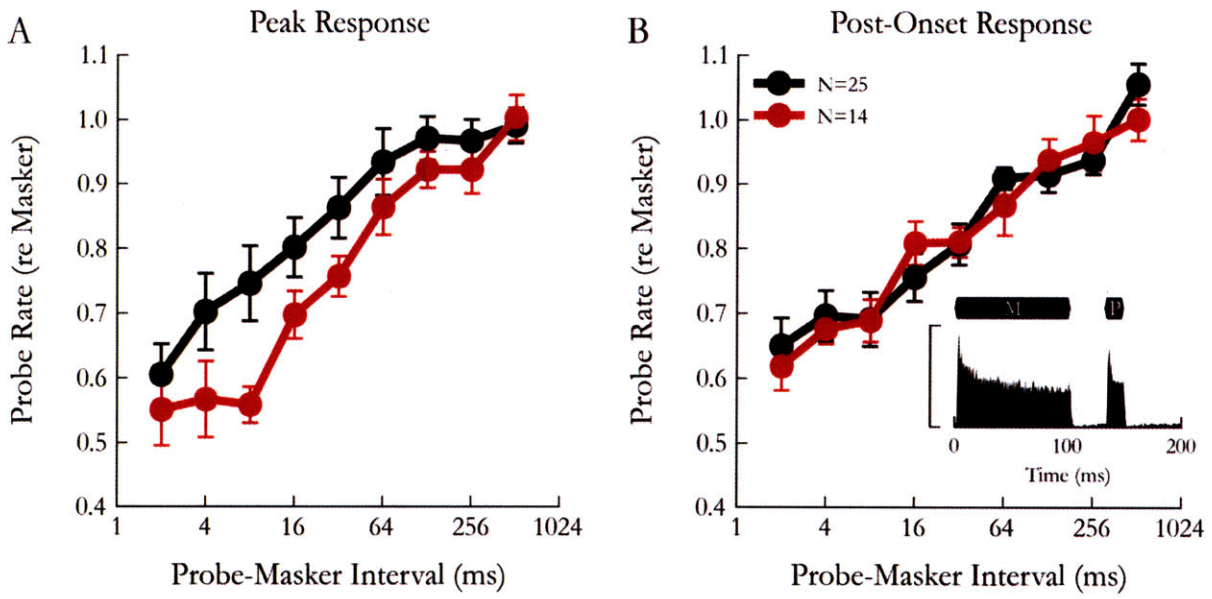

Figure 11 – Recovery of the peak response is impaired in bassoon mutants. Masking of the peak (A) and post-onset (B) rates. Peak rate is defined as the average rate over the first 5 ms of the probe and masker while post-onset rate is defined as the average rate over 10 to 15 ms following peak response (B, inset). Masking is the response to the probe expressed as a fraction of the response to the masker.

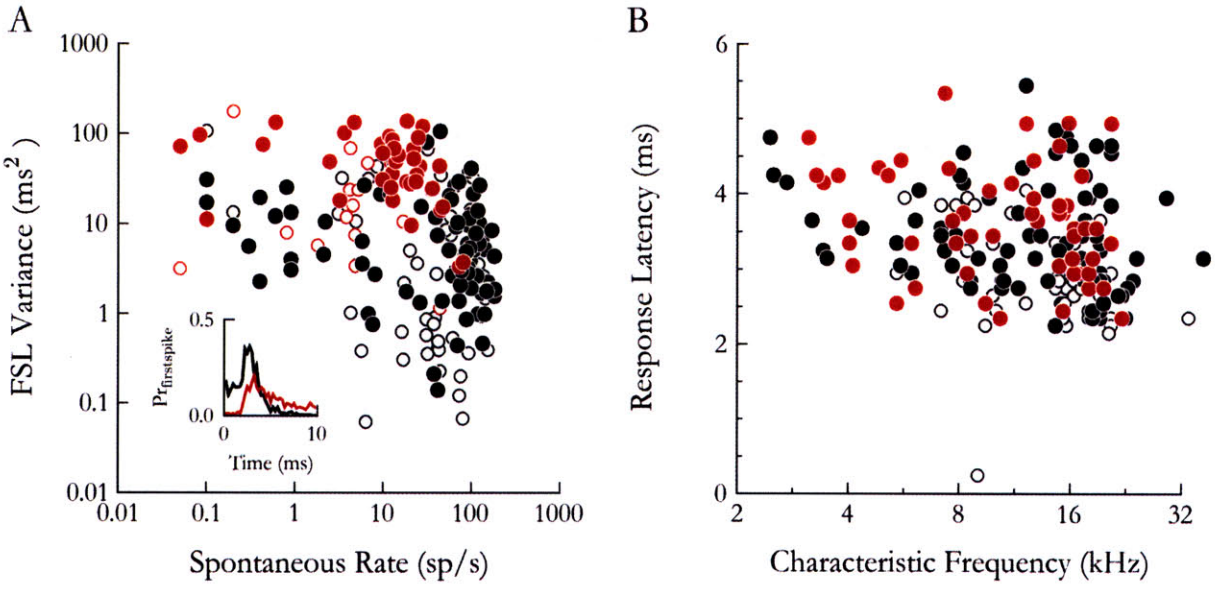

Figure 12 – Relationship between variance of the FSL and SR (A) and the mode of the FSL distribution and CF (B). FSLs were assessed in response to 200-1000 50 ms tone bursts. Distributions (inset to A) were generated by discarding repetitions during which no spike occurred during the first 50 ms and taking the first spike from the remaining repetitions. The mode was computed using a 0.1 ms bin width. The wild-type outlier with a response latency of 0.5 ms is due to a high SR that dominated the FSL distribution for this fiber.

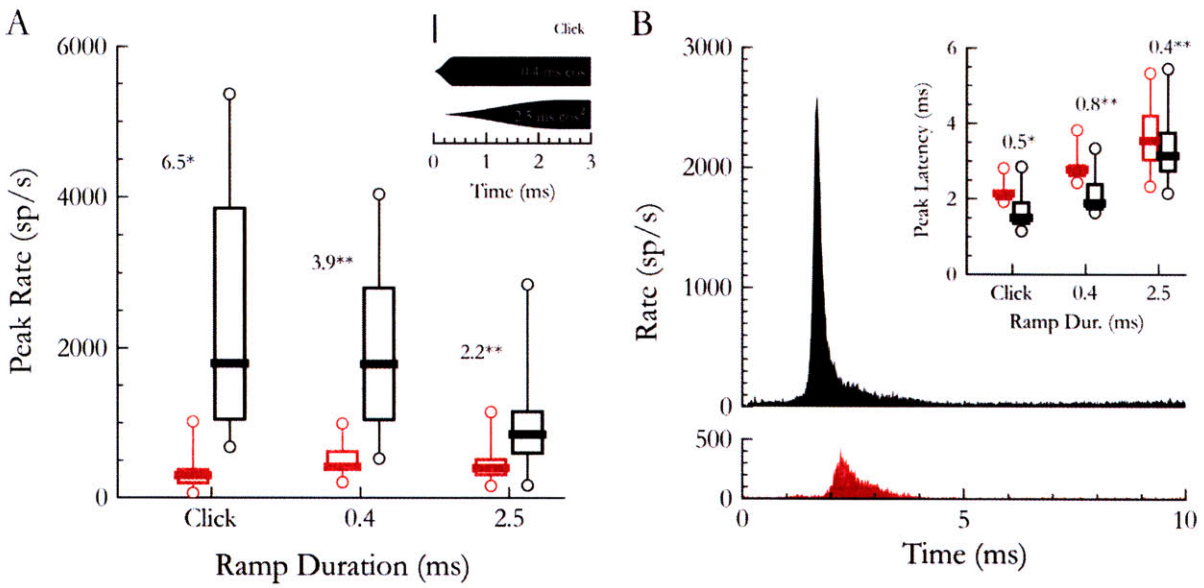

Figure 13 – The reduction of peak rate is more pronounced in response to more abrupt stimulus onset. A: Distribution of peak rates for each stimulus onset as assessed by PST histograms using a 0.1 ms bin width. Inset: Schematic illustrating the rise/fall envelope of the stimuli used for these plots. B: Averaged PST histograms in response to 50 μs condensation clicks using a 10 μs bin width. Prior to averaging individual histograms, they were corrected for response latency (inset to B) by aligning the peaks so that they were equal to the mean peak latency of their respective genotype. Note that the ordinate scale is calibrated so the histograms are directly comparable. A and inset to B: These box-whisker plots summarize the extremes (circles), 25th to 75th percentile (box) and median (heavy line through the box) of the distribution. Fibers with CF ≥ 16 kHz are excluded. Numbers next to each set of box plots indicate the reduction in mean rate re wild-type (A) or the difference in mean latency (B – inset). A single asterisk indicates statistical significance for the difference in mean at the $P \leq 0.05$ level and double for the $P < 0.01$ level as indicated by a two-tailed t-test of independent samples.

5.3.4 Dynamic range

Although the auditory system, as a whole, functions over an extremely large range of sound pressures (~120 dB or 6 orders of magnitude), individual AN fibers have much narrower dynamic range: as sound pressure is increases, discharge rates in single fibers typically saturates within 20 dB of threshold (Figure 14A). In normal AN responses, dynamic range is correlated with SR: high SR fibers have smaller dynamic ranges than low SR fibers (Taberner and Liberman, 2005; Sachs and Abbas, 1974; Schalk and Sachs, 1980). Since the IHC receptor potentials show a larger dynamic range, it is assumed that the hard saturation of high SR fibers arises in synaptic transmission.

The narrowest dynamic ranges, which allow for finer level discrimination, are absent in mutants (Figure 14B). However, there is no difference in dynamic range between mutant and wild-type when fibers are matched for SR, indicating that the presynaptic machinery that controls graded synaptic drive remains intact. We define dynamic range statistically as detailed in the methods and used by others (Sachs et al., 1989; Winslow and Sachs, 1988). The alternate approach where dynamic range is defined as the difference between stimulus levels evoking 10 and 90% of the model fit maximum driven rate does not account for the lower trial-to-trial variability of discharge in low SR fibers, thus estimates of dynamic range for a low SR fiber are not equivalent to estimates for a high SR fiber from a signal-detection perspective.

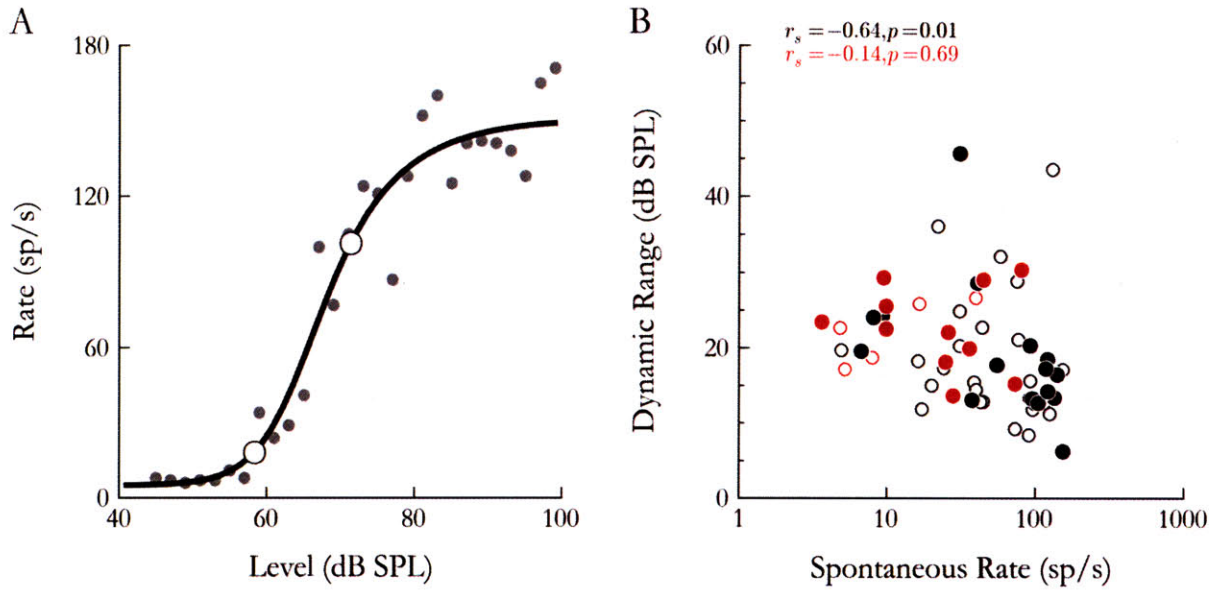

Figure 14 – Fibers with the narrowest dynamic ranges are absent in mutant. A: Dynamic range is assessed by fitting a model (black line) to rate responses from a level series (grey circles) and computing difference between the level at which the driven rate is 1 SD re SR and the level at which driven rate is 1 SD less than saturation (white circles). B: Relationship between dynamic range and SR. Model-fits with adjusted $R^2 < 0.75$ or with estimates of dynamic range that were broader than the range of levels sampled were excluded from analysis.

5.3.5 Refractory Period

The reduction in spontaneous and sound-evoked activity could potentially arise from a prolonged refractory period (RP). Although refractoriness is considered a property of the post-synaptic membrane, changes could be caused by developmental deficits due to the knockout. We rule out this possibility by demonstrating that absolute and relative RP are normal in mutants. The RP was estimated from spike trains obtained under conditions in which the synaptic drive is held constant (Li and Young, 1993). Under such conditions, the RP can be described as the sum of an absolute RP, during which no discharge occurs, and a relative RP during which the probability of a spike increases with a given time constant. Using this definition, we estimate the absolute and relative RP by computing the probability of a spike as a function of the time since the last spike and defining the absolute RP as the duration over which the probability of a spike is zero and the relative RP as the time constant over which the probability of a spike increases and plateaus.

Due to the difficulty of holding mouse AN fibers for extended periods of time required to collect a sufficient number of spikes from low SR units for analysis, we used data derived from a narrow window of the adapted portion of responses to 50 ms tone bursts. At the lowest rates, estimates of the absolute RP were quite wide, ranging from near-zero to 2 ms. However, as the number of spikes available for analysis increased, estimates for the absolute RP converge towards 0.61 ms (Figure 15A). Although the mean absolute RP for mutants is significantly lower than the wild-type mean, they are consistent with estimates from wild-type fibers of similar rate. Estimates for the time constant of the relative RP range from 2.5 ms at the lowest driven rates (50 sp/s) to a minimum of 0.45 at the highest rates (350 sp/s); however, no remarkable difference is observed between wild-type and mutant fibers when matched for rate (Figure 15B).

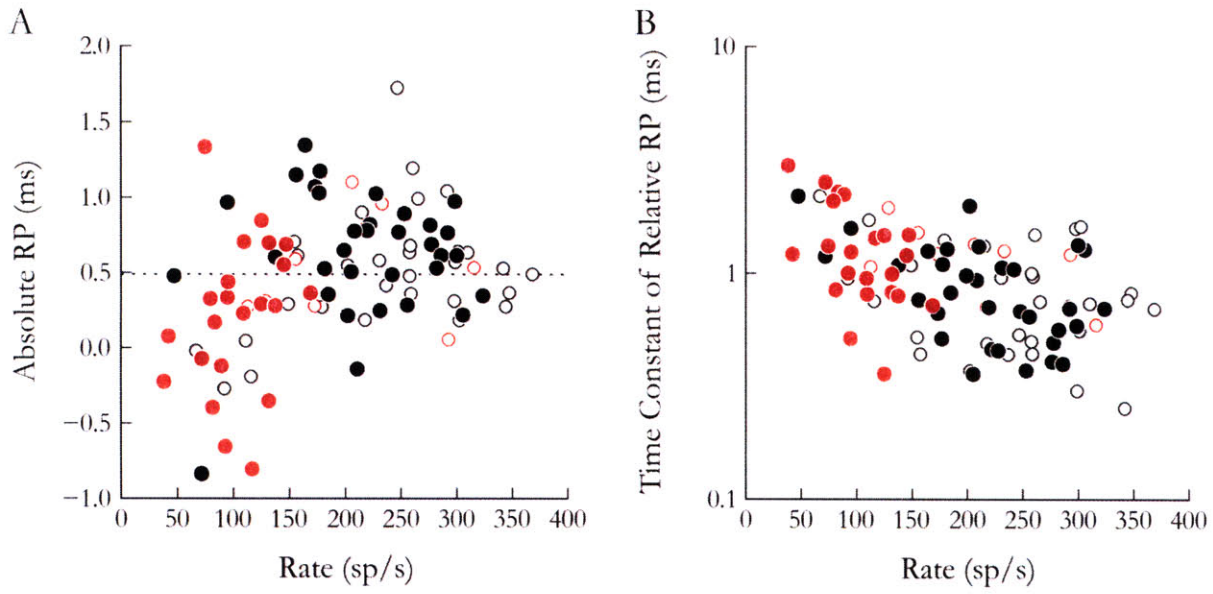

Figure 15 – Refractoriness is unaffected in mutant fibers. Relationship between driven rate and estimates of absolute (A) and relative RP (B) as assessed by from ISIs derived from the adapted portion of the response to 50 ms tone bursts (20 ms to 45 ms). Model-fits with adjusted $R^2 < 0.99$ are not included in analysis. To avoid biasing estimates of the refractory period, the curve fitting was not constrained to positive values; thus, the estimates of the absolute RP sometimes converged on negative values as shown in A.

5.3.6 Phase-locking

In response to periodic, amplitude-modulated stimuli AN fibers will tend to fire at a preferred phase of the stimulus cycle, a phenomenon described as phase-locking (Kiang, 1965; Rose et al., 1967). Phase-locking encodes the temporal structure of auditory stimuli and is essential for key aspects of binaural hearing. Small differences in the relative timing of sound between the two ears are the dominant cue for localizing the source of the sound (Wightman and Kistler, 1992; Macpherson and Middlebrooks, 2002), and the auditory system is sensitive to interaural differences as small as tens of microseconds (Klumpp and Eady, 1956; Wakeford and Robinson, 1974; Houben and Gourevitch, 1979). Precise timing of IHC exocytosis is required to maintain the fidelity of synaptic transmission required to encode these interaural differences.

Low-frequency pure tones are conventionally used to assess phase-locking; however, there is a decrease in synchrony of AN discharge as the stimulus frequency approaches 4 kHz due to the membrane capacitance of IHCs, which filter out high-frequency components of the receptor potential (Palmer and Russell, 1986). Since only a small fraction of mouse AN fibers is sensitive to low-frequency stimuli (Taberner and Liberman, 2005; Johnson, 1980), we instead use an on CF carrier tone that is amplitude-modulated by a low-frequency waveform (inset to Figure 16A). When low-frequency tones are presented to the cochlea, they are effectively low-pass filtered and half-wave rectified by the IHC. By modulating a high-frequency carrier with a half-wave rectified low-frequency sinusoid, we can transpose the information present at low frequencies into the envelope of a high-frequency tone. The resulting temporal modulation IHC receptor potential is similar to the pattern produced by its response to a low-frequency sinusoid (Palmer and Russell, 1986; Dreyer and Delgutte, 2006).

Using transposed tones, we show that mutant fibers retain the ability to phase-lock to the envelope. Since the strength of phase-locking depends on the modulation frequency, with a decrease in synchrony with increasing frequency, we assess phase-locking to four octave-spaced modulation frequencies between 0.12 and 1 kHz. These frequencies are chosen to capture the roll-off of phase-locking strength to transposed tones in cats, which begins at roughly 0.25 kHz with very little synchrony seen above 1 kHz (Dreyer and Delgutte, 2006). For a given frequency as the stimulus level increases the strength of phase-locking increases and saturates. Following Johnson (1980), the maximum strength of phase-locking to a level series is used as a measure for comparison.

In both mutants and wild-types phase-locking was strongest at 0.12 kHz with degradation in phase-locking strength with increasing modulation frequency (Figure 16B). Although mutants, on average, had stronger phase-locking than wild-types across all modulation frequencies, they were comparable to wild-types of similar SR (not shown). Interspike interval histograms of fibers with strong phase-locking reveal a multi-modal distribution with peaks spaced at multiples of the modulator period. By normalizing these histograms by the number of cycles of the modulator, we can assess the reliability of eliciting a phase-locked spike on each cycle. As shown by these normalized histograms (Figure 16A), wild-type AN fibers tended to produce a precisely-timed spike on almost every stimulus cycle. Mutants, in contrast, were far less reliable in producing a spike on each cycle of the modulator. However, the precision of timing was unaffected. High SR fibers tend to have a larger number of spikes occurring randomly throughout the cycle, which degrades the strength of phase-locking: the larger range of SRs observed in wild-type is reflected by the greater extent of synchrony strengths observed (Figure 16B)

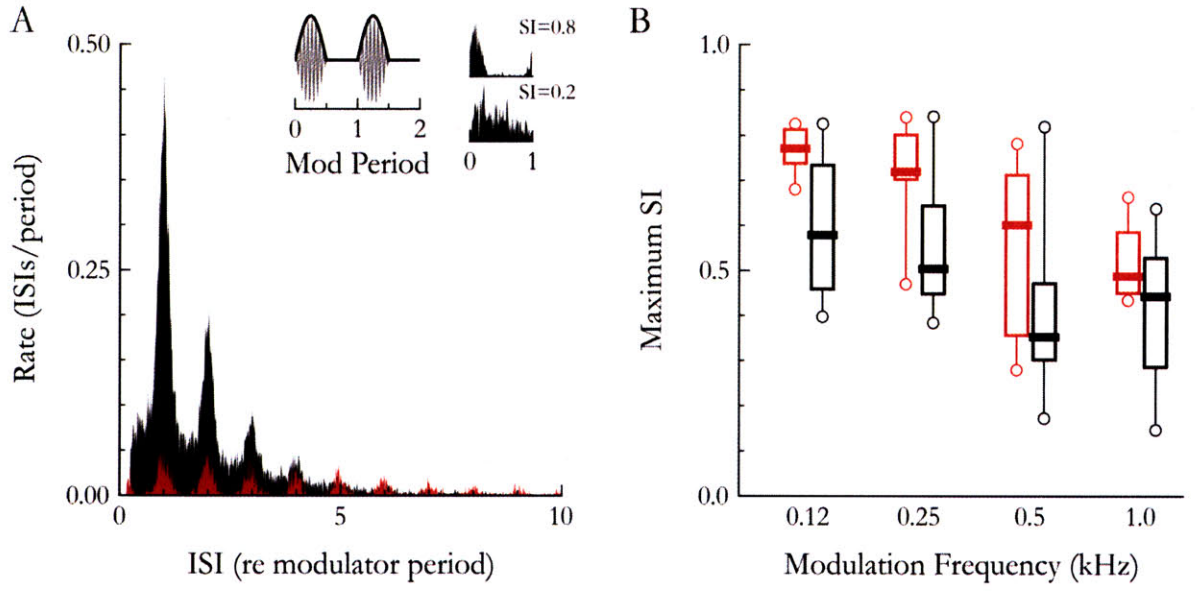

Figure 16 – Synchrony to the envelope of CF tones is preserved in mutant fibers although reliability is significantly degraded. A: Interspike interval histograms expressed as a fraction of the modulator period. ISIs from all fibers are pooled prior to computing the histogram. Counts for each bin are divided by the bin width (0.01 of the period) and total number of periods such that they represent the rate of ISIs. Inset, upper left: Schematic of a transposed tone with a high-frequency carrier (thin line) amplitude-modulated by a low-frequency modulator (thick line). Inset, upper right: Histograms showing the occurrence of spikes as a fraction of the modulator period for fibers with a high (top) and low (bottom) synchrony index (SI). SI is a measure of phase-locking (see section 4.5.3 for details of computing SI) with a value of 1.0 indicating all spikes occur at the same phase re modulation envelope, while a value of 0 indicates random

discharge through the cycle. B: As in Figure 13, these box-whisker plots summarize the 1st, 25th, 50th, 75th and 99th quantiles of the distribution of maximum synchrony indices observed for each modulation frequency.

6 Discussion

Since each AN fiber receives input from a single IHC active zone to which a single ribbon is normally anchored (Liberman, 1980), single-fiber recordings offer a sensitive functional metric of the contribution of individual ribbons to neuronal function. Response properties of AN fibers in mutants were similar, in many respects, to wild-type. Spike intervals retained their normal irregularity, thresholds of single fibers were unaffected, dynamic range was unchanged, synchrony was unimpaired and the ability to sustain discharge over a long-duration stimulus was unaffected. On the other hand, reductions were seen in spontaneous and sound-evoked single-fiber discharge rates with corresponding decrease in the amplitude the first wave of the ABR. Unlike wild-type fibers, AN fibers lacking ribbons failed to show increased peak rate as stimulus onset becomes more abrupt.

6.1 Ribbons are required for rapid onsets but not adapted rate

The large disparity in peak rate by a factor of 6.5 for clicks compared with a disparity of only 1.8 for the sustained response highlight the importance of the ribbon in coding of stimulus onsets and rapid acoustic transients. Whole cell capacitance measures reveal a biphasic component to exocytosis: a rapid component on the order of a few milliseconds which may reflect the immediate RRP at the base of the ribbon (Moser and Beutner, 2000) and a slower, sustained component which may be due to ribbon-mediated rapid resupply of the RRP (von Gersdorff et al., 1996) or diffusion of calcium to distant release-ready vesicles (Voets et al., 1999). Prior in vitro work on isolated IHCs demonstrated that calcium current was reduced by a factor of ~1.5, coinciding with a reduction of rapid exocytosis after a 2 ms depolarization by a factor of 3.3 and sustained exocytosis after a 50 ms depolarization by a factor of 1.4 (Khimich et al., 2005). The large reduction in calcium influx was attributed to a reduction in $Ca_v1.3$ channel number or impaired co-localization with synaptic vesicles since the voltage-dependence of activation for these channels was normal (Khimich et al., 2005). Such a finding suggests that, in addition to loss of anchored ribbons, the structural organization of the active zone is disrupted in bassoon-deficient mice with respect to anchoring of ion channels. Regardless of the cause of the reduced calcium current, the reduction in the sustained component of exocytosis appears to primarily mirror the reduction in calcium current. However, rapid exocytosis in ribbon-deficient IHCs was significantly impaired even when compared with data from wild-type IHCs where calcium current is artificially reduced to levels found in bassoon-deficient IHCs. Thus, the reduction in rapid exocytosis reflects both a reduction in calcium current and loss of the synaptic ribbon.

The reduction in peak rate and adapted rate in response to 50 ms tone bursts by factors of 2.47 and 1.8, respectively, are postsynaptic correlates of the reduction in rapid and sustained exocytosis. If we assume that the difference in adapted rate reflects the difference in calcium current in vivo and that the ribbon has no role in the adapted response as suggested by the in vitro data (Khimich et al., 2005), we can thus infer the in vivo reduction of calcium current from the adapted rates. If all these assumptions are true, then the reduction in onset rate is the product of the reduction in calcium current and loss of the ribbon-dependent component. Factoring out the reduction in calcium current by a factor of 1.8, as inferred by the reduction in adapted rate, we find that loss of the ribbon reduces onset rates anywhere from 1.4 for 2.5 ms $\cos^2$ rise times to 3.6 for clicks.

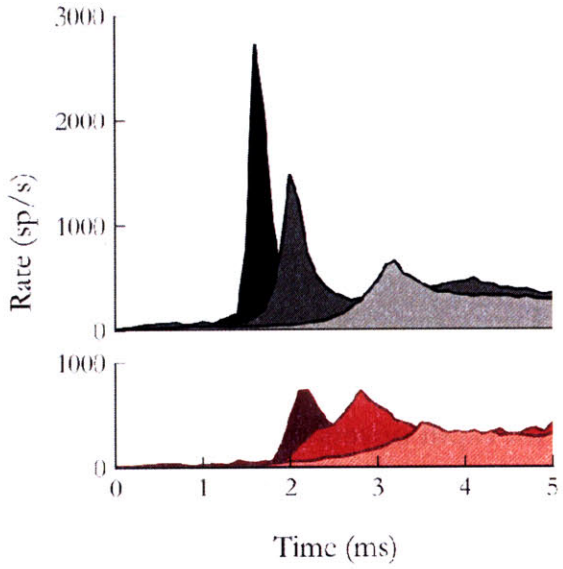

Figure 17 – Average PST histograms, using a 0.1 ms bin width, highlighting the onset response of (from left to right) clicks and tones gated with 0.4 ms and 2.5 ms cosine ramps. Prior to averaging, peaks were aligned with the mean latency of the respective genotype. Top plot shows wild-type, bottom shows mutant. Mutant rates have been multiplied by a factor of 1.8 to highlight the ribbon-dependent component of exocytosis.

Indeed, this hypothesis is supported by a similar experiment in goldfish retinal bipolar cells, which display circadian fluctuations where ribbon number is reduced by ~65% at night, but the number of active zones remain constant. Membrane capacitance reveals that rapid exocytosis, as assessed by 20 ms depolarizing steps, is significantly impaired at night compared with daytime, while there is no difference in the response to 200 ms depolarizations (Hull et al., 2006).

At the resting potential of murine IHCs, approximately -72 mV (Oliver et al., 2003), there is no measurable calcium current in either wild-type or mutant (Khimich et al., 2005). Although the nature of spontaneous activity is unclear, the tight spatial coupling between synaptic vesicles and calcium channels suggests that chance openings of a few calcium channels may be sufficient to drive exocytosis (Brandt et al., 2005). Since $Ca_v1.3$ channels cluster at the base of the ribbon, the size of the RRP at the base can influence the rate of spontaneous activity since calcium transients would not diffuse to outlying vesicles. Under this scenario, the reduction in $Ca_v1.3$ channel number believed to underlie the putative reduction in the calcium current (Khimich et al., 2005), would certainly influence spontaneous activity as well, reducing it by a factor of 1.8. Consequently, the remaining reduction in SR by a factor of 2.2 may reflect a reduction in the size of the RRP.

The smaller reduction in adapted rates is consistent with the reduced calcium influx in mutant IHCs in vitro and lends support to the hypothesis that sustained exocytosis is primarily mediated by outlying vesicles (Voets et al., 1999). Indeed, the normal suppression and time course of recovery from forward masking of the post-onset component indicate that the contribution of the ribbon-tethered pool (Lenzi et al., 1999) to sustained exocytosis is minimal and that mobilization of vesicles on the ribbon is not the rate-limiting step. In contrast, the peak response of the probe was suppressed to a greater degree following forward masking, although the time course of recovery was normal. This separation of the peak recovery from post-onset recovery lends

support to the idea that rapid exocytosis and sustained exocytosis reflect two distinct pools of synaptic vesicles – one positioned immediately adjacent to $Ca_v1.3$ channels at the base of the ribbon itself and an outlying population of vesicles that contribute to the slower, sustained exocytosis. Resupply of the outlying pool does not appear to depend on the synaptic ribbon itself.

Unlike CNS synapses, in which synaptic vesicles are anchored to the actin cytoskeleton via synapsin (Henkel et al., 1996; Kraszewski et al., 1996), vesicles in ribbon terminals are highly mobile (Holt et al., 2004). This mobility appears to create random collisions with the presynaptic membrane (Zenisek et al., 2000) and may be sufficient to resupply the RRP (Holt et al., 2004). If free diffusion of vesicles is indeed the sole mechanism for resupply of the sustained component of exocytosis, then it is not surprising that there is no difference in adapted rates between wild-type and mutant once the putative reduction in calcium current is factored in. Resupply of the pool of vesicles implicated in rapid exocytosis appears to be impaired in the absence of the ribbon. It has been hypothesized that the ribbon may facilitate resupply of this pool by acting as a vesicle trap and providing a surface, terminating at the active zone, which restricts diffusion of vesicles along two dimensions. Loss of this "guide" at bassoon-deficient synapses will certainly alter the kinetics of resupply of vesicles to the active zone, resulting in an impaired onset response.

The calcium sensor driving exocytosis in IHCs appears to require the cooperation (i.e. sequential binding of ions in which the prior ion increases the affinity of one or more binding sites on the molecule) of 3 to 5 calcium ions. If the calcium sensor is situated sufficiently far from calcium channels ($\geq$ 50 nm), the summation of current from many calcium channels appears to be necessary to drive exocytosis (for review, see Augustine et al., 2003). This results in a nonlinear relationship between calcium influx and exocytosis since release of each vesicle depends on the probability of multiple, independent channels opening simultaneously. In contrast, IHCs appear to have a linear relationship between calcium influx and exocytosis (Brandt et al., 2005; Goutman and Glowatzki, 2007; Keen and Hudspeth, 2006), indicating that the calcium sensor is located sufficiently close to a cluster of calcium channels such that that the resulting influx from only a few is sufficient to initiate release. Thus, progressive increases in receptor potential lead to recruitment of additional calcium channels and a linear increase in release rate – which is reflected in the linear region of AN fiber rate-level functions.

Interestingly, the linear relationship between calcium influx and release rate appears to hold for both the rapid and sustained component of exocytosis (Goutman and Glowatzki, 2007), suggesting that synaptic vesicles may preferentially dock in the immediate vicinity of calcium channels. The normal dynamic range observed in bassoon-deficient AN fibers allows us to rule out the simple explanation that ribbon-mediated resupply preferentially positions vesicles near $Ca_v1.3$ channels. An alternate mechanism of preferential docking of vesicles at calcium channels has yet to be identified; however, otoferlin, the putative calcium sensor in IHCs (Roux et al., 2006; Beurg et al., 2008), appears to have binding domains for $Ca_v1.3$ channels (Ramakrishnan et al., 2009) that may mediate this mechanism.

6.2 The ribbon is required for reliability but not precision

How might loss of the RRP tethered to the base of the ribbon influence spike timing? Two metrics are conventionally used to assess temporal precision: variance of spike timing in response to a repeated stimulus, and synchrony to an amplitude-modulated stimulus. The former metric has been utilized extensively in the visual system (for review, see Tiesinga et al., 2008) and the cortex (Mainen and Sejnowski, 1995), while the

latter is commonly used in the auditory system (Rose et al., 1967; Johnson, 1980). Although ribbon-deficient AN fibers have normal, or better, synchrony to the envelope of transposed tones compared to wild-type, the variance of the FSL in response to tone bursts is increased by a factor of 4.91 (Figure 18). In fibers where data is available for both metrics, mutant fibers generally had the highest FSL variance and the best synchrony.

The discrepancy between these two metrics arises from the fact that the FSL variance convolves two distinct concepts, reliability of firing and precision in the time of firing. The use of spike timing variance works well in the visual system and the cortex because they often are characterized by low levels of spontaneous activity or extremely reliable spiking (Mainen and Sejnowski, 1995) where individual spikes can readily be associated with a corresponding event, such as a large temporal fluctuation in the stimulus (Berry et al., 1997). Unfortunately, this metric is not such a straightforward assessment of timing in the auditory system due to the high rates of spontaneous activity and large response variability from trial to trial.

Consider a neuron which fires only in response to stimulus onset. In such a system, the variance of spike timing relative to stimulus onset is an excellent measure of temporal precision. Even if the neuron fails to reliably produce a spike on every onset, our measure is not affected if we simply disregard the failures. However, once we start to analyze the times of first spikes in a noisy system that has a low level of spontaneous activity, our metric begins to break down. A neuron could, hypothetically, fire a perfectly-timed onset spike only once every 10 cycles or so (with spontaneous activity imposing the variance on our metric), or it can fire an imprecisely-timed spike on almost every stimulus cycle. Thus, two neurons, one being very reliable but with low precision and another being very unreliable but very precise with a low level of spontaneous activity, can have the same FSL variance.

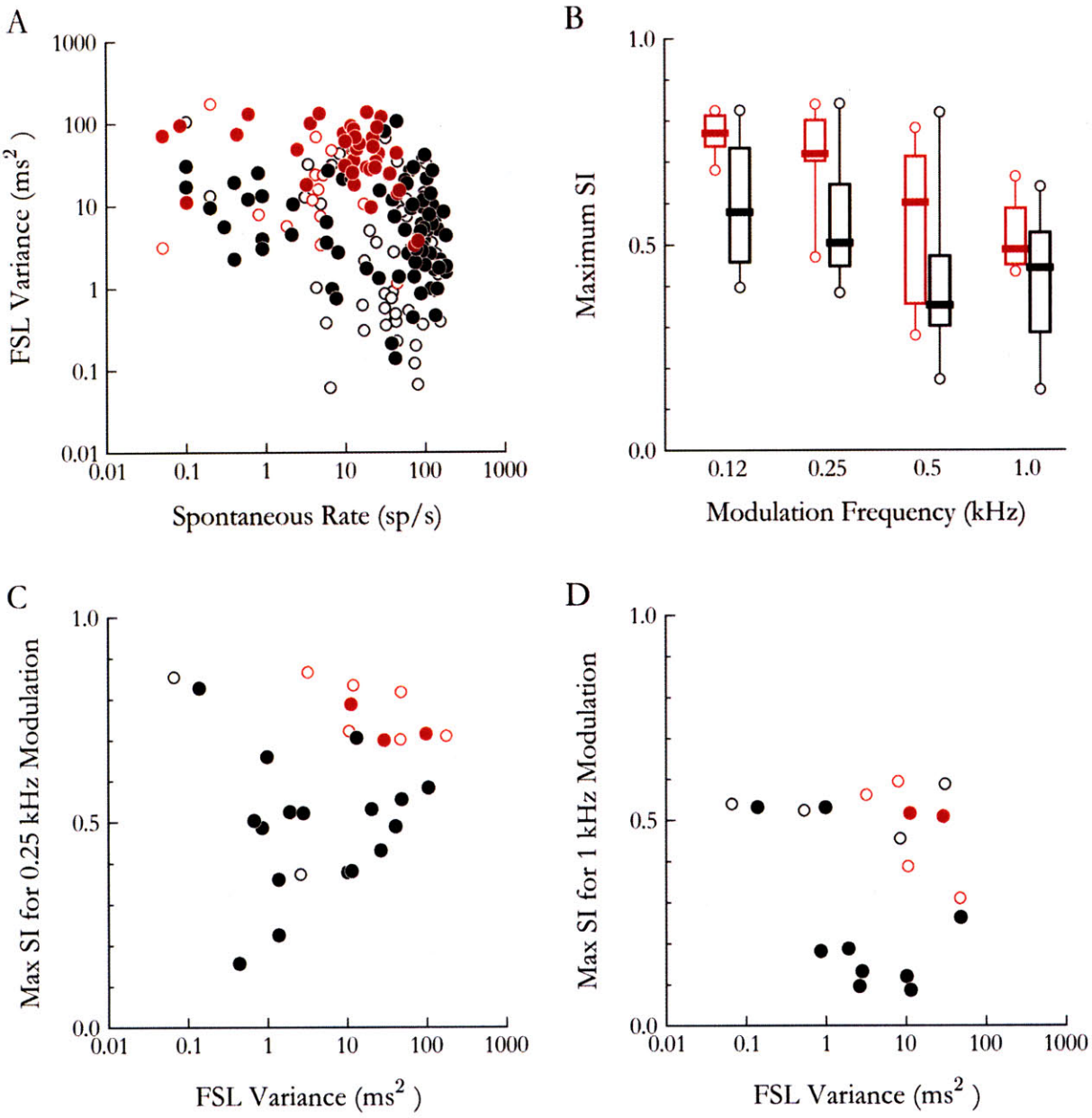

Figure 18 – Mutant AN fibers have a greater FSL variance but better synchrony than wild-type. A: Plot of FSL variance as a function of peak rate in response to 200 to 1000 presentations of a 50 ms tone burst gated with a 2.5 ms $\cos^2$ envelope. FSLs were collected by discarding repetitions during which no spike occurred during the first 50 ms and taking the first spike from the remaining repetitions. As with other figures, peak rate was computed as the maximum onset rate using a 0.1 ms bin. B: As in Figure 13, these box-whisker plots summarize the 1st, 25th, 50th, 75th and 99th quantiles of the distribution of maximum synchrony indices observed for each modulation frequency. C and D: Relationship between maximum synchrony as assessed by transposed tones and FSL variance as assessed by the same tone bursts used for (A) for a modulation frequency of 0.25 (C) and 1 kHz (D).

Although true impulse stimuli do not occur in nature, they are a very useful concept for understanding the response of a complex system, such as the IHC synapse. Consider the hypothetical impulse response of the IHC synapse in which there is an infinitely brief and infinitely high spike of calcium concentration. For purpose of discussion, we assume that the distribution of spike times in response to this impulse are normally

distributed with the width of the distribution reflecting timing precision and the area under the distribution reflecting reliability (Figure 19A). If we assume there is no spontaneous activity, then the variance of the FSL distribution in response to this impulse does an excellent job of capturing the precision of spike timing, regardless of whether a spike is produced for every impulse or not (compare red and black lines in Figure 19B).

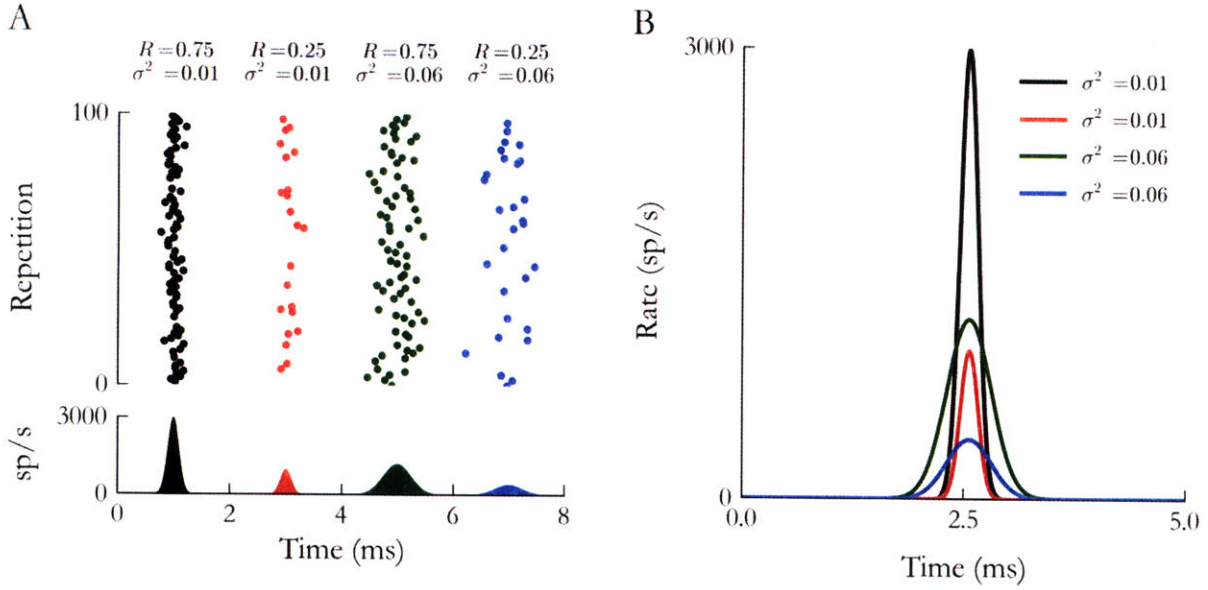

Figure 19 – Impulse response of a model neuron for different combinations of spike precision and reliability
Impulse response of a model neuron for different combinations of precision, expressed as variance of the spike times in ms (we assume spike times in response to an impulse are normally distributed), and reliability, expressed as the number of spikes per impulse with 1 indicating a spike is produced on every cycle. A: The text at the top indicates the precision (σ^2) and reliability (R) for the corresponding dot-raster plot showing the distribution of spike times. The corresponding PST response for the neuron is shown below each dot-raster plot. B: Expected distribution of FSLs in response to the impulses shown in (A). Legend indicates the expected variance of the FSL distribution. The expected value of the FSL distribution was computed as the joint probability of a spike at a given time and no spike occurring before that time[8]. Specifically, $P_{FSL} = P(\text{spike}_{[t, \Delta t)} \text{ and no spike}_{[0, t)}) = P(\text{spike}_{[t, \Delta t)})*P(\text{no spike}_{[0, t)})$. The expected value of the variance for the distribution is computed as a weighted variance using the expected value of the FSL distribution as the weighting factor.

However, as we expand our analysis to more complex synaptic drive which includes the effects of spontaneous activity, sustained depolarization and adaptation, interpreting precision from the FSL distribution becomes much more difficult. The impulse response reflects the transformation of synaptic drive into an instantaneous spike rate, so we can compute the synaptic drive under conditions of degraded reliability or precision by convolving it with the appropriate impulse response (Figure 19A). As shown by the expected FSL distribution in response to a tone burst (Figure 20B, D), reliability is the primary factor influencing the variance of the distribution in contrast to precision, which has very little effect on the variance. This is precisely the effect observed in our single-unit data in response to tone bursts: mutant AN

[8] This approach assumes that the probability of a spike in $[t, \Delta t)$ is independent of the probability of a spike in $[0, t)$. Potential effects of refractoriness on the fiber are ignored for the sake of simplicity.

fibers have lower driven rates, which reflect degraded reliability, and thus a greater FSL variance. Analyzing the variance of the FSL distribution is further complicated by the presence of mid-to-high levels of spontaneous activity in some neurons (Figure 20D).

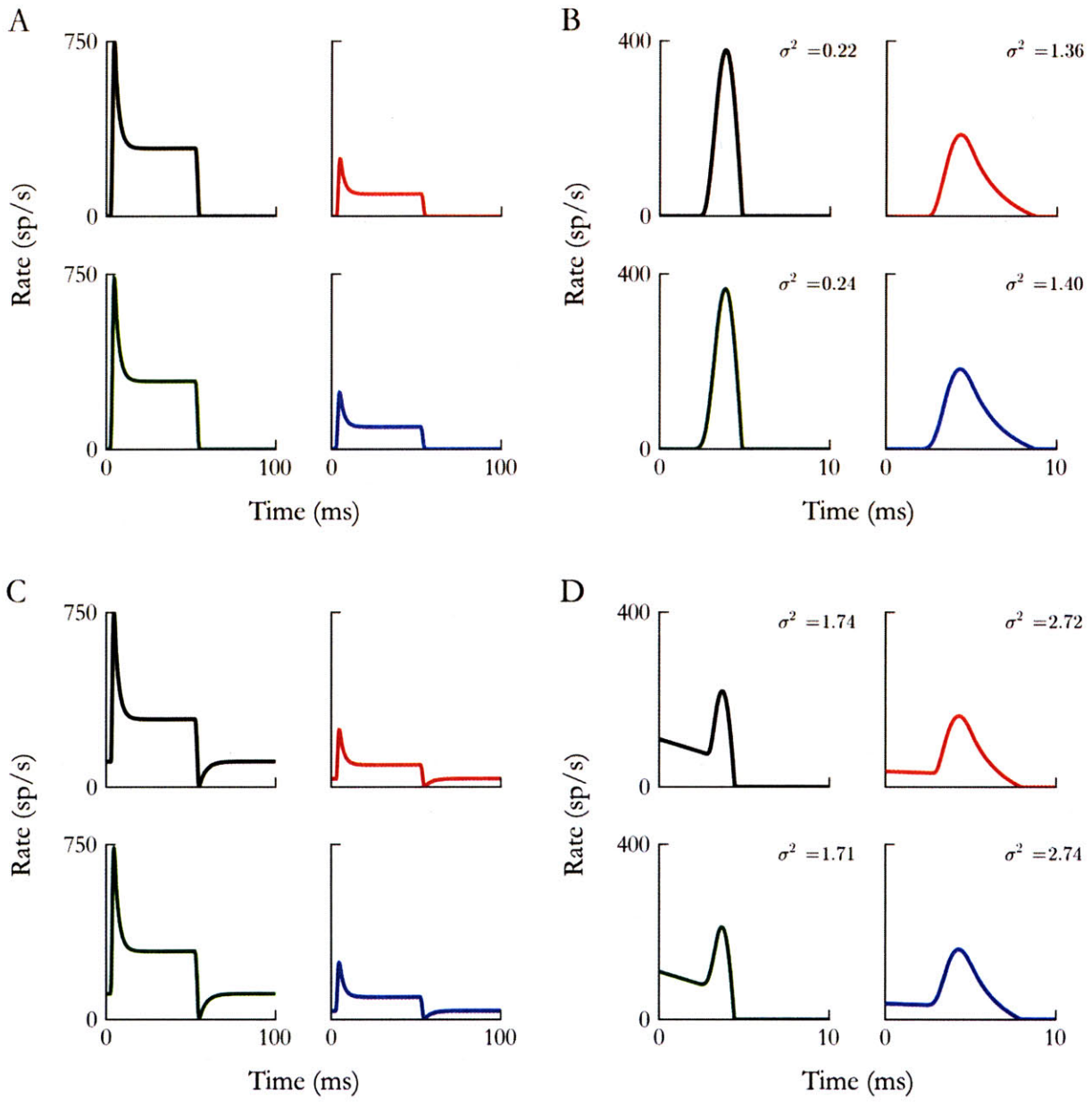

Figure 20 – Effects of spike reliability and precision on the distribution of the first spike latencies of a model neuron responding to a 50 ms tone burst gated by a 2.5 ms $\cos^2$ ramp. A and C: PST histogram showing the driven rate of a neuron with no spontaneous activity (A) and a moderate level of spontaneous activity (C). B and D: Expected FSL distribution derived from the corresponding PST response in A and C. The variance for each distribution is indicated in the upper right corner of the plot. Color key and values for precision (σ^2) and reliability (R) are the same as Figure 19.

Unfortunately it is very difficult to separate out reliability and precision without an appropriate model of spike generation that accurately captures various aspects such as past spiking history and the contribution of various response covariates. As shown above, FSL variance is not a sensitive metric of timing precision and

better reflects the reduced spiking activity of the neuron. Not surprisingly, FSL variance is strongly correlated with peak rate (Figure 21), with high SR fibers tending to show larger variance than low SR fibers of similar peak rate (compare open circles with closed circles in Figure 21).

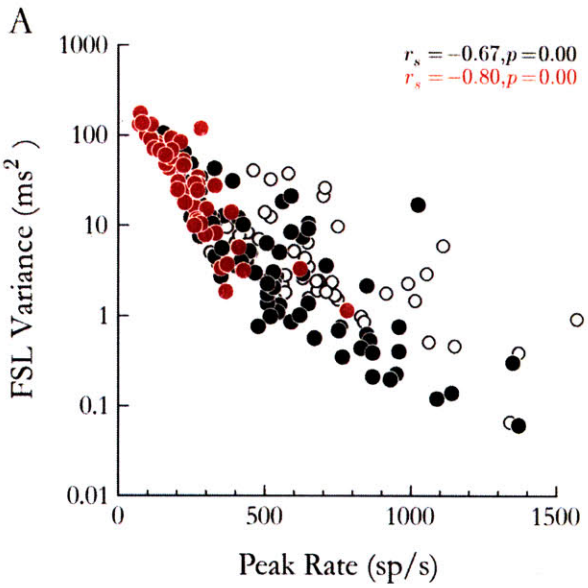

Figure 21 – FSL variance versus peak rate in response to 200 to 1000 presentations of a 50 ms tone burst gated with a 2.5 ms cos^2 envelope. FSLs were collected by discarding repetitions during which no spike occurred during the first 50 ms and taking the first spike from the remaining repetitions. As with other figures, peak rate was computed as the maximum onset rate using a 0.5 ms bin. Open circles indicate fibers with SR > 80 sp/s.

To analyze precision, we must introduce rapid temporal modulations into the envelope of the receptor potential via stimuli such as transposed tones and observe whether the output of the neuron can track these temporal fluctuations. As shown by model responses to transposed tones, phase-locking offers an excellent method to assess the precision of spike timing. Even if reliability is degraded by a factor of 2 to 3, synchrony is unimpaired since it is a normalized metric that reflects the average vector strength of the sample. Likewise, similar metrics used to assess synchrony which are normalized by firing rate, such as shuffled autocorrelograms (Louage et al., 2004), will not be affected by degraded reliability. This normalization process means that the presence of spontaneous activity, which occurs uniformly throughout the cycle, severely degrades synchrony (compare panels B and D of Figure 22) since it generates a large number of spikes with random phase that sums to zero. However, the synchrony of two neurons of similar spontaneous rate can be directly compared (Figure 22D). Although mutant AN fibers may have better synchrony, on average, than wild-type, they are comparable when matched for SR (Figure 23).

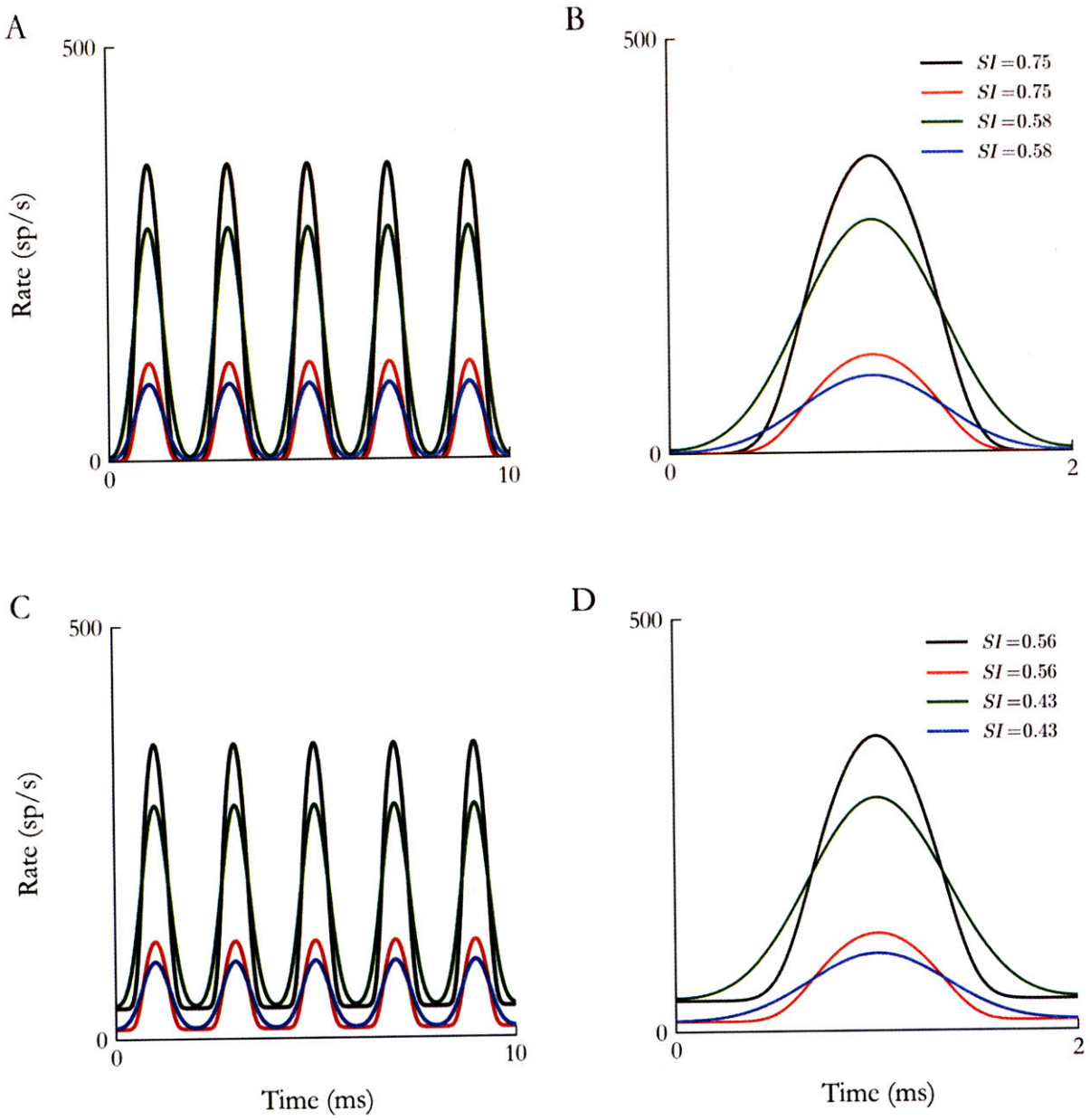

Figure 22 – Effects of spike reliability and precision on phase-locking in a model neuron responding to a transposed tone modulated at 0.5 kHz. A and C: PST histogram showing the driven rate of a neuron with no spontaneous activity (A) and a moderate level of spontaneous activity (C). B and D: Expected distribution of spike times over a single period of the modulator, derived from the corresponding PST response in A and C. Legend indicates the resulting SI. Color key and values for precision (σ^2) and reliability (R) are the same as Figure 19.

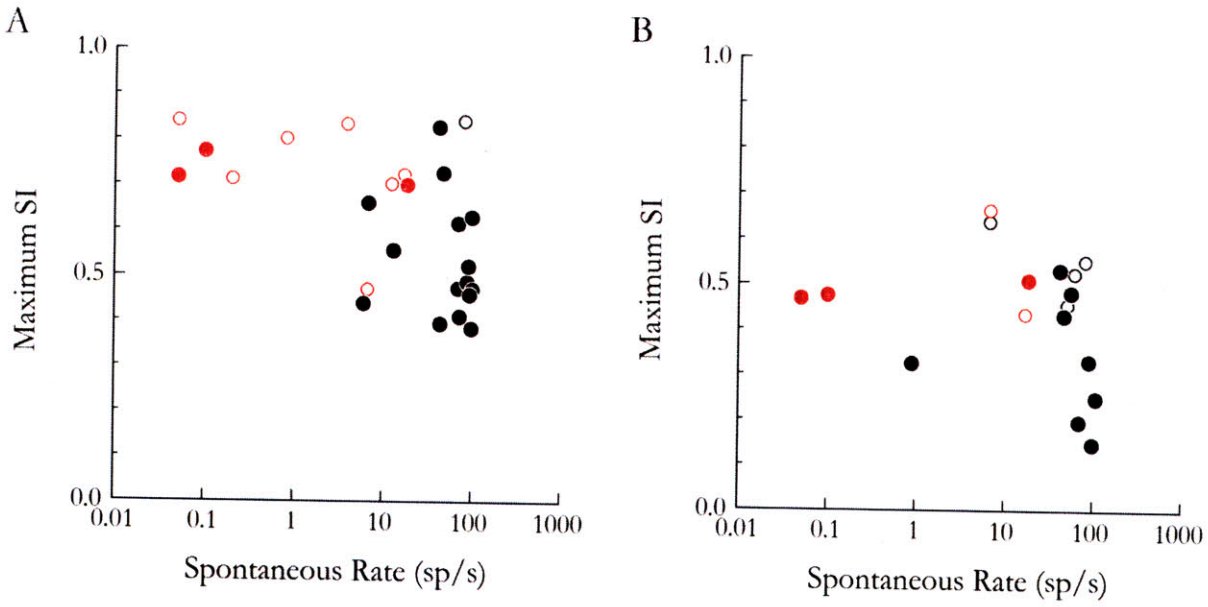

Figure 23 – Maximum synchrony to transposed tones as a function of SR for modulation frequencies of 0.25 (A) and 1.0 kHz (B). Only data from synchrony-level functions that showed saturation were included.

Transposed tones allow us to introduce temporal fluctuations into the receptor potential of IHCs situated in high-frequency regions of the cochlea and, thus, infer the excitatory drive acting on the post-synaptic membrane. If temporal precision of neurotransmitter release and EPSCs are intact, the AN fiber will preferentially fire at multiples of the modulator period resulting in an ISI histogram that shows sharp peaks at multiples of the modulator period (Figure 24). Any degradation of temporal precision will appear as a "smearing" of the peaks in the ISI histogram. Although slow temporal fluctuations on the order of 8 ms (the slowest modulation frequency tested) may not reveal a subtle degradation in timing precision, we tested modulation frequencies up to 1 kHz where the modulator period becomes sufficiently small that subtle deviations in spike timing would become readily apparent. Degraded reliability results in a greater proportion of long ISIs while degraded precision would result in a smearing of the peaks in the ISI histogram. Thus, transposed tones clearly illustrate the distinction between reliability and precision. Indeed, our ISI data from transposed tones demonstrates that mutant AN fibers retain the ability to track temporal modulations in the envelope, although reliability is severely degraded (Figure 24B).

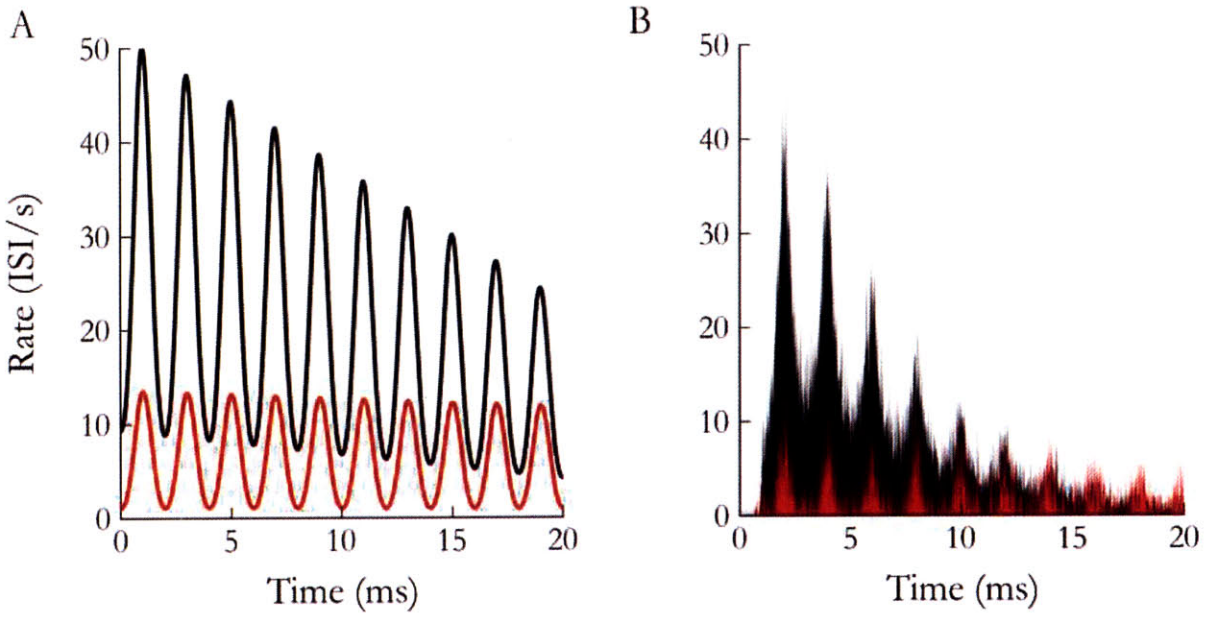

Figure 24 – Distribution of ISIs in response to a transposed tone modulated at 0.5 kHz. A: Expected distribution of ISIs assuming temporal precision is identical between wild-type and mutant and reliability is approximately 2.5 times greater in wild-type. B: Actual distribution of ISIs as determined from experimental data averaged across all units.

6.2.1 Relevance to other studies using FSL variance as a metric

A study of AN fibers in mice lacking large conductance voltage and calcium activated potassium (BK_{Ca}) channels showed that FSL variance was increased by up to two orders of a magnitude in BK_{Ca}-deficient AN fibers (Oliver et al., 2006). However, FSL variance retains a strong correlation with driven rate. Our analysis suggests that the increased FSL variance in BK_{Ca}-deficient AN fibers is due to the observed reduction in mean and peak and adapted rates rather than degraded spike timing. This does not rule out possible degradation in the temporal precision of spike timing in the absence of BK_{Ca} channels since FSL variance would not reflect degraded synchrony. Indeed, the authors tentatively report that there appeared to be degraded synchrony in the mutants; however, their sample size was too small to draw any definitive conclusions, particularly considering the increased SR observed in mutant AN fibers. This degraded synchrony was attributed to the slower membrane time constant observed in BK_{Ca}-deficient IHCs, which leads to a greater DC shift and attenuated AC component. The availability of transposed tones offers an excellent way to assess this hypothesis as the modulation transfer function (i.e. SI_{max} of the AN fiber as a function of modulation frequency) would be expected to roll-off at much lower modulation frequencies. Since the membrane time constant of mutant IHCs is three times longer than wild-type, it is reasonable to hypothesize that synchrony would begin to degrade at modulation frequencies approximately three times slower than the cutoff in wild-type.

6.2.2 Cellular mechanisms governing reliability and jitter

Reliability requires that a spike be produced on each suprathreshold stimulus, while precision requires that the window over which the spike can occur be kept as small as possible, even if it means that a spike cannot be produced each time. AN discharge is probabilistic by nature with an inherent amount of noise built-in that can influence precision and reliability. Since action potentials are extremely reliable, once initiated, with

virtually no timing jitter in the propagation time of the action potential (Lass and Abeles, 1975), the majority of noise must arise from pre and post-synaptic mechanisms at the ribbon synapse itself. Our conclusion that precision is intact but reliability is degraded allows us to make inferences regarding how pre-synaptic mechanisms might be altered in the absence of the ribbon.

Sound-evoked changes in IHC receptor potential govern the open probability of calcium channels which, in turn, modulates the calcium influx that drives neurotransmitter release. A variety of factors can shape the time course of intracellular calcium concentration including channel kinetics, release from intracellular calcium stores, diffusion to the release site, buffering and extrusion from the cytoplasm. The gating kinetics of $Ca_v1.3$ channels, the dominant source of the calcium current in IHCs, are on the order of 100 to 500 μs (Zidanic and Fuchs, 1995) with inactivation occurring over a much longer time scale of seconds (Johnson and Marcotti, 2008). Thus the resulting influx is quite capable of tracking rapid fluctuations in the IHC receptor potential. For transient or rapidly modulated stimuli, such as clicks and transposed tones, IHCs depolarize briefly, resulting in a transient calcium influx. Only vesicles immediately adjacent to calcium channels are exposed to elevated calcium concentrations sufficient to drive exocytosis, and then, only for a very brief time window before excess calcium ions are sequestered, extruded or diffuse away, thus resetting the probability of release back to spontaneous levels within a fraction of a millisecond. Should a synaptic vesicle not be docked immediately adjacent to these calcium channels, exocytosis will not occur. In such a system, exocytosis is very precise, but potentially not reliable depending on the size of the RRP. In the presence of a large RRP in which each calcium channel is associated with a release-ready vesicle, exocytosis will be reliable. If the RRP is reduced in size, reliability would be reduced proportionately: this is precisely the effect we see in the reduced onset rates and decreased probability of firing on each cycle of a modulated tone (Figure 25A).

In the presence of a smaller RRP, it is possible to recover reliability, but only at the expense of temporal precision. Through some combination of mechanisms which extend the spatial and temporal course of the calcium transient, such as slower deactivation of calcium channels, lower cooperativity of release (i.e. the number of calcium ions required to drive exocytosis) and calcium-induced calcium-release from intracellular stores, the calcium influx could drive exocytosis of outlying vesicles. However, the variable distance between these outlying vesicles and the calcium channel, combined with additional noise (e.g. "random walk" of calcium ions and chance fluctuations of calcium channel open probability), will severely degrade temporal precision of exocytosis.

Postsynaptic mechanisms also contribute to reliability and precision including diffusion of glutamate, postsynaptic receptor affinity and kinetics and clearance of glutamate from the cleft. A key factor influencing reliability is the amount of glutamate required to open a sufficient number of glutamate receptors to drive the postsynaptic membrane to threshold. Lower receptor affinities or a higher firing threshold will result in degraded reliability. Precision can be degraded if the postsynaptic receptors are not situated immediately opposite the sites of exocytosis (i.e. the base of the presynaptic ribbon), thus introducing some variability in diffusion time across the cleft.

Discussions of mechanisms which govern precision and reliability are fairly straightforward when considering brief, transient depolarizations. However, extending our discussion to longer depolarizations illustrates why the variance of the FSL is an ill-defined metric for considering precision and reliability of the system as the underlying processes become intertwined. Long-duration stimuli such as 50 ms tone bursts result in a sustained depolarization of the IHC, which lead to two parallel processes that may govern the probability of a

spike. First, although the initial transient elevation of calcium may be rapidly sequestered, the buffer in the immediate vicinity of calcium channels presumably saturates, allowing for diffusion of calcium to vesicles not immediately adjacent to the channels. Second, as the duration of depolarization increases, the probability of a calcium channel (with a release-ready vesicle potentially associated with it) opening at any given point during that time also increases. Even if the neuron fails to produce a spike immediately at stimulus onset (i.e. an unreliable neuron), the probability of a spike remains high, and the FSL distribution includes some of these later-occurring spikes (Figure 25B). As exocytosis continues, neurotransmitter may build up slightly in the synaptic cleft, thus increasing the probability of reaching firing threshold.

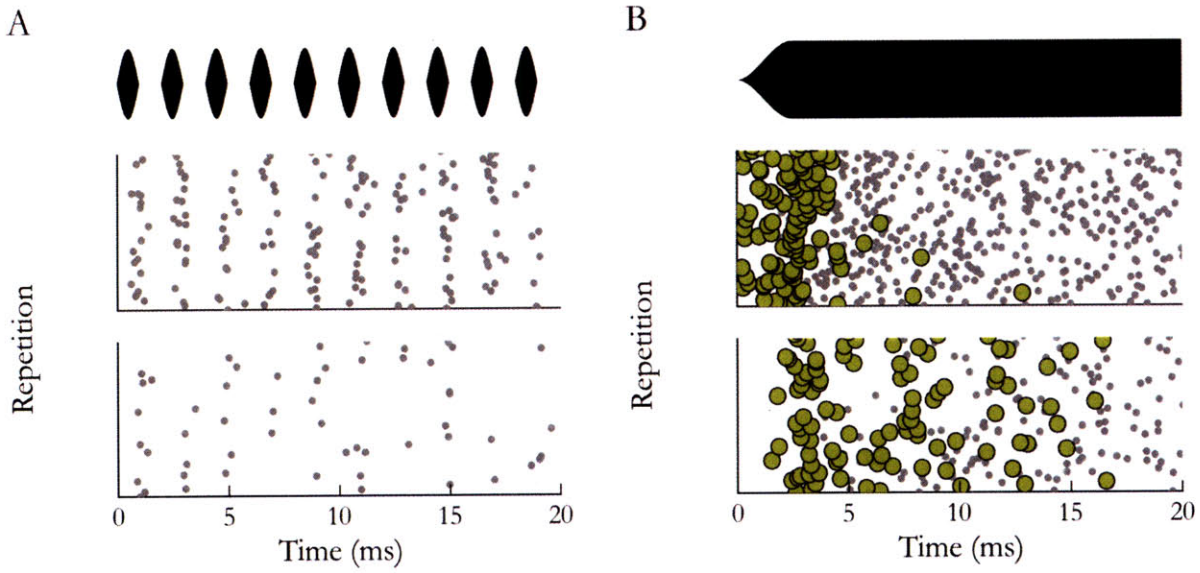

Figure 25 – Dot-raster plots showing spike times (grey) from a wild-type (top) and mutant AN fiber (bottom) for 100 repetitions of a transposed stimuli (A) and 100 repetitions of a 50 ms tone burst gated with a 2.5 ms $\cos^2$ ramp (B). Yellow markers in (B) indicate time of the first spike on each repetition. The envelope of the stimuli used is shown above the respective dot-raster plots.

Interestingly, the mechanisms that contribute to a very reliable, temporally precise system can also result in a higher level of spontaneous activity. Although it's not clear what drives spontaneous release or what pool of synaptic vesicles participates, one possibility is that spontaneous activity arises from chance opening of calcium channels at resting potential. If a large fraction of calcium channels have an associated release-ready vesicle, then chance openings of the channel at rest will drive exocytosis of this vesicle. A less reliable system with a smaller RRP or higher post-synaptic threshold will have a lower spontaneous rate. Such noise could be filtered out via mechanisms such as requiring the summed current of multiple nearby calcium channels to drive exocytosis (thus averaging out stochastic noise of calcium channel opening) or multiquantal release to drive spiking activity. However, filtering out such noise comes at the expense of degraded reliability, particularly at near-threshold levels where the depolarization may increase open probability of calcium channels only slightly.

Our phase-locking data to transposed tones clearly illustrate that ribbon-deficient AN fibers remain capable of tracking rapid temporal fluctuations up to 1 kHz with no apparent degradation in spike timing, although

the probability of neurotransmitter release is greatly reduced, presumably due to the decreased number of release-ready vesicles that are typically associated with the ribbon.

6.3 Psychophysical Correlates

In the context of ribbon synapses, in which an analog stimulus, receptor potential (i.e. "probability of exocytosis") is converted into a "point" code where the intervals between individual neurons carry information about the probability distribution that gave rise to the spike train. The challenge of the central auditory processor is to reconstruct the external scene based solely on the information encoded in these interspike intervals across multiple neurons. Inferences can be made about the external stimulus that gave rise to the spike pattern. As with any probabilistic system, there is a range of external stimuli that could lead the observed spike distribution. Thus, the central processor must weight its inference by the likelihood that it is the correct one. As the information available to the central processor increases, the likelihood that the inference is correct becomes stronger as other hypotheses regarding the nature of the external stimulus can be ruled out. There is indication that the brain operates in such a fashion, where the "salience" of the stimuli corresponds with increasing amount of information that can be used for such inferences (Pouget et al., 2003; Ma et al., 2006, 2008; Beck et al., 2007; Paninski et al., 2007).

Although temporal precision may remain intact in ribbon-deficient AN fibers, the severely degraded reliability will reduce the amount of information available to the central processor, resulting in great difficulty in reconstructing the temporal structure of the stimulus that gave rise to the spike train. For periodic signals, the central processor could recover the necessary information by integrating over long samples in time; however, many naturally-occurring sounds tend to be transient or aperiodic. An alternate approach would be to boost the number of AN fibers, perhaps by a factor as high as 3.6 as suggested by the reduction of onset rates in response to clicks. This runs into obvious morphological and metabolic constraints that may be limited by the biology of the organism. The ribbon may have evolved to compensate for such limitations and ensure sufficient information is available to the CNS to reconstruct the external scene.

The ability to resolve temporal structure of stimuli is key for a number of psychophysical tasks including sound localization (Wightman and Kistler, 1992; Macpherson and Middlebrooks, 2002), discrimination of continuous sounds and speech intelligibility (Elliott and Theunissen, 2009). Indeed, certain speech sounds can be discriminated by the rise time of the envelope (Cutting and Rosner, 1974), which is reflected in an increase of onset rate as rise time becomes more abrupt (Delgutte, 1980). Onsets are pervasive in the auditory environment, with many natural sounds and vocalizations characterized by sharp transients and rapid amplitude modulations (Lesica and Grothe, 2008; Elliott and Theunissen, 2009). Such onsets appear to hold a dominant role in auditory processing, particularly for speech communication, sound localization and hearing in noisy environments.

Although judgments of source direction appear to integrate information over tens to hundreds of milliseconds (Grantham and Wightman, 1978; Kollmeier and Gilkey, 1990; Boehnke et al., 2002), onset dominance may emphasize early stimulus segments. Indeed, such effects of onset dominance have been reported in responses of neurons of the inferior colliculus (Devore et al., 2009), which display a range of sensitivity to localization cues (Benevento and Coleman, 1970; Caird and Klinke, 1987; Delgutte et al., 1999; Chase and Young, 2005). The inferior colliculus appears to be a major center for spatial processing of auditory input, receiving convergent input from multiple ascending auditory pathways (Roth et al., 1978;

Adams, 1979; Brunso-Bechtold et al., 1981; Oliver et al., 1997). The weighting of the onset response may serve to enhance onsets in reverberant environments where reflections tend to obscure ITDs present in ongoing sounds.

A closely-related phenomenon, the precedence effect or "law of the first wavefront" (Wallach et al., 1949), operates over much shorter time scales of a few milliseconds (for review, see Litovsky et al., 1999). When two successive sounds of similar nature are presented in rapid succession, cues in the leading sound dominate the perceived location of the object. The precedence effect may be a form of echo suppression allowing the listener to rapidly focus on the actual source of the sound. Although physiological mechanisms of the precedence effect remain to be elucidated, onsets appear to strengthen the precedence effect (Dizon and Colburn, 2006).

In the presence of background noise, bassoon-deficient mice may have normal or better performance on a number of perceptual tasks. Several studies demonstrate that in quiet environments, the ratio of peak to adapted rates can be quite large; however, in the presence of background noise there is little difference between peak and adapted rates (Delgutte, 1980; Sachs et al., 1983). Instead, the bulk of information in the presence of masking noise appears to be encoded in the synchrony of discharge to the target itself (Kiang and Moxon, 1974; Sachs et al., 1983), which would be normal or better in bassoon-deficient AN fibers.

In many ways, ribbon-deficient AN fibers appear identical to low SR fibers. The loss of the highest SR fibers, which have the best relative thresholds and carry the bulk of auditory information at low sound levels, suggests that if there is, indeed, impaired psychophysical performance, it will only appear at the lowest sound levels in bassoon mutants. At high sound levels or in the presence of moderate background noise, where the responses of high SR fibers are typically saturated, bassoon-deficient mice may have normal or better performance on a number of perceptual tasks.

6.4 Statistical models of coincidence detection

Many central auditory neurons, such as the coincidence detectors of the medial superior olive (MSO) which are sensitive to differences in ITD as small as 10 μs (Batra et al., 1997; Goldberg and Brown, 1969; Spitzer and Semple, 1995; Yin and Chan, 1990), are sensitive to simultaneous input. Consequently, the performance of such downstream neurons would be impaired, particularly those that rely on a few, large inputs such as the one to four endbulbs onto the spherical bushy cells of the anteroventral cochlear nucleus (Ryugo and Sento, 1991; Nicol and Walmsley, 2002) and coincidence detectors of the medial superior olive. In contrast, cells that receive many more inputs may be able to partially compensate for the reduced input by fine-tuning the contribution of individual synapses. Consistent with this argument, ABR wave 3, which is thought to reflect contribution of the spherical bushy cells (Melcher and Kiang, 1996), was reduced by a similar factor as wave 1 (Figure 4C). In contrast, the near-normal ABR wave 2 amplitude reflects the contribution of globular bushy cells which receive convergence of many more auditory nerve fibers (Spirou et al., 2005).

The physiological basis of the dominance of onsets in many perceptual tasks may be due to the presence of specialized neurons that primarily respond to stimulus onset, such as the aptly-named onset neurons of the cochlear nucleus. Modeling studies suggest that neurons such as the MSO coincidence detectors and onset neurons sample across multiple subthreshold synapses, firing only when a sufficient fraction of inputs are activated simultaneously. A number of models of auditory neurons are based on an integrate-and-fire approach, in which a number of neurons with weak inputs synapse onto the soma or dendrites of the model

neuron. Since each synapse provides a subthreshold input, the summation of EPSCs from several synapses are required to bring membrane potential to firing threshold (for review, see Koch and Segev, 2000). By varying parameters, such as number, firing threshold, location and strength of AN synapses, these models do an excellent job of predicting response types of several auditory neurons in the cochlear nucleus (Zhang and Carney, 2005; Kalluri and Delgutte, 2003a, 2003b). Such models provide a relatively straightforward framework to help illustrate the importance of rapid onsets for downstream auditory neurons.

Since the discharge of each AN fiber is statistically independent, then the output of a coincidence detector with a given number of inputs, N, with a given rate parameter, $\lambda_{in}(t)$, can be determined by binomial statistics. The probability of a single input of producing a spike in a time interval, Δt, is $\lambda_{in}(t)\Delta t$. If all N inputs must be active within this interval to produce an output spike, then the output rate of the coincidence detector can be estimated from the joint probability of each input producing a spike within this time window:

$$\lambda_{out}(t) = \frac{1}{\Delta t}(\lambda_{in}(t)\Delta t)^N$$

$$\lambda_{out}(t) = \lambda_{in}^N(t)\Delta t^{N-1}$$

Although this approach ignores many factors such as the EPSC time course, varying synaptic strength and dendritic filtering (Sumner et al., 2009) and that the coincidence detector probably doesn't require synchronous firing of all inputs to produce an output spike, this approach helps illustrate how a reduction in rate might impair the performance of downstream auditory neurons. To estimate the reduction in output of the coincidence detector given a reduction in the input rate:

$$\frac{\lambda_{outWT}(t)}{\lambda_{outKO}(t)} = \frac{\lambda_{inWT}^N(t)\Delta t^{N-1}}{\lambda_{inKO}^N(t)\Delta t^{N-1}}$$

$$\frac{\lambda_{outWT}(t)}{\lambda_{outKO}(t)} = \left(\frac{\lambda_{inWT}(t)}{\lambda_{inKO}(t)}\right)^N$$

Thus, the output of the coincidence detector will be reduced by a power that is determined by the number of inputs converging onto the detector. For the simplest case where a single neuron from each ear synapses onto the coincidence detector, the reduction in ribbon-dependent onset rates by a factor of 1.4 to 3.6 would result in a reduction in the output of the coincidence detector by a factor of 2.0 to 13.

For neurons that require coincident activation of only a fraction of many subthreshold synapses, such as onset and onset choppers of the CN, the output of the coincidence detector can be determined by the combination of all possible inputs that could result in an output spike (Kalluri and Delgutte, 2003b):

$$\lambda_{out}(t) = \frac{1}{\Delta t}\sum_{i=n}^{N}\binom{N}{i}(\lambda_{in}(t)\Delta t)^i(1-\lambda_{in}(t)\Delta t)^{(N-i)}$$

Of particular note is the relatively steep relation between the mean input rate of the AN fibers and the output rate of the model neuron for large numbers of convergent inputs (Figure 26).

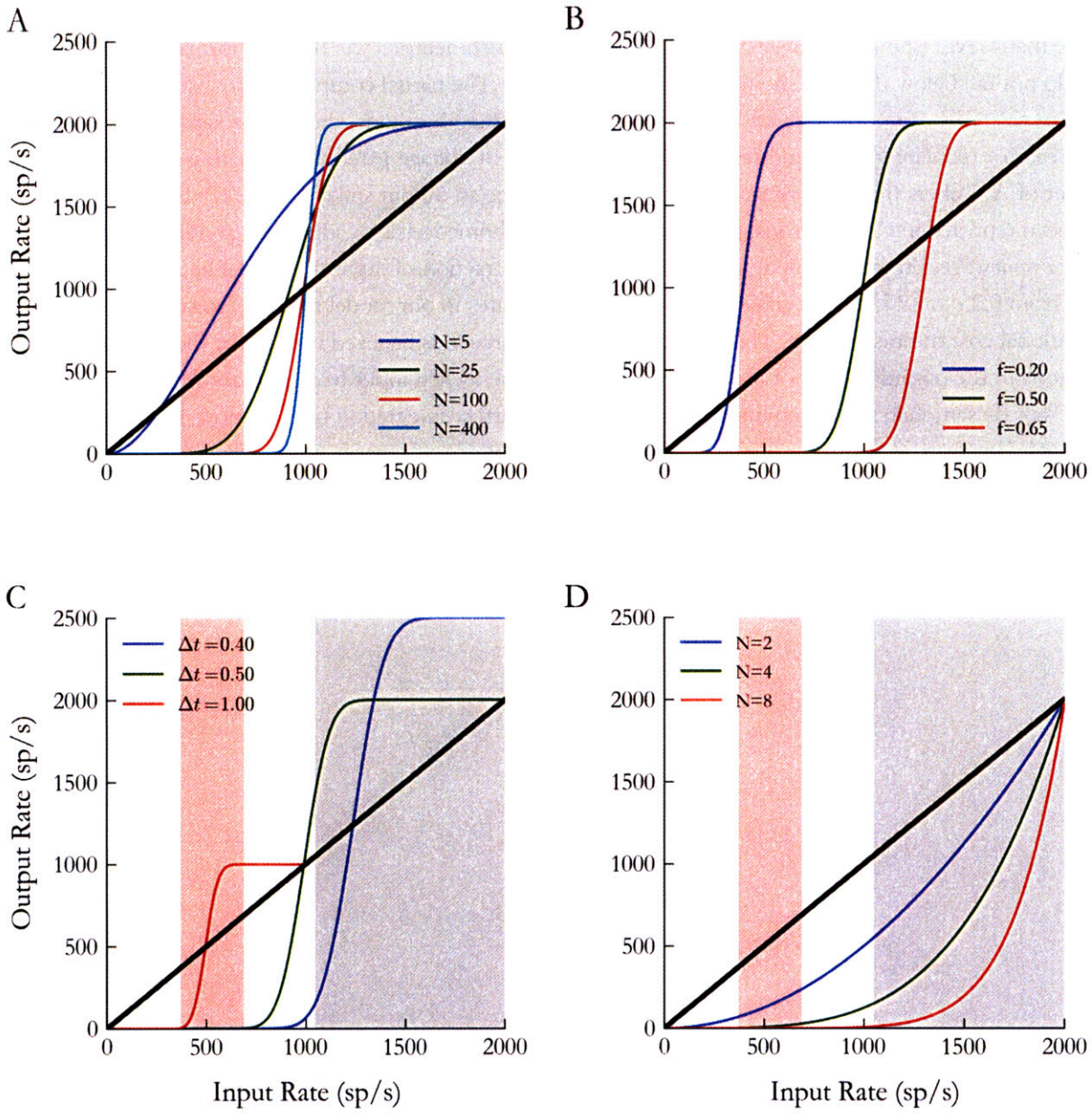

Figure 26 – Output rate of a coincidence detector receiving multiple subthreshold inputs of given input rate. The curves represent the transfer function of the coincidence detector based on a statistical model that considers the number of inputs, N, of which a given fraction, f, need to be active over an integration window of Δt to produce an output spike. To help illustrate the significance of the loss of the ribbon, the range of onset rates in response to clicks (specifically the 25th to 75th percentile) are shown by the shaded backgrounds for mutant (pink) and wild-type (grey). Note that mutant onset rates have been multiplied by a factor of 1.8 to compensate for the reduced calcium current. Black lines indicate unity (i.e. a neuron that faithfully replicates a single primary input from a single AN fiber). A: Transfer functions with Δt = 0.5 ms and f = 0.5 for various inputs, N. B: Transfer functions with Δt = 0.5 ms and N = 100 for various fractions, f. C: Transfer functions with N = 100 and f = 0.5 for various Δt. D: Transfer functions for Δt = 0.5 ms and f = 1.0 for various N.

As the number of inputs onto a single integrate-and-fire neuron increase, the transfer function becomes steeper. In contrast, increasing the fraction of the inputs that must be active over a given time window shifts

the transfer function to the right. The steep input-output relationship of integrate-and-fire neurons which receive many ($N \geq 25$) inputs suggests that the response of such neurons will be near-normal provided onset rates do not fall below the "threshold" input rate (Figure 27). The partial compensation observed in later waves of the ABR can potentially arise from increasing the strength of individual AN synapses onto globular bushy cells or reducing the firing threshold via up-regulation of voltage-gated channels, thus reducing the number of AN fibers that must fire simultaneously to produce an output spike (Figure 27). Such mechanisms have been reported in CNS neurons, putatively as a form of homeostasis to adjust the overall excitability of a cell (for review, see Abraham, 2008). Simply by reducing the fraction of inputs that must be simultaneously active from 0.25 to 0.15, we can achieve near-normal onset rates in our model neuron. However, this comes at additional cost of noisy output. This integrate-and-fire approach is believed to underlie the enhancement of synchrony in the output of cells of the AVCN receiving phase-locked input from primary AN fibers (Joris et al., 1994a). By sampling across multiple inputs and using a narrow integration time window, synchrony can be enhanced. However, as shown in our statistical analysis, alterations of synaptic strength or increasing the integration window will decrease the signal-to-noise ratio and temporal precision of the system.

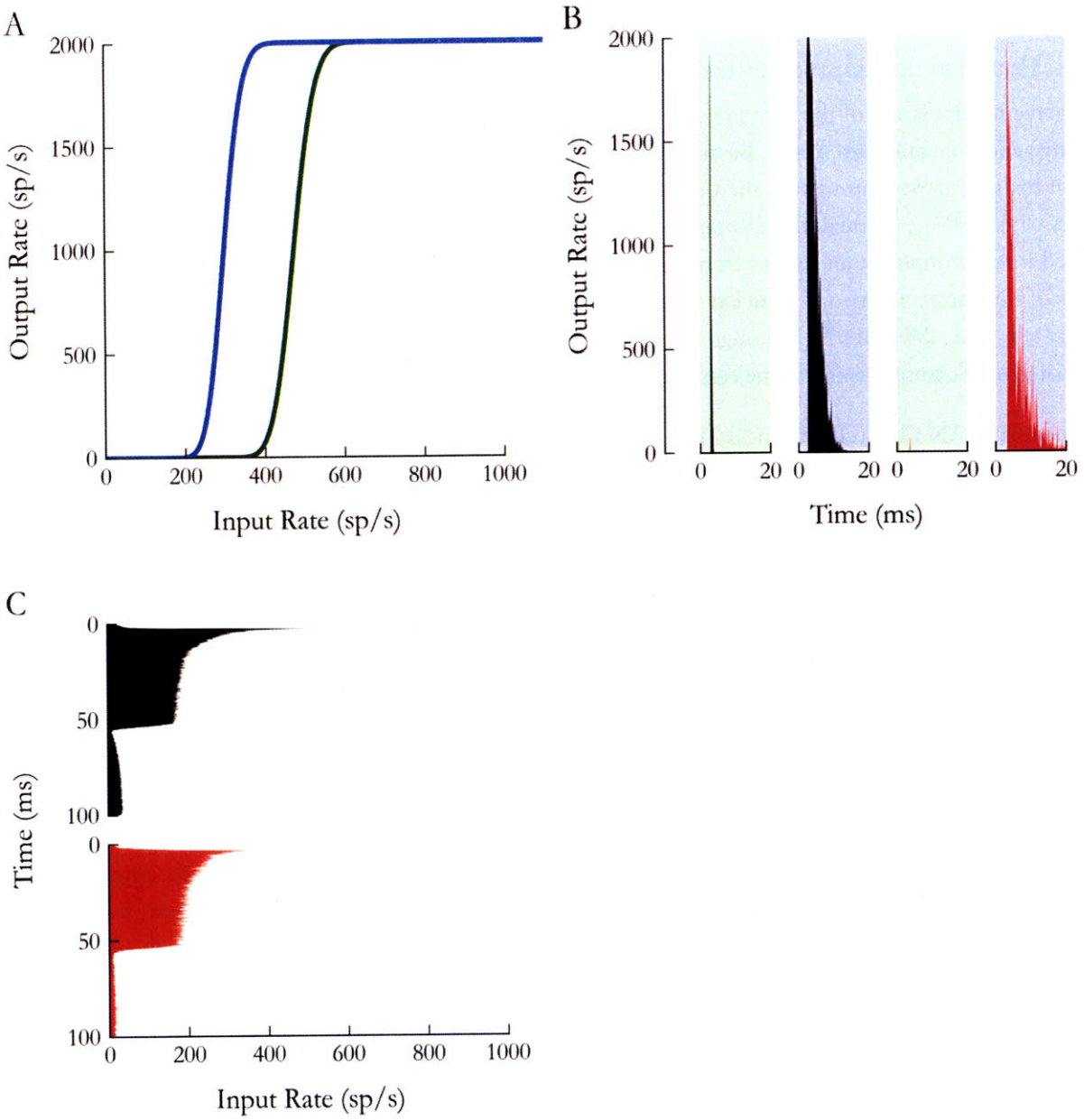

Figure 27 – Output of a coincidence detector neuron with 400 convergent inputs, 100 (green) or 80 (blue) of which must be simultaneously active over a time window of 0.5 ms to produce an output spike. A: Input-output function for the coincidence detector. B: PST histogram of output of coincidence detector given the wild-type (black) or mutant (red) input shown in C. Background indicates the corresponding transfer function used to compute the output. C: PST histogram of input. These histograms were obtained by averaging the responses to 50 ms tone bursts of all AN fibers with CF < 16 kHz in our database. Prior to averaging the histograms, they were aligned so that the peak latency of each individual fiber was equal to the mean latency for its corresponding genotype. The mutant PST histogram was multiplied by a correction factor of 1.8 to compensate for the reduction in calcium current (see section 6.1).

6.5 Alternate explanations for the reduction in spiking activity

6.5.1 Potential developmental factors due to the mutation

Transgenic manipulation of the germline often results in a complex phenotype due to the pleiotropic nature of many genes (Yu and Zuo, 2009). Bassoon, being one of the largest structural proteins found at the active zone of many synapses throughout the CNS, is no exception (tom Dieck et al., 1998; Richter et al., 1999; Fenster et al., 2000). Although there appear to be no structural abnormality at the synaptic level, bassoon is required for neurotransmitter release from a subset of glutamatergic synapses (Altrock et al., 2003). Moreover, studies of the cortex in bassoon-deficient mice reveal cytoarchitectural abnormalities and altered brain activity (Angenstein et al., 2008, 2007). Although a reduction in AN activity could be attributed to a number of pre and post-synaptic impairments, some can be ruled out.

Our analysis of AN fiber refractoriness makes it very unlikely that a post-synaptic deficit might reduce driven rates via a prolonged refractory period (Figure 15). Furthermore, our estimate of the refractory period is in close agreement with prior analysis from other species. Using long duration recordings of spontaneous activity in cat AN fibers, Heil et al. (2007) suggests that the absolute refractory period (RP) and relative RP are uniform across all fibers at 0.59 ms and 0.65 ms, respectively. Based on recordings from the adapted portion of PST responses in cat AN fibers, Li and Young (1993) report absolute RPs of 0.56 to 0.86 ms, with the time constant of the relative RP inversely correlated with SR, ranging from 0.2 for a fiber of 300 sp/s to 2 ms for a fiber of 30 sp/s.

The cochlea also receives efferent feedback via the olivocochlear system, which arises from the superior olivary complex and innervates cochlear sensory cells and afferent neurons. This system can be divided into two subgroups – the medial olivocochlear system (MOC) which arises from the medial superior olive and targets the basolateral membrane of OHCs and the lateral olivocochlear system (LOC) which originates in the lateral superior olive and synapses onto the base of IHCs and dendrites of AN fibers (for review, see Eybalin, 1993; Guinan, 2006; Irvine, 1992; Schwartz, 1992). Although the MOC can reduce cochlear excitability by increasing conductance of the basolateral membrane of OHCs (Guinan, 2006), there would be a corresponding elevation of DPOAE thresholds. The transient suppression in SR by approximately 10-30% during MOC stimulation (Wiederhold and Kiang, 1970; Guinan and Gifford, 1988) has been attributed to the transient decrease in the endolymphatic potential. However, such changes in SR would be CF-dependent, reaching a maximum at 10 kHz where MOC innervation density peaks in the mouse (Maison et al., 2003b). Normal DPOAE thresholds (Figure 4A) allow us to rule out inhibitory effects of the MOC as a potential cause of the reduction in rate.

The LOC, on the other hand, is hypothesized to have excitatory and inhibitory roles, possibly through the actions of distinct neurotransmitters or cytochemical subgroups (Darrow et al., 2006b; Groff and Liberman, 2003; Maison et al., 2003a, 2003b). A single-unit study of chronic cochlear de-efferentation in cat demonstrated a reduction in mean SR of 25 sp/s among high SR units ($\geq$ 10 sp/s) (Liberman, 1990), although all other response properties of AN fibers, including maximum discharge rate, were normal. At present, we cannot rule out the possibility that all or part of the reduction in SR observed in mutant AN fibers may be due to stronger inhibitory effects of the LOC system. Indeed, there is an increase of dopamanergic LOC terminals, which are believed to have an inhibitory role, in the IHC region of bassoon-deficient ears (see section 7.3 for additional detail).

There is some indication that $Ca_v3.1$ T-type calcium channels may be present in the inner ear (Inagaki et al., 2008; Nie et al., 2008), although it remains unclear whether they are expressed in IHCs. Like other T-type calcium channels, $Ca_v3.1$ is characterized by a current that rapidly inactivates with a time constant of a few milliseconds following depolarization (Nie et al., 2008). If present in IHCs, this rapidly-inactivating current could enhance the rapid component of exocytosis by providing a large, initial transient that quickly inactivates, with the sustained component of exocytosis mediated by $Ca_v1.3$ channels, which do not inactivate. Considering that calcium current is reduced in bassoon-deficient hair cells, it is certainly possible that loss of bassoon would impair stabilization or expression of such T-type channels at the active zone, thus reducing the rapid component of exocytosis.

Of note is the reduction in $Ca_v1.3$ current observed in bassoon-deficient IHCs in vitro (Khimich et al., 2005), which suggests that, in addition to loss of anchored ribbons, structural organization of the active zone may be impaired in other respects. Since the voltage-dependence of $Ca_v1.3$ channel activation and voltage-current relationship were normal, the reduction in current was attributed to a reduction in channel number (Khimich et al., 2005). This reduction in channel number may simply reflect impaired integrity of the scaffolding at the active zone due to deletion of bassoon: e.g. the active zone may require a highly-organized scaffold to support a high density of calcium channels. Alternatively, there could also be a developmental or activity-dependent down-regulation of $Ca_v1.3$ expression via retrograde signaling pathways. Prior to the onset of hearing, ATP-mediated signaling from the greater epithelial ridge appears to drive spontaneous exocytosis in IHCs (Tritsch et al., 2007). This spontaneous activity may be essential for maturation of AN fiber synapses onto IHCs: disruption of this spontaneous activity in bassoon-deficient IHCs can conceivably lead to compensatory mechanisms run amok via altered activation of retrograde signaling pathways. Activation of retrograde signaling pathways during CNS maturation has been shown to drive changes in presynaptic excitability (for review, see Tao and Poo, 2001). Since synthesis of known retrograde messengers such as nitric oxide and endocannabinoids is driven primarily by elevated calcium levels in postsynaptic neurons, the observed phenotype would be most likely explained by disruption of a pathway known to induce long-term potentiation such as nitric oxide (Feil and Kleppisch, 2008), rather than long-term depression via a pathway such as endocannabinoid signaling (for review, see Chevaleyre et al., 2006). Although we have primarily focused on developmental and activity-dependent pathways that could lead to a failure of synaptic strengthening, it is important to recognize that some activity-dependent pathways might have the opposite effect: reduced excitatory drive could conceivably activate regulatory mechanisms that attempt to compensate via mechanisms such as increasing the surface area of the active zone, up-regulating post-synaptic glutamate receptors or increasing the number of synaptic vesicles in the terminal. If this is the case, then our data is an under-estimate of the true contribution of synaptic ribbons to synaptic transmission.

Although several factors cannot be ruled out at present, the surprising normalcy of many response properties of single AN fibers allow us to rule out a number of roles for the ribbon in synaptic function and lends circumstantial support for other hypotheses.

For the purpose of our discussion of how certain psychophysical tasks may be impaired by loss of the ribbon, we assumed that central auditory nuclei are normal, which almost certainly is not the case in bassoon mutants. Prior to the onset of hearing, auditory neurons show spontaneous activity that appears to be required for normal development of synaptic connectivity. In the deafness (dn/dn) mouse, a congenital model of deafness that lacks spontaneous activity in the AN during development, the size and strength of the endbulb of Held, a

giant calyceal synapse between AN fibers and spherical bushy cells are altered (Youssoufian et al., 2008; McKay and Oleskevich, 2007). The probable reduction in spontaneous and sound-evoked activity during development likely will lead to altered synaptic strength. Although such alterations in synaptic strength may be able to partially compensate for the reduced AN input, this may come at the cost of increased noise in the system (section 6.4). Furthermore, bassoon is ubiquitous at neuronal synapses and can impair synaptic transmission in the CNS (Altrock et al., 2003).

6.5.2 Other known causes of reduction in sound-evoked or spontaneous activity

Although alterations in pre-synaptic mechanisms involved in auditory transduction are unlikely considering bassoon is found only in the CNS. However, as mentioned earlier, development and gene regulation can be extraordinarily complex, with manipulation or removal of a single factor initiating a cascade through multiple regulatory pathways and feedback systems that ultimately alters another factor that one would ordinarily expect to be completely unrelated to the initial manipulation. Although it is not clear how loss of a CNS protein might influence various mechanisms such as endolymphatic potential or IHC receptor potential, for the sake of completeness, we discuss the known causes of reduction in sound-evoked and spontaneous activity.

A shift in the stimulus-voltage response of IHCs towards more hyperpolarized potentials could theoretically account for reduced rate while preserving tuning, dynamic range and other response metrics of AN fibers. The resting potential is primarily determined by the small cationic current through the mechanoelectrical transduction channels (MET) in the stereocilia and KCNQ-like channels in the basolateral membrane of the IHC (Oliver et al., 2003). Mechanical deflection of the stereocilia leads to an increase in the MET conductance, depolarizing the cell and activating several calcium and voltage-activated potassium conductances including BK_{Ca} (Corey and Hudspeth, 1979; Kros et al., 1998; Oliver et al., 2006; Thurm et al., 2005). A small increase in the conductance of the BK_{Ca} or KCNQ current, or a decrease in the MET current, would shift the IHC receptor potential towards more hyperpolarized receptor potentials in response to the same stimulus. Although we cannot rule out this possibility from our single-unit data, prior in vitro work in which the membrane voltage and current of bassoon-deficient IHCs was manipulated under controlled conditions still revealed a strong exocytotic phenotype (Khimich et al., 2005) that is consistent with our single-unit data.

Decreases in the endolymphatic potential, the large electrochemical gradient that provides the transmembrane current required for exquisite high-frequency hearing in mammalian cochleae (Wangemann, 2002), result in a reduction of SR and evoked rates at low sound levels (Sewell, 1984c, 1984a). Even a reduction in the endolymphatic potential of a few millivolts potentially could contribute partially to the observed reduction in SR and driven rates by reducing the driving force for the transducer current. However, these reductions would be accompanied by an elevation of DPOAE and single-unit thresholds and responses to high-level tone bursts would be normal (Sewell, 1984b, 1984c; Kemp and Brown, 1984; Ruggero and Rich, 1991).

Large conductance voltage and calcium activated potassium (BK_{Ca}) channels have been implicated in tuning the frequency selectivity of non-mammalian IHCs (Fettiplace and Fuchs, 1999; Art and Fettiplace, 1987), this does not appear to be the case in mammals (Oliver et al., 2006). However, in mice lacking functional BK_{Ca} channels, the lowest SR fibers (< 1 sp/s) were absent and adapted rates were reduced by a factor of 1.8 although peak rate was normal (Oliver et al., 2006). Although it's not clear whether this reduction in rate is

due to loss of pre-synaptic BK channels, which are dominant component of the IHC receptor potential (Thurm et al., 2005), or the post-synaptic channels found in AN fibers (Hafidi et al., 2005; Skinner et al., 2003). However, loss of the lowest SR units was attributed to a slightly depolarized resting potential of IHCs, while the reduction in adapted rates was attributed to various factors including prolonged refractoriness of the post-synaptic membrane. The large number of units with SR < 1 sp/s in bassoon-deficient ears makes BK_{Ca} channel dysfunction in IHCs unlikely, a conclusion supported by additional experiments that demonstrate normal expression and function of BK_{Ca} channels in IHCs (Moser, personal communication).

6.6 Summary

Response properties of mutant AN fibers were similar, in many respects, to wild-type. Spike intervals remained irregular, thresholds were unaffected, dynamic range was unchanged, spike synchronization to stimulus phase was unimpaired, the time course of post-onset adaptation and recovery from adaptation were normal, and the ability to sustain discharge throughout a long-duration stimulus was unaffected. These data indicate that the presynaptic mechanisms which regulate precise timing of exocytosis, graded release rates and sustained neurotransmitter release were not impaired by loss of the ribbon.

However, reductions were seen in spontaneous and sound-evoked AN fiber discharge rates, coinciding with an increased variance of first spike timing to stimulus onset. Unlike wild-type fibers, mutant fibers failed to show increased peak rate as stimulus onset became more abrupt. The reduction of peak rates and increased first spike variance likely result from degraded reliability of discharge to stimulus onset via a mechanism such as reduced RRP size.

The major functional consequence of the increased discharge rates, which appear to require a ribbon, is the resulting enhancement of the representation of rapid temporal changes in stimulus amplitude in the auditory nerve. Although temporal precision of spiking is preserved, the decreased reliability of discharge results in a severely decreased number of synchronously-firing AN fibers. The reduction in discharge rate severely degrades the ability of central auditory neurons to resolve these temporal features due to the decreased probability of the requisite number of inputs being simultaneously active over the temporal integration window. Thus many perceptual tasks that depend on powerful onsets and synchronous input from multiple AN fibers will be degraded in the absence of the ribbon.

7 Appendix – Outer hair cell and efferent phenotype of Bassoon mutants

In addition to their prominent position at the IHC synapse, synaptic ribbons are also found at a subset of OHC-type II synapses. Although the role of type II afferents in cochlear physiology is unknown, some of the type II boutons appear to form reciprocal, efferent contacts with the OHC (Thiers et al., 2008) and may function as a local feedback network that allows OHCs to modulate the excitability of nearby OHCs over short cochlear spans. Should such reciprocal synapses provide efferent feedback to OHCs that modulates their excitability, then loss of the ribbon may influence some aspects of cochlear mechanics.

7.1 Synaptic ribbon histology

To assess whether synaptic ribbons were also impaired in OHCs, their distribution and number was assessed in two wild-type ears and three mutant ears using the ribbon marker, CtBP2. Although there are antibodies that can be used to label the outline of the OHC, such as prestin, OHCs have low levels of autofluorescence that is sufficient, in combination with the nuclear label TOPRO3, to establish the outline of each cell and determine the proximity of the ribbon to the membrane. Label was observed in two distinct locations: at the base of the OHC immediately below the nucleus as well as between the nucleus and the cuticular plate in wild-type ears (Figure 28). The subnuclear label tended to be on the side of the OHC facing the stria vascularis, consistent with the location of type II afferent synapses (Liberman, 1980) and likely reflects the position of synaptic ribbons. Hence, we consider all label observed below the midline of the nucleus as functional ribbons.

One or two ribbons were observed at the base of each OHC in wild-type (Figure 29A). Although ribbon number in OHCs has not been assessed in mouse using EM, studies from cat suggest that ribbons are extremely rare in mature OHCs above the 1 kHz place (Liberman et al., 1990). In the extreme apex, a maximum of one to two ribbons per OHC were observed. The discrepancy between our immunohistochemistry in mouse and the EM data in cat may reflect cross-species differences or be due to an underestimate of ribbon number in the EM study, a possibility acknowledged by the author due to the small size of ribbons in OHCs (sometimes appearing on only a single section) and the sparse sampling technique (analyzing only every fifth section) used. Ribbon number was reduced to 0.1 per OHC in mutants.

Although there's no report of ribbons located elsewhere in OHCs, the supranuclear label may reflect nascent or vestigial ribbons or even cross-reaction with a protein with high homology to the CtBP2 family such as the Golgi-associated brefeldin A-ADP-ribosylated substrate (Spanfo et al., 1999). Interestingly, the shape, number and distribution of the supranuclear label was identical between mutant and wild-type (Figure 29B).

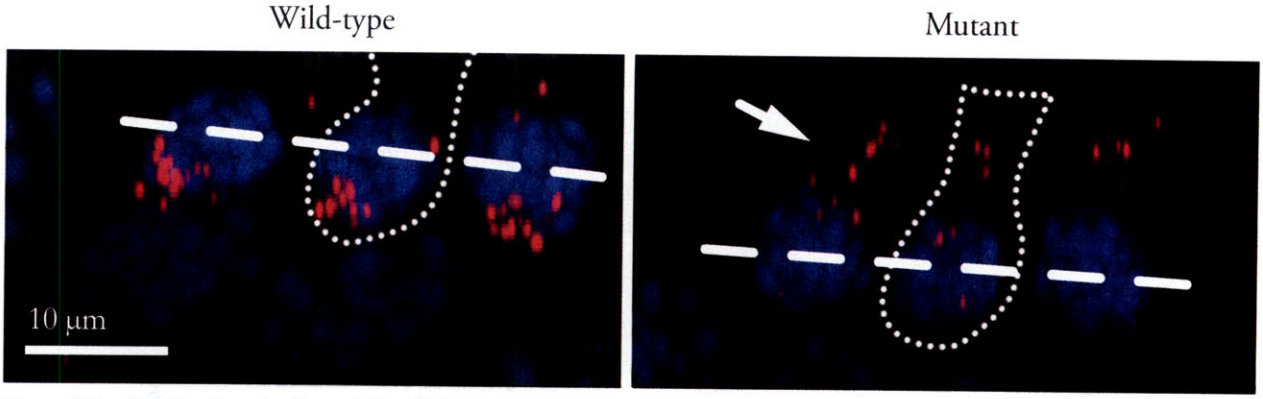

Figure 28 – Confocal projection of the 22 kHz region of whole-mount cochleae stained with the ribbon marker, CtBP2 (red), and a nuclear marker, TOPRO-3 (blue). Only the YZ plane is shown. Modiolar side is to the right. CtBP2 also appeared to label some supranuclear structure as well (grey arrow). Dotted line indicates outline of the second row of OHCs. All CtBP2-positive spots below the dashed line were considered synaptic ribbons. The arrow indicates CtBP2-positive spots above the dashed line (termed "supranuclear label" which were not considered synaptic ribbons.

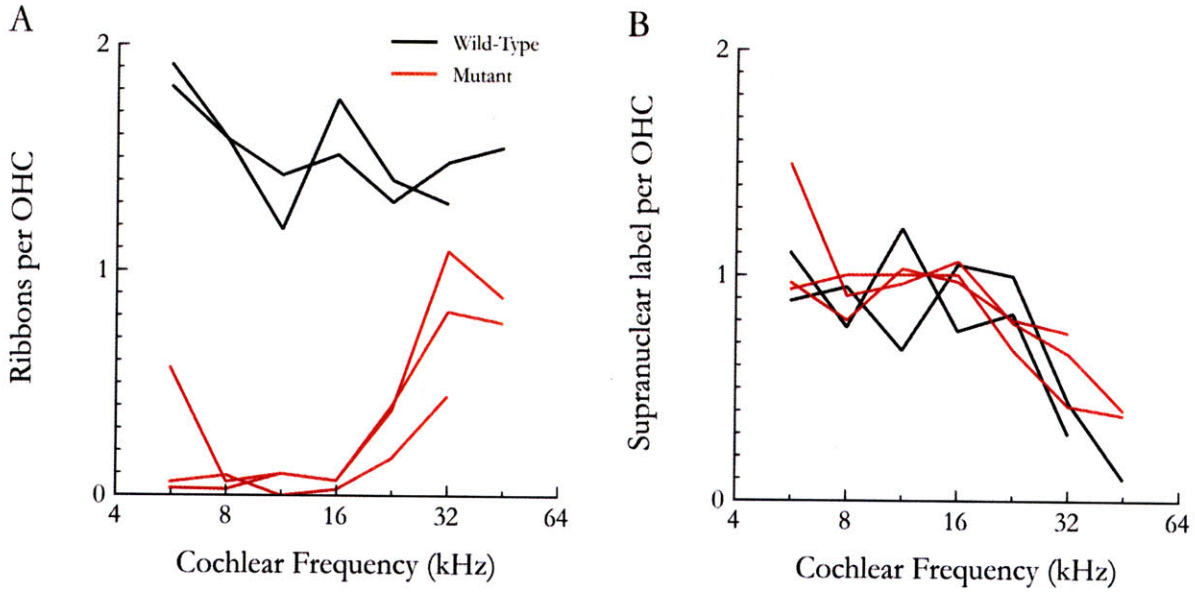

Figure 29 – A: Number of ribbons per OHC. Ribbon number was estimated from confocal analysis of whole-mount cochlear preparations (Figure 28). Only ribbons appearing below the midline (indicated by the dashed line in Figure 28) were counted. B: Supra-nuclear label, as assessed by all CtBP2-positive spots above the midline of the nucleus.

7.2 Cochlear physiology

Although the source of the nonlinearity that produces DPOAEs is unclear, the reverse transduction process mediated by OHCs contributes to the amplification of DPOAEs (Liberman et al., 1997). Hence, DPOAEs are a sensitive metric of OHC function and perturbations in OHC function will likely be reflected in DPOAE responses (Lonsbury-Martin and Martin, 1990). Despite the ten-fold reduction in ribbon number in OHCs of bassoon mutants, the growth of $2f_1$-f_2 DPOAE amplitude with level was normal and DPOAE thresholds were identical to wild-type (Figure 4A, Figure 30A). However, the phase of the DPOAE changed much more rapidly with level between approximately 35, where the DPOAE first becomes visible above the noise floor,

and 60 dB SPL. At f_2 levels above 60 dB SPL, the level at which DPOAE growth switches from compressive to linear, wild-type and mutant were in opposite phase (Figure 30B). Current models of DPOAE generation are insufficient to explain the significance of this phenotype; however, there is some speculation that loss of the ribbon may affect the putative local feedback network, particularly during the compressive growth of DPOAE amplitude. Further data on the role of the OHC-type II synapse in cochlear processing are needed to elucidate the significance of this phenotype.

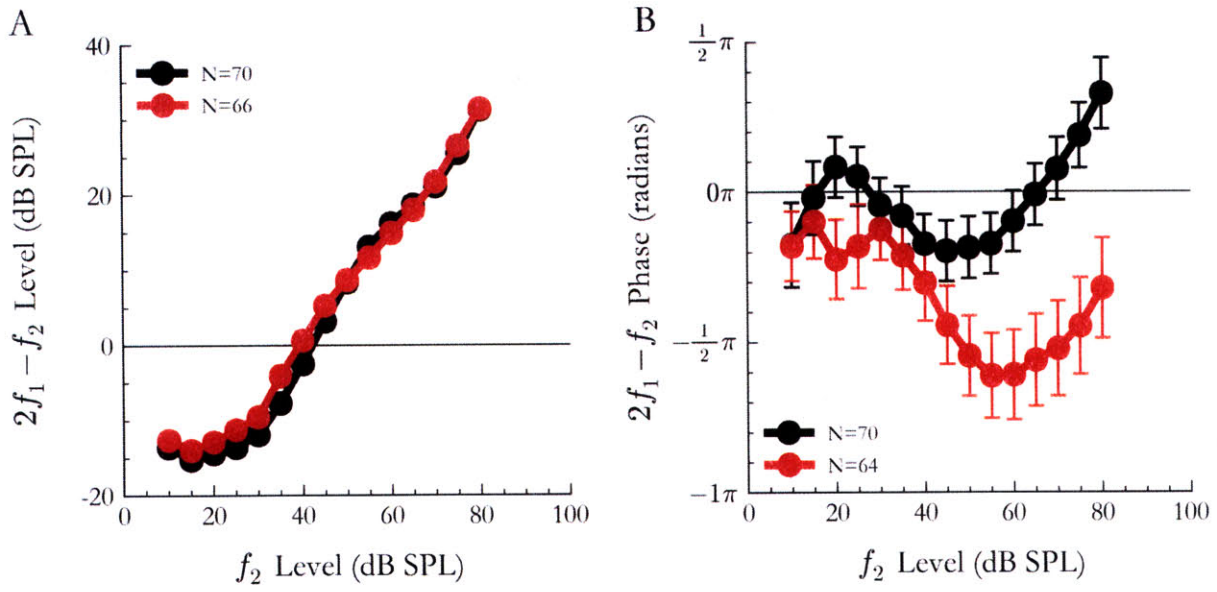

Figure 30 – $2f_2$-f_1 DPOAE amplitude (A) and phase (B) as a function of f_2 level for f_2 = 16 kHz. Error bars indicate ± SEM.

7.3 Olivocochlear innervation in Bassoon mutants

The LOC system primarily targets the dendrites of AN fibers and is hypothesized to have both excitatory and inhibitory roles, possibly through the actions of distinct neurotransmitters or cytochemical subgroups of the LOC. At least two cytochemical subgroups, a dopamanergic one and one co-localizing acetylcholine, GABA and CGRP, are present (Darrow et al., 2006b). Physiology experiments suggest that the GABA/CGRP/Ach subgroup is excitatory while the dopamanergic subgroup is a candidate for inhibitory effects. An early single-unit study of chronic cochlear de-efferentation in cat demonstrated a reduction in mean SR of 25 sp/s among high SR units (≥ 10 sp/s), (Liberman, 1990), although all other response properties of AN fibers, including maximum discharge rate, were normal. Consistent with this finding, application of CGRP, a putative neurotransmitter of the LOC system (Maison et al., 2003b) increases SR activity in afferents of the bullfrog lateral line (Bailey and Sewell, 2000). In a CGRP KO mouse, compound action potential (CAP) amplitude was decreased (Maison et al., 2003a).

In addition to these excitatory effects, inhibitory effects have also been attributed to the LOC based on indirect activation of LOC fibers via electrical shocks to the inferior colliculus (Groff and Liberman, 2003). Such inhibitory effects could conceivably protect AN fibers from glutamaterigic excitotoxicity as demonstrated by perfusion of dopamine through the cochlea during acoustic trauma which appeared to reduce CAP threshold shifts (d'Aldin et al., 1995).

Recently, a role for the LOC in balancing interaural sensitivity was proposed based on unilateral destruction of the LSO which appears to destroy correlated changes in ABR wave 1 amplitude between ears (Darrow et al., 2006a); however followup studies using unilateral cochlear trauma to reduce afferent drive in one side did not find the hypothesized decrease in contralateral response (Larsen, 2008), casting doubt on this hypothesis.

Despite our incomplete understanding of LOC effects, this evidence suggests that long-lasting changes in AN fiber excitability can be mediated by the LOC system. To investigate whether the reduction in SR observed in mutants might be due, in part, to changes in LOC innervation, two ears from each genotype were set aside for immunohistochemistry using vesicular acetylcholine transporter (VAT), a marker of the cholinergic terminals of the MOC and LOC, and tyrosine hydroxylase (TH), a dopaminergic marker. To minimize experimental variability the ears were processed in pairs, consisting of one from each genotype.

A remarkable elevation in the number of dopaminergic terminals was seen in both mutant ears compared with wild-type (Figure 31). In wild-type, dopaminergic terminals tended to be quite sparse, with fibers forming synapses with a small fraction of AN fibers, and large extents of the cochlea lack dopaminergic terminals. In contrast, dopaminergic terminals were observed throughout the cochlea in mutant fibers. Although the distribution and size of VAT label was similar between mutant and wild-type it was qualitatively weaker (fainter) in both the IHC and OHC region of mutant ears.

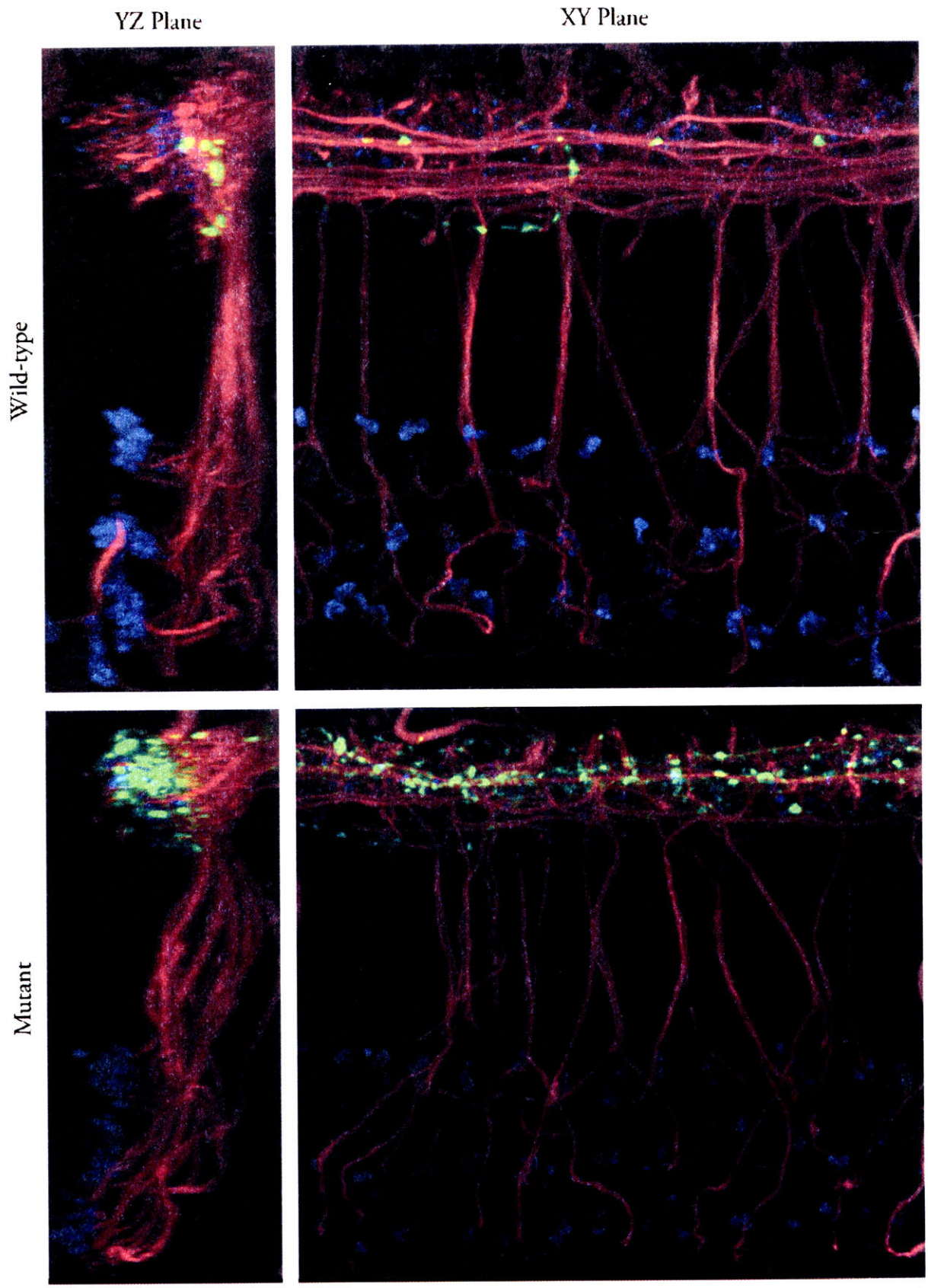

Figure 31 – Confocal projections of cochlear whole-mounts stained with the dopamanergic marker, TH (green), the cholinergic marker, VAT (blue), and neurofilament (red) from the 16 kHz region of the cochlea.

The OC phenotype observed in mutants does raise some question about to what extent the reduced rates observed is due to loss of the synaptic ribbon. Although the reduction in spontaneous and sound-evoked discharge rate is consistent with an inhibitory role for the dopaminergic subgroup, a similar reduction in hair cell exocytosis is observed in isolated cochlear preparations and remains the most likely explanation for the reduced rates observed in mutant ears (Khimich et al., 2005). In one study, chronic cochlear de-efferentation appears to affect only SR (Liberman, 1990), suggesting that the four-fold reduction in mean SR, compared with only a two-fold reduction in maximum discharge rate, may reflect a compound effect of both increased dopaminergic innervation and decreased synaptic drive.

The up-regulation of dopamanergic fibers in the bassoon mutants suggests that this mouse could be used as a model to test the hypothesis that these fibers are inhibitory. Several experiments come to mind:

- If the dopamanergic subgroup has a protective effect on AN fibers, then mutant ears should be less vulnerable to acoustic trauma. Vulnerability can be assessed via exposure to broadband noise of varying duration and monitoring elevation of DPOAE and ABR thresholds re baseline. Such experiments need to account for the reduced sound-evoked rates in bassoon mutants, which may lead to decreased activation of the efferent system. Decreased activation of the efferents, however, would be expected to lead to greater vulnerability: should we find that mutant ears are more robust, then this effect would most likely be attributed to the greater dopamanergic innervation.

- Unilateral de-efferentation in cat results in a reduction of mean SR among high SR units. Although the LOC appears to have excitatory and inhibitory effects, the excitatory component may be more dominant in cat. If there is indeed an up-regulation of an inhibitory component of the LOC in bassoon mutants, then chronic de-efferentation would likely result in a smaller reduction in SR, or even possibly an increase. Although it's unknown whether the ratio of excitation to inhibition is similar in mouse as well, this can be controlled for by comparing bassoon mutants with wild-type.

8 Appendix – Correlation between ribbon count and cochlear potentials

ABR thresholds in mutant ears were highly variable, with the best mutant ears having thresholds similar to wild-type. Although the majority of ribbons in mutant IHCs were positioned adjacent to the basolateral membrane, approximately 0.5/IHC in mid-turns was clearly floating in the cytoplasm far from the membrane itself. The remaining ribbons were within 1 μm of the membrane; however, 50% were positioned on the sides of the IHC that contact neighboring IHCs, a region that is unlikely to receive type I synapses. Despite this histological evidence that ribbons are largely nonfunctional in mutant IHCs, the large variability in ABR thresholds observed in mutants, with the best ears being similar to wild-type (Figure 32A) raised some concern that a large fraction of the ribbons touching the membrane may be functional ribbons.

To address concern that the residual ribbons in mutant IHCs might be contributing to this variability, ribbon counts from the cochleae set aside for histology were compared with physiological data collected immediately prior to perfusion of these ears. These ears were selected for perfusion since they were representative of the entire range of ABR thresholds and ABR wave 1 amplitudes observed in mutants. No correlation was observed between the number of ribbons per IHC and ABR threshold (not shown) or ABR wave 1 amplitude (Figure 32B), indicating that the remaining ribbons seen in mutant ears are non-functional.

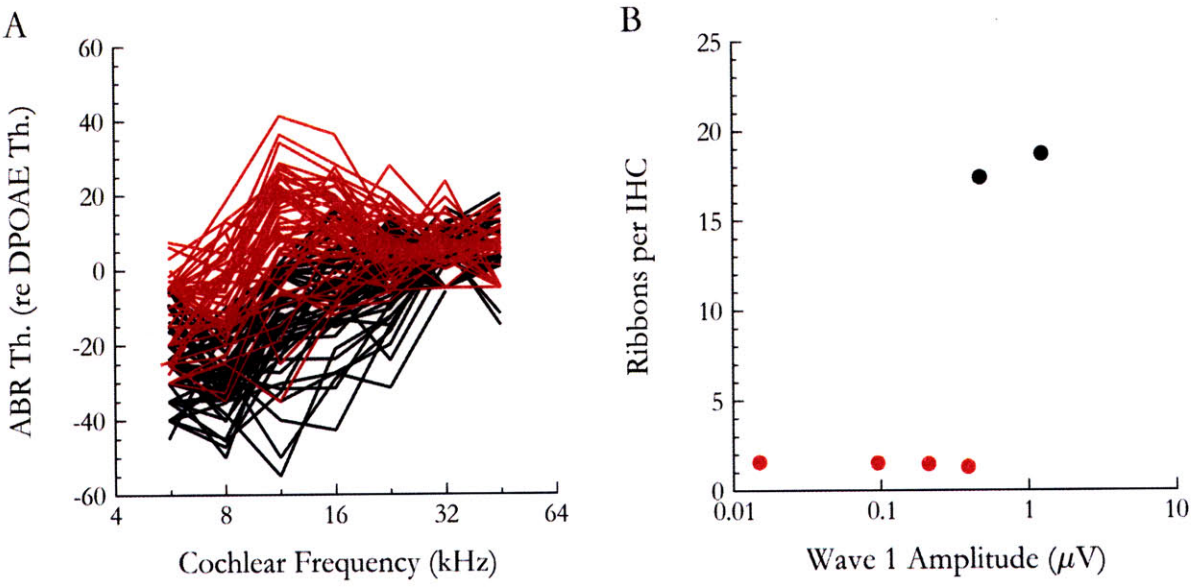

Figure 32 – There is a large variability in ABR waveform thresholds (re DPOAE thresholds), with some mutant ears appearing having wild-type like responses (A). However, no correlation is observed between wave 1 amplitude and ribbon number (B).

9 Appendix – Analysis of synchrony

9.1 Synchrony at high frequencies

Low-frequency pure tones are conventionally used to assess phase-locking; however, there is a decrease in synchrony of AN discharge as the stimulus frequency approaches 4 kHz due to the membrane capacitance of IHCs, which filter out high-frequency components of the receptor potential (Palmer and Russell, 1986). Initial experiments assessed phase-locking at 2 kHz, to the low-frequency tail of AN fibers; however, since mouse is a high-frequency hearing animal, we could assess phase-locking to low-frequency tones in only a small fraction of the AN fibers sample (Figure 33A). In the few ribbon-deficient units that phase-locking could be assessed in, synchrony appeared to be as good as wild-type (Figure 33B).

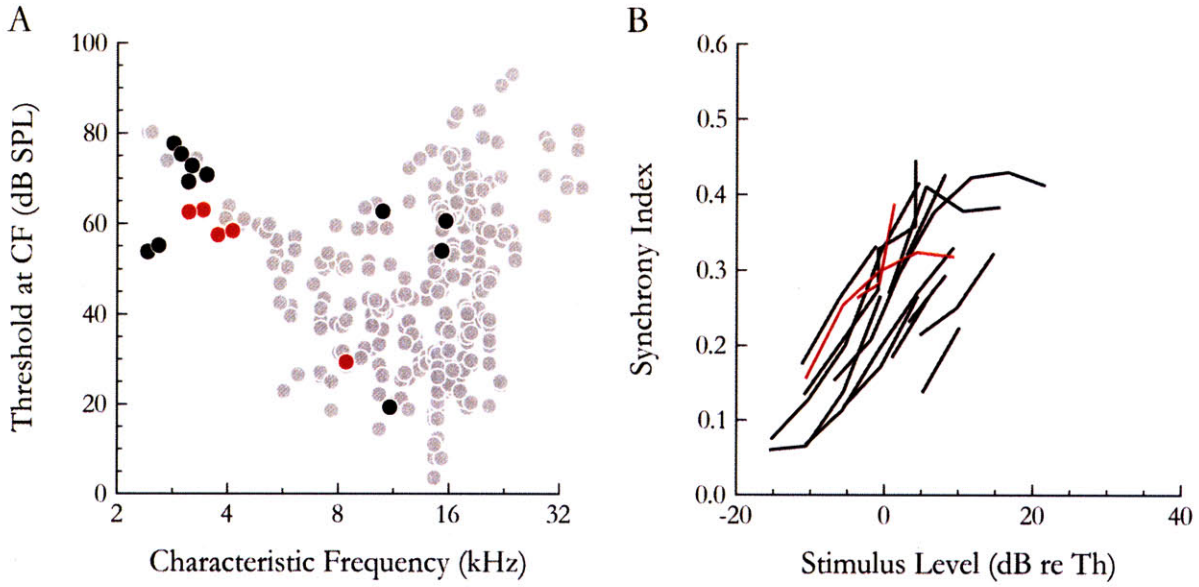

Figure 33 – A: Threshold at CF versus CF for the entire sample of AN fibers collected for this study (grey) highlighting the subset of fibers sufficiently sensitive at low-frequencies to assess phase-locking at 2 kHz (black – wild-type and red – mutant). B: Synchrony index versus level re threshold at 2 kHz. Synchrony index was assessed from phase-locking to a low-frequency 15 s 2 kHz tone assessed at multiple levels in 5 dB steps.

To assess synchrony in a larger proportion of the sample, we decided to use an on CF carrier amplitude-modulated by a low-frequency waveform. Two approaches for amplitude-modulated were considered: sinusoidally amplitude modulated (SAM) tones and transposed tones (Figure 34). SAM tones, in which a high-frequency carrier is amplitude-modulated by a low-frequency sinusoid, are prevalent throughout the literature (for review, see Joris et al., 2004). In contrast, transposed tones are a relatively new paradigm, first developed by Bernstein and Trahiotis (2002) for use in psychophysical studies assessing localization using ITD cues encoded into the amplitude of high-frequency stimuli. When low-frequency tones are presented to the cochlea, they are effectively low-pass filtered and half-wave rectified by the IHC. By modulating a high-frequency carrier with a half-wave rectified low-frequency sinusoid, we can transpose the information present at low frequencies into the envelope of a high-frequency tone. The resulting temporal modulation IHC receptor potential is similar to the pattern produced by its response to a low-frequency sinusoid (Palmer and

Russell, 1986; Dreyer and Delgutte, 2006). In contrast, a half-wave rectified SAM tone is simply transformed into a sinusoidal modulation of the IHC receptor potential.

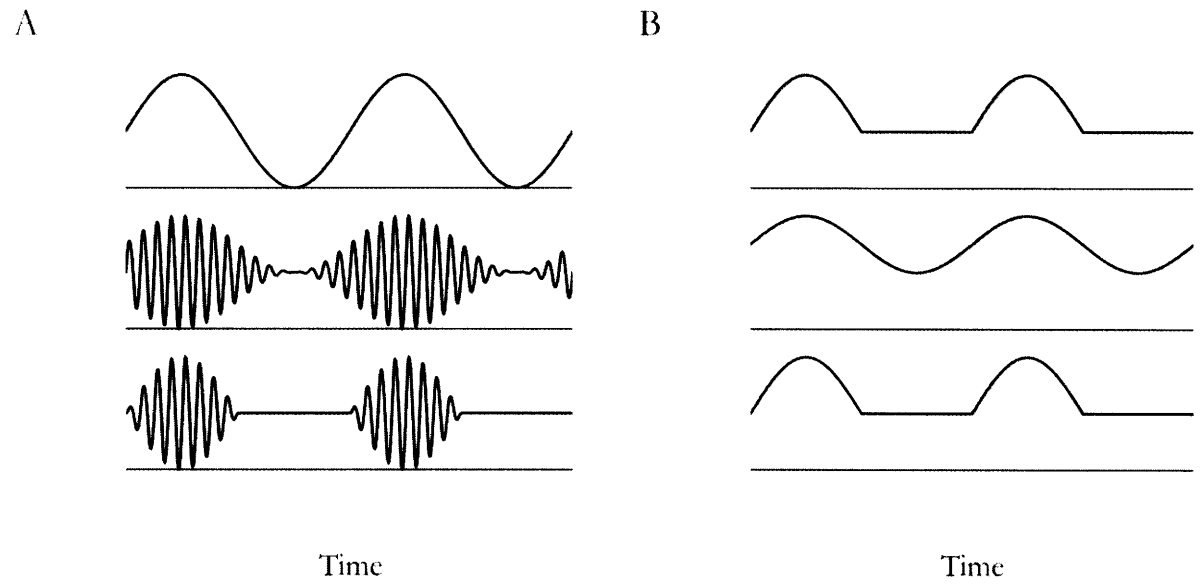

Figure 34 – Waveform (A) of stimuli conventionally used to assess phase-locking in the auditory nerve and the corresponding low-pass filtered, half-wave rectified waveform (B) that reflects the hypothetical receptor potential of an IHC. From top to bottom: 1 kHz pure tone, 16 kHz tone sinusoidally amplitude-modulated at 1 kHz, 16 kHz tone amplitude-modulated by a 1 kHz half-wave rectified sinusoid.

A study comparing phase-locking to the envelope of SAM and transposed tones in AN fibers of cat demonstrated better phase-locking for transposed tones across all stimulus levels and modulation frequencies (Dreyer and Delgutte, 2006); however, strength of phase-locking to amplitude-modulated stimuli drops off more rapidly with modulation frequency, rolling off around 1 kHz, while phase-locking to pure tones remains strong up to approximately 3 kHz. To assess whether such finding is applicable in mouse AN fibers, we compared SAM and transposed stimuli in a trial experiment with a few fibers. Both SAM and transposed tones showed similar growth of synchrony with increasing stimulus level for a number of modulation frequencies; however, phase-locking to transposed tones consistently reached a higher maximum synchrony than phase-locking to SAM tones (Figure 35, Figure 36). In response to a level series for several modulation frequencies ranging from 0.01 to 2 kHz, the maximum synchrony for each modulation frequency showed a similar roll-off at about 1 kHz regardless of whether transposed or SAM tones were used (Figure 36).

Although this data consists of only a few AN units, these findings confirm prior results that synchrony is better to transposed tones than SAM tones regardless of level or modulation frequency. Thus, transposed tones offer a more "efficient" approach to assessing fine spike timing in the mouse AN. The only compelling reason to choose SAM tones would be for comparison with the extensive literature that utilizes SAM tones, both in physiology and psychoacoustics (for review, see Joris et al., 2004). Indeed, certain experiments, such as assessing phase-locking in noise-damaged ears may benefit from using SAM tones for comparison with psychophysics studies in hearing-impaired listeners. However, our primary interest was to compare fine spike

timing in bassoon-deficient mice with wild-type, thus we chose to use the stimulus that gives better synchrony.

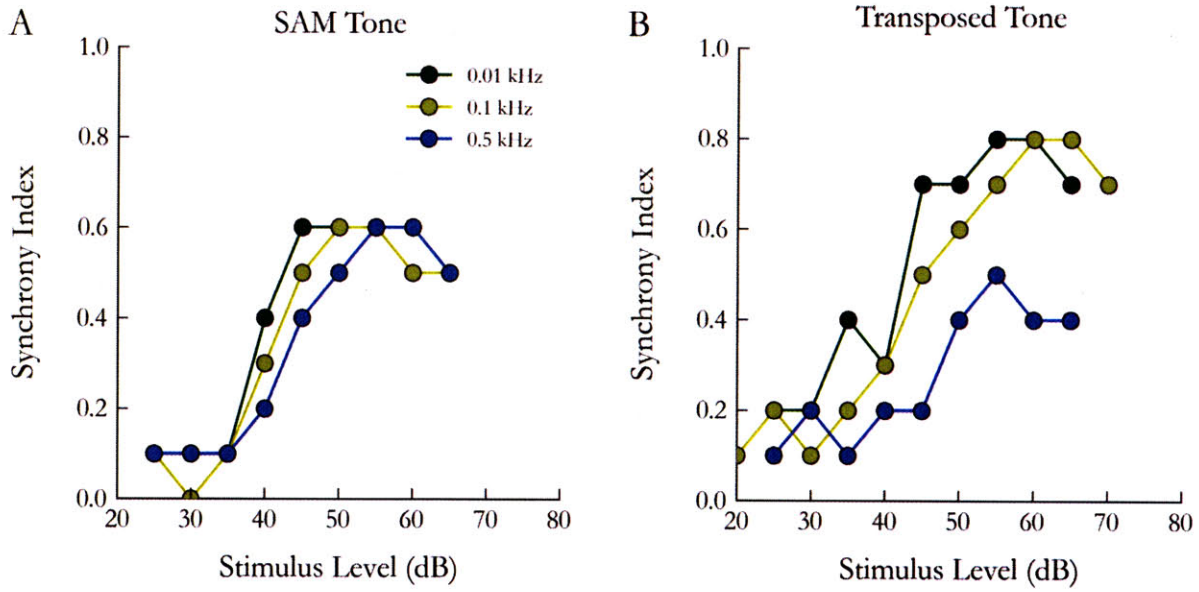

Figure 35 – Comparison of synchrony as a function of level for SAM tones (A) and transposed tones (B) in the same AN fiber.

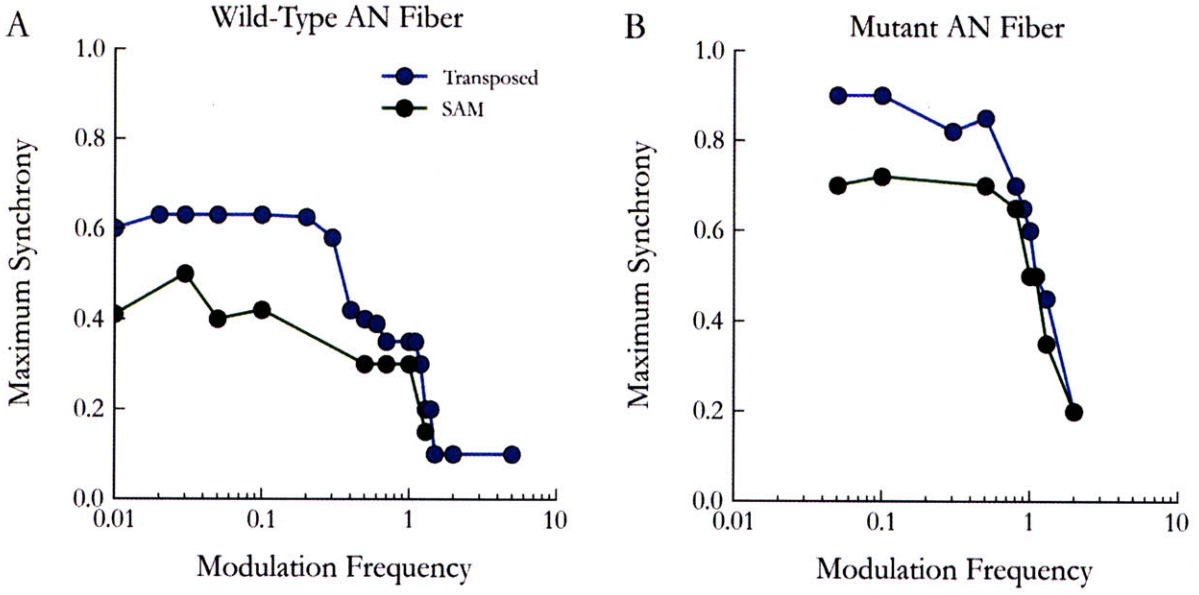

Figure 36 – Comparison of modulation transfer functions for SAM tones and transposed tones in a wild-type (A) and mutant (B) AN fiber. Modulation transfer functions are derived by the maximum SI observed in a level series for each modulation frequency tested.

9.2 Synchrony artifact in systems that trigger off the peak

Action potentials are traditionally viewed as a point process, or a series of identical, discrete events occurring throughout continuous time (Cox, 1962; Cox and Lewis, 1966; Perkel et al., 1967a, 1967b). Since extracellular recording of single neurons provide a voltage record of the waveform at the electrode, the challenge is to convert this continuous trace into a discrete series of event times that can be used for data analysis. Although there are a variety of complex spike detection algorithms such as template-matching (Wörgötter et al., 1986; Jansen and Ter Maat, 1992; Kim and McNames, 2007) and wavelet transforms (Hulata et al., 2002) that utilize both the time and frequency domain of the signal to identify event times, these were developed mainly for challenging preparations where there is significant background noise or activity from multiple units at a single recording site. In preparations where high-impedance electrodes can be used to isolate single neurons and reduce background noise, action potentials can easily be identified as large deviations in the voltage trace. Thus, a threshold value can be adjusted so that it is well above the fluctuations in voltage caused by noise, but sufficiently below the maximum deflection in voltage generated by an action potential that each action potential is reliably detected. The event time can be recorded as the time the signal crosses this set threshold (i.e. the "slope" method). An alternate approach is to define the event time at which the first derivative of the signal becomes zero after a threshold crossing. This approach essentially defines the event time as the time of the peak of the action potential (i.e. the "peak" method).

The custom-built event timer used for the single-unit recording in this thesis utilizes the peak method. This trigger was considered an improvement over the traditional Schmitt trigger, which utilizes the slope method, since a peak trigger presumably would result in "less timing uncertainty than the prevalent practice of triggering at some arbitrary point on the rising edge of the waveform" (Stefanov-Wagner, 1994). In a noise-free system where each AN fiber consistently generates an action potential of uniform amplitude, duration and shape, timing uncertainty would not be an issue regardless of the choice of trigger threshold or method. However, introducing periodic fluctuations into the signal from the electrode can have subtle influence on the shape of the action potential waveform. To illustrate the problem, note how an action potential riding on the rising portion of a sinusoidal artifact will advance the trigger time while a spike on the falling portion will delay the trigger (Figure 37). Both the slope and the peak of the action potential are shifted in time by a small fraction of a millisecond. Although small, such effects are of great concern in experiments that analyze synchrony of AN fibers to low-frequency tones. Such artifacts can arise if the electrode picks up electrical activity from the sound system or the cochlear microphonic and will introduce a jitter in the trigger time around the true time that can cause artifactual synchrony at sufficiently high levels.

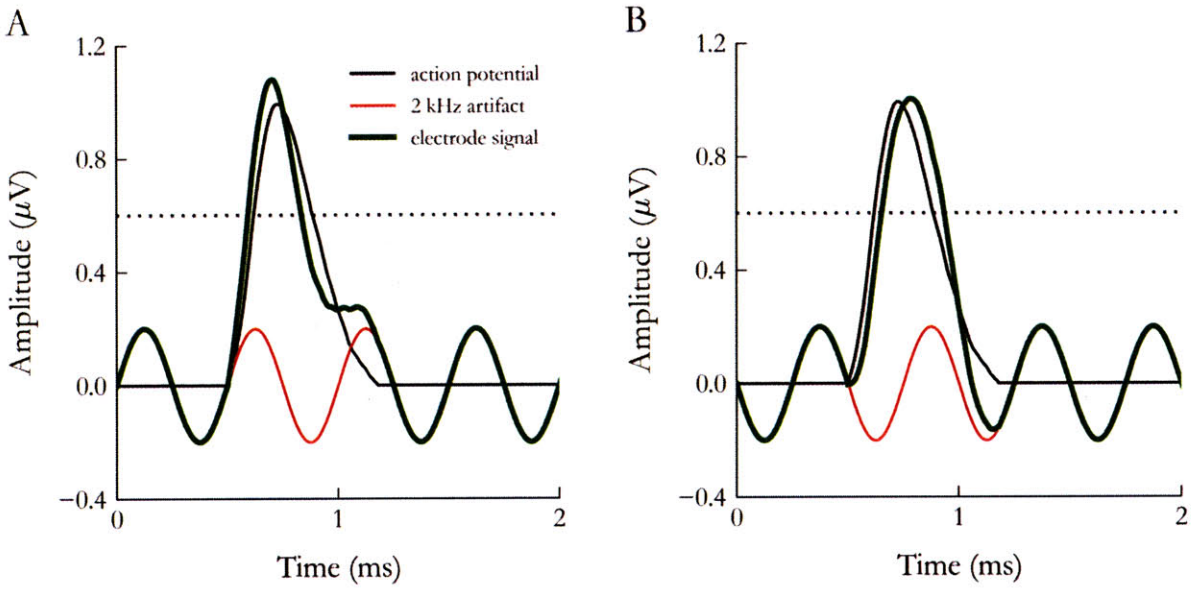

Figure 37 – Effect of a 2 kHz periodic artifact on the waveform of an action potential when the action potential occurs at 0 (A) or π phase (B) relative to the artifact. Dashed line indicates trigger threshold. The waveform of the action potential was obtained from a 15 s sample of the waveform from a single AN fiber recorded in vivo. The waveform was bandpass filtered from 0.3 to 3 kHz, digitized at 200 kHz and a single action potential was extracted from the digitized waveform.

The effect of such artifacts on measures of synchrony has been analyzed for the slope trigger method (Johnson, 1978). According to this analysis, the synchrony attributed to a sinusoidal artifact of frequency f can be estimated by

$$\mathrm{SI}_{\mathrm{artifact}} = \sqrt{8}\pi f \gamma t$$

where t is the rise time of the spike and γ is the ratio of the root mean square amplitude of the artifact to the amplitude of the spike. This equation is, however, valid only for systems that utilize a slope trigger since it rests on the key assumption that the slope of the spike (i.e. the first derivative of the waveform) relative to the amplitude of the interfering artifact[9] is the key determinant of jitter in the time of the trigger. However, if the trigger time depends on the slope of the signal going to zero, then the amplitude and the rise time of the spike are irrelevant. Instead, the key determinant of the artifact would be the curvature of the spike near its peak (i.e. its second derivative)[10].

[9] This is implicit in the equation since γt is proportional to the slope of the spike, thus increasing the amplitude of the spike or decreasing the rise time will decrease the synchrony artifact.

[10] An attempt to replicate the analysis done by Johnson (1978) by modeling the peak of a spike as a sinusoid failed since a closed form of the equation could not be found. However, by modeling the shape of the peak using a different equation, Johnson was able to find a closed form that describes the effect of an interfering signal on the synchrony artifact for a peak trigger (Johnson, personal communication).

To explore whether the method of triggering off the peak is, indeed, better than the simpler slope trigger, we generated a synthetic waveform of approximately 25 s in duration at a sampling frequency of 100 kHz. Five thousand interspike intervals were drawn from an exponential distribution with a rate parameter of 5 ms. All intervals smaller than 0.5 ms were discarded and the cumulative sum of the remaining (unsorted) intervals were computed to generate a series of event times. At each event time, a spike waveform obtained from an actual single unit recording (shown in Figure 37) was added to our synthetic waveform. Although we could have chosen a simpler model for our waveform, such as a cosine or a parabola, the slope and curvature of the actual spike are key elements that determine the effect of periodic artifacts on the trigger time. Hence, we decided to use an experimentally-measured waveform.

A sinusoidal interfering noise was added to the synthetic waveform, which was then run through two algorithms that imitate the slope and peak trigger, respectively. Specifically, one returned the time at which the signal crossed a pre-determined threshold and the other returned the time at which the first derivative crossed zero after crossing the pre-determined threshold. Since the frequency of the interfering artifact is typically the frequency to which phase-locking is being assessed (i.e. electrical artifact from the cochlear microphonic or acoustic system), we computed the synchronization index of the triggered times to the frequency of the artifact. As shown by our analysis, the method of triggering off the peak is not any better than triggering off the slope of the spike waveform, and can be significantly worse in some cases (Figure 38). Such a conclusion is not surprising when we consider that at frequencies of 2 to 4 kHz, the period of the artifact is 0.5 to 0.25 ms, which is close to the duration of an action potential. The steepness of the rising phase of the action potential helps minimize the influence of a periodic artifact on the threshold crossing. However, near the peak where the slope begins to shallow and become flat, the temporal structure of an interfering sinusoid whose period is shorter than the duration of the action potential will be visible in the curvature of the action potential and shift the triggered time, thus creating artifactual synchrony.

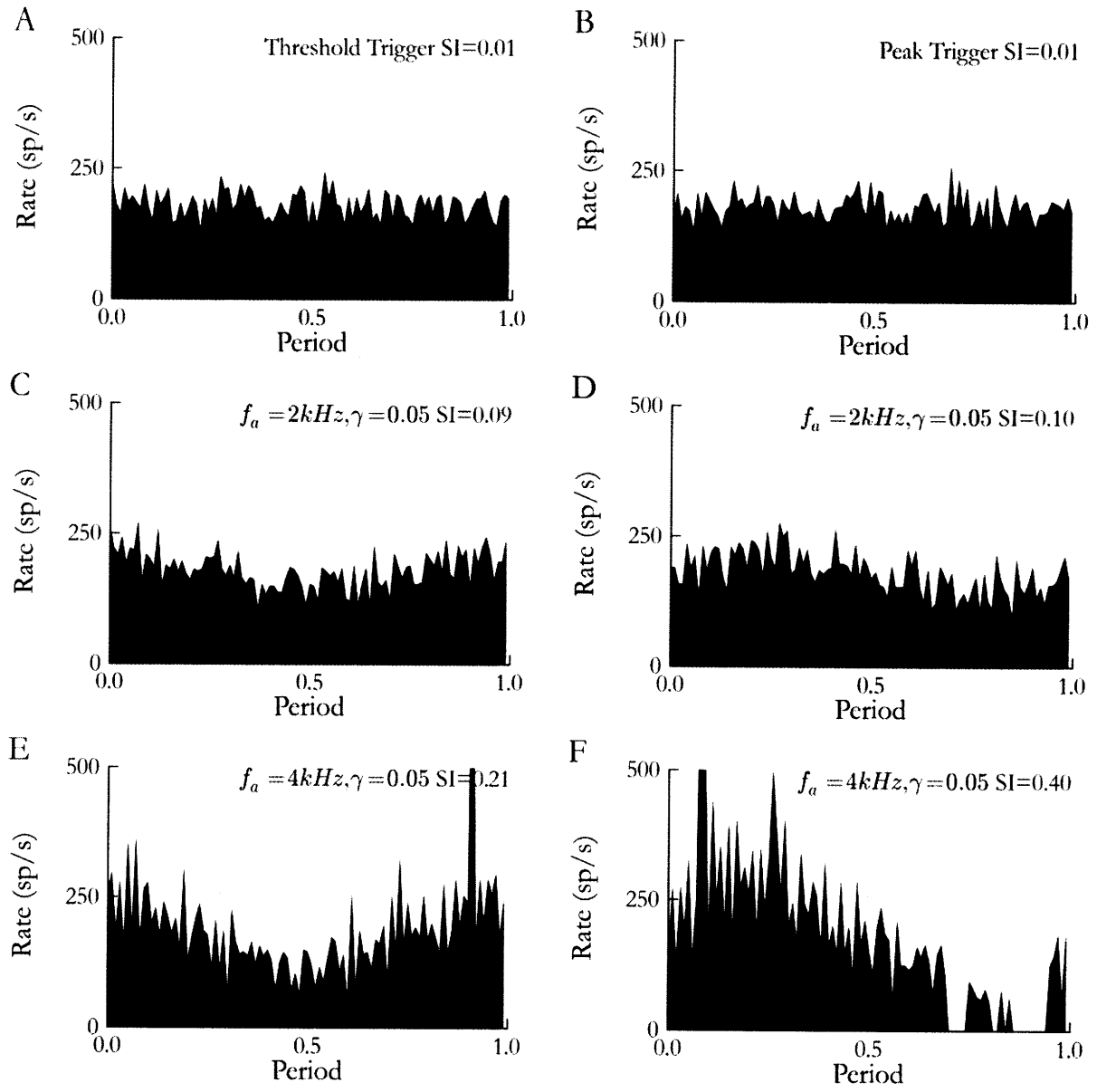

Figure 38 – Effect of a sinusoidal artifact on the observed event times of a spike train for an event timer that triggers off the threshold (A, C, E) or the peak (B, D, F) of a raw waveform. A, B: Distribution of trigger times when no artifact is present in the waveform (referenced to a 0.5 ms period). C, D: Trigger times when a sinusoidal artifact of 2 kHz and ratio of RMS amplitude to spike amplitude of 0.05 is added to the waveform. E, F: Same as C, D except the frequency of the artifact is 4 kHz.

It may be necessary to reconsider the use of a peak trigger in light of this analysis. The threshold trigger appears to be much more robust than the peak trigger; however, there are additional systems that may prove more accurate. For example, a dynamic "template" matching trigger can be trained at the beginning of each experiment to compute an "average" action potential (e.g. by computing the reverse correlation of the waveform given event times from a threshold trigger). Once the average waveform of the action potential is

computed, spike times can be determined by the time at which the correlation between this average waveform and the electrode waveform reaches a maximum.

9.3 Synchrony artifact for transposed stimuli

Is there reason to be concerned about artifactual synchrony to transposed tones? Probably not at the frequencies tested. Transposed tones have sidebands on either side of the carrier frequency at multiples of the modulation frequency (Figure 39). Phase-locking was assessed using a carrier frequency at CF, with the units showing the best phase-locking tending to have CF > 16 kHz[11]. Since the signal from the electrode is bandpass filtered from 0.3 to 3 kHz, frequency components present in a transposed tone with f_c = 16 kHz and f_m = 0 .5 kHz would be greatly attenuated. Our data showed strong phase-locking for high CF fibers for modulation frequencies as low as 120 Hz where there should be virtually no spectral energy from the transposed tone in the signal from the electrode.

However, as the modulation frequency increases and the carrier frequency decreases, the amount of energy that falls into the passband of the electrode filter will increase. This issue was recognized by Bernstein and Trahiotis (2002) who transform the half-wave rectified modulator into the frequency domain, filter out frequency components greater than 2 kHz by setting the magnitude to zero, then transform the signal back to the time domain. This approach restricts the extent of the sidebands to 2 kHz around the carrier frequency (Figure 40B). Although this distorts the waveform somewhat, the output of the peripheral processor still remains similar to that of a low-frequency sinusoid (Figure 40A) and should result in a similar extent of phase-locking; however, this remains to be assessed at the single-unit level.

[11] This is partially due to degraded tuning of the basilar membrane at high frequencies (Figure 4), which broadened cochlear filters and reduced distortion of the frequency components of transposed tones. Furthermore, there appears to be a lower-limit of phase-locking to amplitude modulated tones, possibly due to narrower bandwidths at low frequencies (Joris and Yin, 1992).

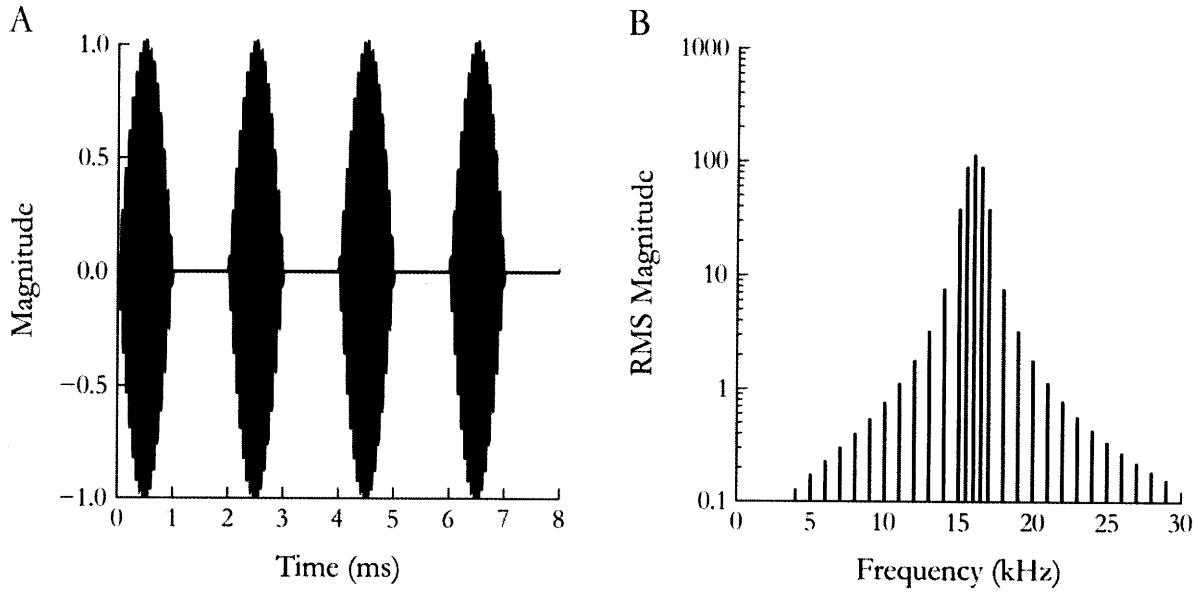

Figure 39 – Time (A) and frequency domain (B) of a transposed tone generated by multiplying a 16 kHz carrier frequency by a half-wave rectified 0.5 kHz sinusoid with 100% modulation.

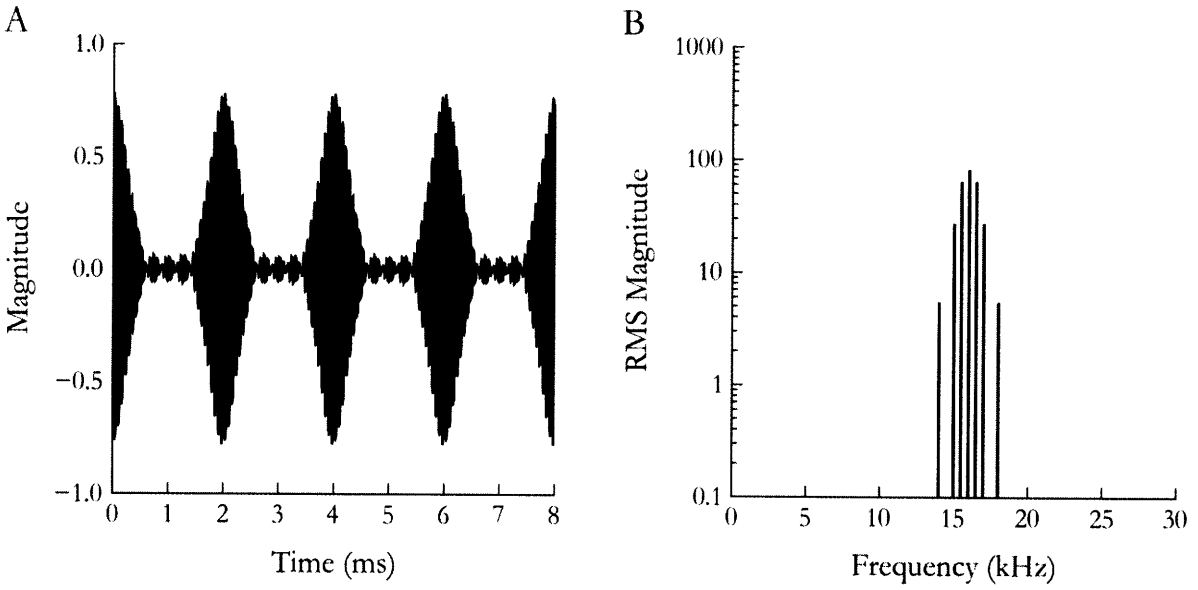

Figure 40 – Time (A) and frequency domain (B) of a transposed tone generated as in Figure 39 except the 0.5 kHz modulator was half wave rectified, transformed to the frequency domain, and the magnitude of spectral components greater than 2 kHz were set to zero. The resulting signal was transformed back to the time domain and multiplied with a carrier frequency of 16 kHz.

10 Appendix – Details on some spike train analysis

10.1 Estimating the refractory period from spike trains

AN spike trains are conventionally modelled as a Poisson process of given rate, $\lambda_E(t)$, modified by an absolute RP, t_D, during which no spike occurs followed by a relative RP where the probability of a spike increases exponentially with a given time constant, λ_R. Early studies that examine the refractory period generally fit the hazard (i.e. conditional intensity) function to their data (Li and Young, 1993). The hazard function describes the probability of a spike in a time interval, Δt, given that no spike has occurred up until that time. Although the literature is not clear on why the hazard function was preferred over the probability functions it is derived from, one advantage of the hazard function is its intuitive portrayal of the RP. Plots of this function clearly illustrate the dead-time of the absolute RP and exponential growth of the relative RP (Figure 41).

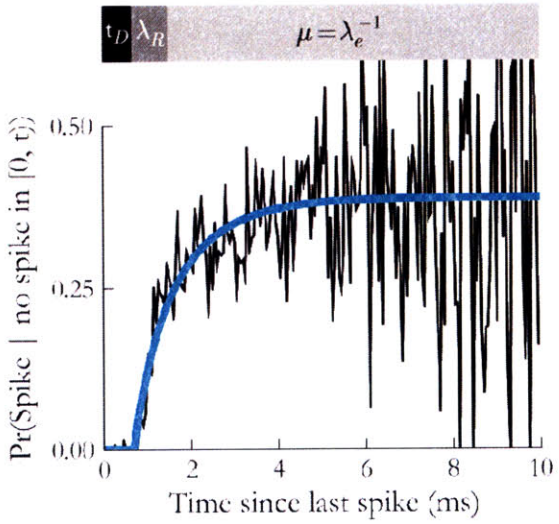

Figure 41 – Hazard function derived from the distribution of ISIs from a sample of spontaneous activity. The function reflects the probability of a spike at time t, given that no spike has occurred before then, and clearly illustrates the absolute RP and exponential time course of the relative RP as shown by the bar above the plot.

The hazard function can be defined as the ratio of the PDF, *PDF(t)*, to the survival function, *S(t)*. Thus, we can estimate the hazard function from the distribution of ISIs collected from a sample under conditions where the synaptic drive is held constant (e.g. spontaneous activity or the portion of the adapted response to tone bursts). As described by Li and Young (1993), an ISI histogram, *I(n)* of binwidth Δt is first computed and the hazard function, *h(n)* can be computed:

$$h(n) = \frac{PDF(n)}{S(n)} = \frac{I(n)}{\Delta t \sum_{n=t}^{N} I(n)}$$

where the sequence of n represents the values of the distribution at discrete intervals: ISI = $n\Delta t$. Parameters can then be extracted from the resulting estimate of the hazard function by finding the duration over which the probability of a spike is consistently zero, which gives us t_D, and the value of the asymptote, equivalent to

λ_E^{-1}, by averaging the later time bins. The final parameter, λ_R, can be computed by estimating the time at which the hazard function reaches 0.63 (specifically, $1\text{-}e^{-1}$) of its asymptote.

Even for long samples of spiking activity (the plot in Figure 41 represents a 150 s sample from a 130 sp/s fiber), the function becomes extremely noisy at long intervals due to quantitization of the ISIs into discrete time bins and rare occurance of long ISIs. The noisiness of the function becomes particularly problematic when analyzing mutant data due to the reduced number of spikes available for analysis. While this problem can be partially rectified by approaches such smoothing the data or fitting a curve only to the first 10 ms of the hazard function, an alternate approach is to fit to the cumulative distribution function (CDF) of the ISI distribution instead (Figure 42). Since the hazard function is derived from the CDF, this approach is simply a way of estimating the model parameters using a different equation. The CDF is relatively simple to compute from the ISI sample by sorting the ISIs, with the cumulative probability for the i^{th} ISI defined as i/n where n is the total number of ISIs in the sample. Using the same model described above, the CDF is given by

$$CDF_{isi}(t) = \left(1 - e^{-\lambda_E(t-t_D)}\right)\left(1 - e^{-\lambda_R(t-t_D)}\right) \quad for\ t \geq t_D$$
$$CDF_{isi}(t) = 0 \quad for\ t < t_D$$

$$CDF_{isi}(t) = 1 - \lambda_E e^{-\lambda_R(t-t_D)} - \lambda_R e^{-\lambda_E(t-t_D)} \quad for\ t \geq t_D$$
$$CDF_{isi}(t) = 0 \quad for\ t < t_D$$

The curve can then be fit by minimizing the sum of the squared x and y residuals. To ensure that long ISIs do not dominate the goodness of fit, we can weight the x residuals by the inverse of the CDF. This weighting is essentially a similar concept as truncating the hazard function to the first 10 ms, except we do not have to define an arbitrary cutoff.

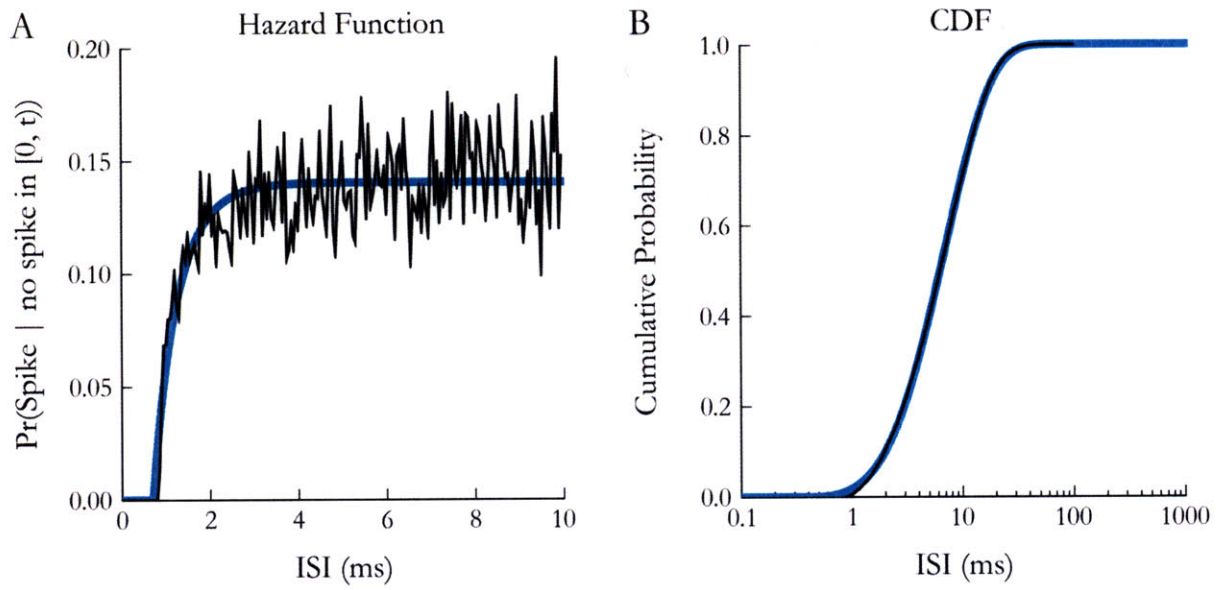

Figure 42 – Fitting to the hazard function (A) versus the CDF (B). Black line indicates the raw estimate of the function as derived from ISIs obtained from a 150 s sample of spontaneous activity. Thick blue line indicates model fit to the raw data.

10.2 Sparse counting technique for spike trains

A naive approach to computing spike counts using a sliding window over long sample times is often computationally intensive. Generating counts for spike trains of up to 150 s using a window slid in 1 μs increments across the spike train requires 150 million iterations. This algorithm reduces the number of iterations necessary by several orders of a magnitude: the maximum number of iterations needed will never be more than twice the number of spikes in the train (and often will be far less depending on the window size and spike rate). Although originally written to optimize computation of the Fano factor for large datasets, this algorithm is useful for a number of other analysis techniques as well. For example, if one was to assume that a given spike train is generated via a Poisson process, then the counts generated by this algorithm can be used to compute the probability that a given spike in the train could be drawn from a Poisson distribution with a given rate parameter.

The following code is written in C++ syntax specifically for the Python weave package, which facilitates inlining of C++ code and utilizes the Python and Numpy C-interface to manipulate the Python data structure that stores the spike time information. We provide this code as a template to give an idea of the structure needed for sparse counting. It is a relatively straightforward process for someone skilled in writing C-interfaces for other languages (e.g. Matlab, LabVIEW) to modify the code accordingly. The result array is pre-allocated and resized if necessary (i.e. via PyArray_Resize). Note that Nsp and Ncount are vectors holding the dimensions of sp and count, respectively. SP1(i) and COUNT2(i,j) are C++ templates that access the elements stored in the sp and count arrays at the given indices (sp and count are actually Numpy data structures holding an array plus associated information, hence it is simpler to use the provided templates to access the data inside the arrays).

Additional steps that can be taken to optimize the code if additional speed is needed, such as converting all time units to integers and computing the mean and standard deviation simultaneously so additional loops over the result array are not needed; however, such steps were not needed for the analysis done in this thesis.

```
/*  Note that the function can take any arbitrary unit of time, but the unit
 *  must be uniform across the parameters passed to the function (e.g. if you
 *  provide spike times in ms, the count interval must be specified in ms as
 *  well).
 *
 *  Input parameters:
 *     1. ci                Length of the window over which to compute the spike
 *                          count.
 *     2. sp                Sparse array containing the time of each spike.
 *     3. duration          Duration of the sample.
 *
 *  RETURN: 2D array with 4 columns:
 *     1. spike count       Number of spikes in the counting window.
 *     2. window fraction   Length of interval (in same units as the input data)
 *                          that the spike count is valid for.  For example, if
 *                          the input data is in microseconds, then a value of
 *                          413 would indicate that if you slide the window in 1
 *                          microsecond increments along the spike train, the
 *                          spike count in column 1 is valid for 413 of these
 *                          "increments".
```

```
 *     3. spike            Boolean flag indicating whether or not the leading
 *                         edge of the window is on a spike.  Note that the
 *                         counting algorithm does not include this spike in
 *                         the count for that current row since the upper bound
 *                         is exclusive.  The count is for the interval [lb,
 *                         ub) where lb is the lower bound of the window and ub
 *                         is the upper bound.
 *     4. time             Position of the leading edge of the counting window.
 **/

/* lb and ub track the first and last spike that fall within the counting
 * window, ci, respectively.  spikes keeps track of the current spike count
 * within the window and is incremented each time ub is incremented,
 * decremented each time lb is incremented.
 **/
int spikes=0, ub=0, lb=0, i=0;
float lb_time=0, ub_time=ci, n_time=0, lb_isi=0, ub_isi=0, c_time=0;

/* Counting begins at t=ci.  We find the first spike that occurs after ci and
 * weight the number of spikes up to this point by the time range between ci
 * and the start of this spike.  There are several edge cases to consider:
 *      1.  No spikes occur before ci.
 *      2.  All spikes occur before ci.
 **/
for (; (SP1(ub)<=ci) && (ub<Nsp[0]); spikes++, ub++);

/* Now that we have found the first spike, we loop through the entire spike
 * array.  Note that the first window is also processed in this loop as well.
 **/
for (; ub<=Nsp[0]; spikes++, ub++) {
    /* If we are on the last spike, then isi is computed up to the end of the
     * stimulus duration.  isi cannot be greater than ci.  **/
    n_time = (ub==Nsp[0]) ? duration : SP1(ub);
    ub_isi = n_time-ub_time;

    /* If the distance of the next spike at the lower bound of the window is
     * less than the distance of the next spike at the upper bound of the
     * window, then we need to iterate through the spikes at the lower bound
     * and add count and weighting factors accordingly.
     **/
    lb_time = ub_time-ci;
    c_time = 0;
    for (; (ub!=lb) && ((lb_isi=SP1(lb)-lb_time) < ub_isi); lb++, spikes--) {
        if (lb_isi > 0) {
            COUNT2(i,0) = spikes;
            COUNT2(i,1) = lb_isi-c_time;
            COUNT2(i,2) = 0;
            c_time += COUNT2(i,1);
            COUNT2(i,3) = ub_time+c_time;
            i++;
        }
```

```
        if (i+2 >= Ncount[0]) {
            PyArray_Dims dims;
            dims.len = 2;
            dims.ptr= Ncount;
            dims.ptr[0] += Nsp[0] + 10;
            PyArray_Resize(count_array, &dims, 1, NPY_ANYORDER);
        }
    }

    COUNT2(i,0) = spikes;
    COUNT2(i,1) = ub_isi-c_time;
    if (ub==Nsp[0]) {
        COUNT2(i,2) = 0;
    } else {
        COUNT2(i,2) = 1;
        ub_time = SP1(ub);
    }
    COUNT2(i,3) = n_time;
    i++;
}
if (i>=Ncount[0]) {
    return_val = -1;
} else {
    return_val = i;
}
```

The mean and variance of the spike count for the sample can be computed from the resulting array by using the window fraction (column 2), w_f, to weight the counts (column 1), c. Where d is total sample duration of the spike train and w is the counting window, the weighted mean can be computed accordingly

$$\bar{c} = \frac{\sum_{i=1}^{n} c_i w_{f_i}}{d - w}$$

The weighted variance is given by

$$\sigma_{\bar{c}}^2 = \frac{\sum_{i=1}^{n} w_{f_i} \left(sp_{num_i} - \overline{sp_{num}}\right)^2}{d - w}$$

Note

$$\sum_{i=1}^{n} w_{f_i} = d - w$$

since the spike count is undefined for the initial portion of the spike train of length w as we have no information about the prior spiking history before this point.

11 Acknowledgements

During my time as a graduate student in Boston I have had the pleasure of meeting many people who have shaped me, both professionally and personally. I am deeply grateful to these individuals for the support they have given me over the years:

Dr. M. Charles Liberman, my thesis advisor, has helped me develop as a scientist and inspired me to continue my work in auditory physiology. He was always available whenever I needed assistance with a technique or analyzing my data. He allowed me great freedom to explore a variety of research topics and encouraged me to develop a strong set of skills ranging from molecular biology to computer programming to complement my physiology work; yet, he always kept me focused on the big picture and kept me from getting distracted by minute details.

The expertise and knowledge of my thesis committee – Dr. John Guinan, Dr. William Sewell and Dr. Doug Vetter – was invaluable. In addition to being on my thesis committee, they also formed my oral qualifying committee along with Dr. Chris Brown. I had many enjoyable discussions with them about my research and their feedback helped hone my research and critical thinking skills. My academic advisors, Dr. Jennifer Melcher and Dr. Andrew Oxenham, ensured I was on track and making timely progress towards the completion of my thesis. My undergraduate research advisors, Dr. Doris K. Wu and Dr. Arthur N. Popper, provided me with career advice and encouragement as I began to look for a postdoctoral position.

Dr. Tobias Moser, who provided the transgenic mice used in this study, was involved in the design and planning of some of the experiments detailed in this thesis. The in vitro work from his lab was helpful in crafting the appropriate paradigms for the single fiber recordings. His student, Nicola Strenzke, spent a year at Eaton-Peabody to learn how to do single fiber recordings from me: she assisted with collection of some of the data presented in this thesis.

My labmates – Meritxell Argence, Keith Darrow, Adam Furman, Ann Hickox, Erik Larsen, Harrison Lin, and Stephane Maison – kept me engaged with lively discussion about research over countless pots of coffee and often helped me get over stumbling blocks in my experiments. The engineers – Chris Scarpino, Ishmael Stefanov-Wagner and Frank Cardarelli – maintained the equipment used in the single fiber experiments. Anytime there was a hardware malfunction or bug in the software they were extremely quick to respond, even in the earliest hours of the morning when everyone else was asleep. Connie Miller ensured that the surgery room and histology lab were always stocked with supplies and kept the area clean and well-organized. Leslie Dodds, whose steady hands and patience results in some of the most beautiful whole-mount cochlear immunohistochemistry, taught me the secrets to her technique. Ken Hancock, Adrian KC Lee, Daryush Mehta and Bo Wen always took the time to help me whenever I was confounded by arcane engineering terminology. Dianna Sands and Jessica Cunha worked tirelessly to handle the paperwork necessary to keep a lab running smoothly and were quick to respond whenever I had an administrative concern. Albert Edge let me use his lab resources for genotyping and some exploratory molecular biology work. His door was always open whenever I was having difficulty troubleshooting a new protocol.

A few years ago, I sat down with several SHBT students for dinner after a long day of skiing. Out of this dinner came the idea to initiate a recruiting campaign to increase awareness of the SHBT program. Although

many SHBT students and faculty assisted, the success of the SHBT Recruiting Committee would not have been possible without a core group of individuals: our supervisors Dr. Chris Brown and Dr. Bertrand Delgutte as well as SHBT students Erik Larsen, Nick Malyska and Cara Stepp. These people had key roles in initiating our recruiting efforts and invested extensive time into making the committee a success.

I would have been lost without the cued language transliterators who covered my courses, lab meetings and research seminars. One transliterator, Thomas Shull, has worked with me during my entire time at MIT as a graduate student. He was always eager for a challenge and enjoyed tackling some of the hardest assignments I threw at him. One particularly difficult assignment was transliterating for 6.541J: Speech Communication, a course that reviews detailed aspects of speech sounds. Through extra work on Tom's part, we were able to develop a series of additional signals that could be used to disambiguate the sounds discussed in the course.

I could always count on my friends at Eaton Peabody and MIT whenever I needed to relax after a long day in the lab or get out of Boston for a few days: we enjoyed numerous oysters by the waterfront, backpacking trips through the valleys, skiing in the mountains and cabin retreats. At work, my labmates as well as other coworkers – especially Naomi Bramhall, Eduardo Corrales, Dawn Keighley and Sudeep Mukerji – made long hours in the lab pass by quickly. The faculty and students of SHBT made me feel at home in Boston, especially my classmates Sasha Devore, Anne Dreyer, Adrian KC Lee, Daryush Mehta, Hui Nam, Anton Peng, S.R. Prakash, Yoko Saikachi, and Sherry Zhao as well as the HST administrative staff, especially Ms. Catherine Modica and Ms. Patricia Cunningham.

Last, but most important of all, I am grateful for the love and support of my parents and siblings – Brian, Kim and Brett – throughout the years.

12 List of References

Abraham WC (2008) Metaplasticity: tuning synapses and networks for plasticity. Nat Rev Neurosci 9:387

Adams JC (1979) Ascending projections to the inferior colliculus. J Comp Neurol 183:519-38

Altrock WD et al. (2003) Functional Inactivation of a Fraction of Excitatory Synapses in Mice Deficient for the Active Zone Protein Bassoon. Neuron 37:787-800

Angenstein F, Hilfert L, Zuschratter W, Altrock WD, Niessen HG, Gundelfinger ED (2008) Morphological and metabolic changes in the cortex of mice lacking the functional presynaptic active zone protein bassoon: a combined 1H-NMR spectroscopy and histochemical study. Cereb Cortex 18:890-7

Angenstein F, Niessen HG, Goldschmidt J, Lison H, Altrock WD, Gundelfinger ED, Scheich H (2007) Manganese-enhanced MRI reveals structural and functional changes in the cortex of Bassoon mutant mice. Cereb Cortex 17:28-36

Art JJ, Fettiplace R (1987) Variation of membrane properties in hair cells isolated from the turtle cochlea. J Physiol. 385:207–242

Augustine GJ, Santamaria F, Tanaka K (2003) Local Calcium Signaling in Neurons. Neuron 40:331-346

Bailey GP, Sewell WF (2000) Pharmacological characterization of the CGRP receptor in the lateral line organ of Xenopus laevis. J Assoc Res Otolaryngol 1:82-8

Batra R, Kuwada S, Fitzpatrick DC (1997) Sensitivity to Interaural Temporal Disparities of Low- and High-Frequency Neurons in the Superior Olivary Complex. I. Heterogeneity of Responses. J Neurophysiol 78:1222-1236

Bean BP (2007) The action potential in mammalian central neurons. Nat Rev Neurosci 8:451-465

Beck J, Ma WJ, Latham PE, Pouget A (2007) Probabilistic population codes and the exponential family of distributions. Prog Brain Res 165:509-19

Benevento LA, Coleman PD (1970) Responses of single cells in cat inferior colliculus to binaural click stimuli: Combinations of intensity levels, time differences and intensity differences. Brain Research 17:387-405

Bernstein LR, Trahiotis C (2002) Enhancing sensitivity to interaural delays at high frequencies by using "transposed stimuli". J Acoust Soc Am 112:1026-36

Berry MJ, Warland DK, Meister M (1997) The structure and precision of retinal spike trains. Proc Natl Acad Sci U S A 94

Beurg M, Safieddine S, Roux I, Bouleau Y, Petit C, Dulon D (2008) Calcium- and Otoferlin-Dependent Exocytosis by Immature Outer Hair Cells. J. Neurosci. 28:1798-1803

Beutner D, Voets T, Neher E, Moser T (2001) Calcium Dependence of Exocytosis and Endocytosis at the Cochlear Inner Hair Cell Afferent Synapse. Neuron 29:681-690

Blackburn CC, Sachs MB (1989) Classification of unit types in the anteroventral cochlear nucleus: PST histograms and regularity analysis. J Neurophysiol 62:1303-1329

Boehnke SE, Hall SE, Marquardt T (2002) Detection of static and dynamic changes in interaural correlation. J. Acoust. Soc. Am. 112:1617-1626

Brandstatter JH, Fletcher EL, Garner CC, Gundelfinger ED, Wassle H (1999) Differential expression of the presynaptic cytomatrix protein bassoon among ribbon synapses in the mammalian retina. European Journal of Neuroscience 11:3683-3693

Brandt A, Khimich D, Moser T (2005) Few CaV1.3 Channels Regulate the Exocytosis of a Synaptic Vesicle at the Hair Cell Ribbon Synapse. J. Neurosci. 25:11577-11585

Brownell WE, Bader CR, Bertrand D, de Ribaupierre Y (1985) Evoked mechanical responses of isolated cochlear outer hair cells. Science 227:194-6

Brunso-Bechtold JK, Thompson GC, Masterton RB (1981) HRP study of the organization of auditory afferents ascending to central nucleus of inferior colliculus in cat. J Comp Neurol 197:705-22

Buunen TJF, Rhode WS (1978) Response of fibers in the cat's auditory nerve to the cubic difference tone. J. Acoust. Soc. Am. 64:772-781

Caird D, Klinke R (1987) Processing of interaural time and intensity differences in the cat inferior colliculus. Exp Brain Res 68:379-92

Catterall WA (2000) Structure and regulation of voltage-gated Ca2+ channels. Annual Review of Cell & Developmental Biology 16:521

Chase SM, Young ED (2005) Limited Segregation of Different Types of Sound Localization Information among Classes of Units in the Inferior Colliculus. J. Neurosci. 25:7575-7585

Chevaleyre V, Takahashi KA, Castillo PE (2006) Endocannabinoid-mediated synaptic plasticity in the CNS. Annu. Rev. Neurosci 29:37-76

Corey DP, Hudspeth AJ (1979) Ionic basis of the receptor potential in a vertebrate hair cell. Nature 281:675-7

Cox DR (1962) Renewal process In Methuen's monographs in applied probability and statistics New York, NY: John Wiley & Sons, Inc.

Cox DR, Lewis PAW (1966) The statistical analysis of series of events In Methuen's monographs in applied probability and statistics New York, NY: John Wiley & Sons, Inc.

Cutting J, Rosner B (1974) Categories and boundaries in speech and music. Perceptual Psychophysics 16:564-570

d'Aldin C, Puel JL, Leducq R, Crambes O, Eybalin M, Pujol R (1995) Effects of a dopaminergic agonist in the guinea pig cochlea. Hear Res 90:202-11

Darrow KN, Maison SF, Liberman MC (2006a) Cochlear efferent feedback balances interaural sensitivity. Nature Neuroscience 9:1474-1476

Darrow KN, Simons EJ, Dodds LW, Liberman MC (2006b) Dopaminergic Innervation of the Mouse Inner Ear: Evidence for a Separate Cytochemical Group of Cochlear Efferent Fibers. J Comp Neurol. 498:403–414

Delgutte B (1996) Psychophysiological Models In Auditory Computation Springer Handbook of Auditory Research. New York: Springer-Verlag, p. 157-220.

Delgutte B (1980) Representation of speech-like sounds in the discharge patterns of auditory-nerve fibers. J. Acoust. Soc. Am. 68:843-857

Delgutte B, Joris PX, Litovsky RY, Yin TC (1999) Receptive Fields and Binaural Interactions for Virtual-Space Stimuli in the Cat Inferior Colliculus. J Neurophysiol 81:2833-2851

Devore S, Ihlefeld A, Hancock K, Shinn-Cunningham B, Delgutte B (2009) Accurate Sound Localization in Reverberant Environments Is Mediated by Robust Encoding of Spatial Cues in the Auditory Midbrain. Neuron 62:123-134

Dick O, tom Dieck S, Altrock WD, Ammermuller J, Weiler R, Garner CC, Gundelfinger ED, Brandstatter JH (2003) The Presynaptic Active Zone Protein Bassoon Is Essential for Photoreceptor Ribbon Synapse Formation in the Retina. Neuron 37:775-786

tom Dieck S, Altrock WD, Kessels MM, Qualmann B, Regus H, Brauner D, Fejtova A, Bracko O, Gundelfinger ED, Brandstatter JH (2005) Molecular dissection of the photoreceptor ribbon synapse: physical interaction of Bassoon and RIBEYE is essential for the assembly of the ribbon complex. J. Cell Biol. 168:825-836

tom Dieck S, Sanmarti-Vila L, Langnaese K, Richter K, Kindler S, Soyke A, Wex H, Smalla K, Kampf U, Franzer J, Stumm M, Garner CC, Gundelfinger ED (1998) Bassoon, a Novel Zinc-finger CAG/Glutamine-repeat Protein Selectively Localized at the Active Zone of Presynaptic Nerve Terminals. J. Cell Biol. 142:499-509

DiMatteo I, Genovese CR, Kass RE (2001) Bayesian curve fitting with free-knot splines. Biometrika 88:1055-1073

Dizon RM, Colburn HS (2006) The influence of spectral, temporal, and interaural stimulus variations on the precedence effect. J Acoust Soc Am 119:2947-64

Dreyer A, Delgutte B (2006) Phase Locking of Auditory-Nerve Fibers to the Envelopes of High-Frequency Sounds: Implications for Sound Localization. J Neurophysiol 96:2327-2341

Dunn RA, Morest DK (1975) Receptor synapses without synaptic ribbons in the cochlea of the cat. Proc Natl Acad Sci U S A. 72:3599–3603

Eisen MD, Spassova M, Parsons TD (2004) Large Releasable Pool of Synaptic Vesicles in Chick Cochlear Hair Cells. J Neurophysiol 91:2422-2428

Ekström P, Meissl H (2003) Evolution of photosensory pineal organs in new light: the fate of neuroendocrine photoreceptors. Philos Trans R Soc Lond B Biol Sci. 358:1679–1700

Elliott TM, Theunissen FE (2009) The Modulation Transfer Function for Speech Intelligibility. PLoS Comput Biol 5:e1000302

Evans EF (1972) The frequency response and other properties of single fibres in the guinea-pig cochlear nerve. J Physiol. 226:263–287

Eybalin M (1993) Neurotransmitters and neuromodulators of the mammalian cochlea. Physiol Rev 73:309-73

Feil R, Kleppisch T (2008) NO/cGMP-dependent modulation of synaptic transmission. Handb Exp Pharmacol:529-560

Fenster SD, Chung WJ, Zhai R, Cases-Langhoff C, Voss B, Garner AM, Kaempf U, Kindler S, Gundelfinger ED, Garner CC (2000) Piccolo, a Presynaptic Zinc Finger Protein Structurally Related to Bassoon. Neuron 25:203-214

Fettiplace R, Fuchs PA (1999) Mechanisms of hair cell tuning. Annu Rev Physiol 61:809-34

Francis HW, Rivas A, Lehar M, Ryugo DK (2004) Two types of afferent terminals innervate cochlear inner hair cells in C57BL/6J mice. Brain Research 1016:182-194

Furukawa T, Matsuura S (1978) Adaptive rundown of excitatory post-synaptic potentials at synapses between hair cells and eight nerve fibres in the goldfish. J Physiol. 276:193–209

von Gersdorff H, Matthews G (1994) Dynamics of synaptic vesicle fusion and membrane retrieval in synaptic terminals. Nature 367:735-9

von Gersdorff H (2001) Synaptic Ribbons:Versatile Signal Transducers. Neuron 29:7-10

von Gersdorff H, Vardi E, Matthews G, Sterling P (1996) Evidence That Vesicles on the Synaptic Ribbon of Retinal Bipolar Neurons Can Be Rapidly Released. Neuron 16:1221-1227

Glowatzki E, Fuchs PA (2002) Transmitter release at the hair cell ribbon synapse. Nat Neurosci 5:147-154

Godfrey DA, Kiang NYS, Norris BE (1975) Single unit activity in the posteroventral cochlear nucleus of the cat. The Journal of Comparative Neurology 162:247-268

Goldberg JM, Brown PB (1969) Response of binaural neurons of dog superior olivary complex to dichotic tonal stimuli: some physiological mechanisms of sound localization. J Neurophysiol 32:613-36

Goldstein J, Kiang NY (1958) Synchrony of Neural Activity in Electric Responses Evoked by Transient Acoustic Stimuli. J. Acoust. Soc. Am. 30:107-114

Goutman JD, Glowatzki E (2007) Time course and calcium dependence of transmitter release at a single ribbon synapse. Proc Natl Acad Sci U S A 104:16341-6

Grantham DW, Wightman FL (1978) Detectability of varying interaural temporal differences[sup a)]. J. Acoust. Soc. Am. 63:511-523

Green D, Swets J (1974) Signal detection theory and psychophysics. New York: Kreiger.

Groff JA, Liberman MC (2003) Modulation of Cochlear Afferent Response by the Lateral Olivocochlear System: Activation Via Electrical Stimulation of the Inferior Colliculus. J Neurophysiol 90:3178-3200

Guinan JJ (2006) Olivocochlear efferents: anatomy, physiology, function, and the measurement of efferent effects in humans. Ear Hear 27:589-607

Guinan JJ, Gifford ML (1988) Effects of electrical stimulation of efferent olivocochlear neurons on cat auditory-nerve fibers. II. Spontaneous rate. Hearing Research 33:115-127

Hafidi A, Beurg M, Dulon D (2005) Localization and developmental expression of BK channels in mammalian cochlear hair cells. Neuroscience 130:475-484

Harris DM, Dallos P (1979) Forward masking of auditory nerve fiber responses. J Neurophysiol 42:1083-1107

He L, Xue L, Xu J, McNeil BD, Bai L, Melicoff E, Adachi R, Wu L (2009) Compound vesicle fusion increases quantal size and potentiates synaptic transmission. Nature 459:93-97

Heidelberger R, Sterling P, Matthews G (2002) Roles of ATP in Depletion and Replenishment of the Releasable Pool of Synaptic Vesicles. J Neurophysiol 88:98-106

Heil P, Irvine DR (1997) First-Spike Timing of Auditory-Nerve Fibers and Comparison With Auditory Cortex. J Neurophysiol 78:2438-2454

Heil P, Neubauer H, Brown M, Irvine DR (2008) Towards a unifying basis of auditory thresholds: Distributions of the first-spike latencies of auditory-nerve fibers. Hearing Research 238:25-38

Heil P, Neubauer H, Irvine DRF, Brown M (2007) Spontaneous Activity of Auditory-Nerve Fibers: Insights into Stochastic Processes at Ribbon Synapses. J. Neurosci. 27:8457-8474

Heinz MG, Colburn HS, Carney LH (2001) Evaluating Auditory Performance Limits: I. One-Parameter Discrimination Using a Computational Model for the Auditory Nerve. Neural Computation 13:2273-2316

Henkel AW, Simpson LL, Ridge RM, Betz WJ (1996) Synaptic Vesicle Movements Monitored by Fluorescence Recovery after Photobleaching in Nerve Terminals Stained with FM1-43. J. Neurosci. 16:3960-3967

Hequembourg, Liberman (2001) Spiral Ligament Pathology: A Major Aspect of Age-Related Cochlear Degeneration in C57BL/6 Mice. JARO - Journal of the Association for Research in Otolaryngology 2:118-129

Holt JC, Xue J, Brichta AM, Goldberg JM (2006) Transmission Between Type II Hair Cells and Bouton Afferents in the Turtle Posterior Crista. J Neurophysiol 95:428-452

Holt M, Cooke A, Neef A, Lagnado L (2004) High Mobility of Vesicles Supports Continuous Exocytosis at a Ribbon Synapse. Current Biology 14:173-183

Houben D, Gourevitch G (1979) Auditory lateralization in monkeys: An examination of two cues serving directional hearing. J. Acoust. Soc. Am. 66:1057-1063

Hulata E, Segev R, Ben-Jacob E (2002) A method for spike sorting and detection based on wavelet packets and Shannon's mutual information. Journal of Neuroscience Methods 117:1-12

Hull C, Studholme K, Yazulla S, von Gersdorff H (2006) Diurnal Changes in Exocytosis and the Number of Synaptic Ribbons at Active Zones of an ON-Type Bipolar Cell Terminal. J Neurophysiol 96:2025-2033

Inagaki A, Ugawa S, Yamamura H, Murakami S, Shimada S (2008) The CaV3.1 T-type Ca2+channel contributes to voltage-dependent calcium currents in rat outer hair cells. Brain Research 1201:68-77

Irvine DRF (1992) Physiology of the auditory brainstem In D. Webster, A. N. Popper, & R. R. Fay, eds. The mammalian auditory pathway: Neuroanatomy New York, NY: Springer-Verlag.

Jansen RF, Ter Maat A (1992) Automatic wave form classification of extracellular multineuron recordings. Journal of Neuroscience Methods 41:123-132

Johnson DH (1978) The relationship of post-stimulus time and interval histograms to the timing characteristics of spike trains. Biophysical Journal 22

Johnson DH (1980) The relationship between spike rate and synchrony in responses of auditory-nerve fibers to single tones. J. Acoust. Soc. Am. 68:1115-1122

Johnson SL, Marcotti W (2008) Biophysical properties of CaV1.3 calcium channels in gerbil inner hair cells. J Physiol. 586:1029–1042

Joris PX, Carney LH, Smith PH, Yin TC (1994a) Enhancement of neural synchronization in the anteroventral cochlear nucleus. I. Responses to tones at the characteristic frequency. J Neurophysiol 71:1022-36

Joris PX, Smith PH, Yin TC (1994b) Enhancement of neural synchronization in the anteroventral cochlear nucleus. II. Responses in the tuning curve tail. J Neurophysiol 71:1037-51

Joris PX, Schreiner CE, Rees A (2004) Neural Processing of Amplitude-Modulated Sounds. Physiol. Rev. 84:541-577

Joris PX, Yin TCT (1992) Responses to amplitude-modulated tones in the auditory nerve of the cat. J. Acoust. Soc. Am. 91:215-232

Kalluri S, Delgutte B (2003a) Mathematical Models of Cochlear Nucleus Onset Neurons: II. Model with Dynamic Spike-Blocking State. Journal of computational neuroscience 14:91-110

Kalluri S, Delgutte B (2003b) Mathematical Models of Cochlear Nucleus Onset Neurons: I. Point Neuron with Many Weak Synaptic Inputs. Journal of computational neuroscience 14:71-90

Keen EC, Hudspeth AJ (2006) Transfer characteristics of the hair cell's afferent synapse. 103:5537-5542

Kemp DT, Brown AM (1984) Ear canal acoustic and round window electrical correlates of 2f1- f2 distortion generated in the cochlea. Hearing Research 13:39-46

Kennedy HJ, Meech RW (2002) Fast Ca2+ signals at mouse inner hair cell synapse: a role for Ca2+-induced Ca2+ release. J Physiol 539:15-23

Khimich D, Nouvian R, Pujol R, tom Dieck S, Egner A, Gundelfinger ED, Moser T (2005) Hair cell synaptic ribbons are essential for synchronous auditory signalling. Nature 434:889-894

Kiang NYS, Moxon EC (1974) Tails of tuning curves of auditory-nerve fibers. J. Acoust. Soc. Am. 55:620-630

Kiang NY (1965) Discharge patterns of single fibers in the cat's auditory nerve. Cambridge, MA: MIT Press.

Kiang NY, Moxon EC, Levine RA (1970) Auditory-nerve activity in cats with normal and abnormal cochleas In G. E. Wolstenholme & J. Knight, eds. Sensorineural Hearing Loss Great Britain: Churchill, p. 241-273.

Kim S, McNames J (2007) Automatic spike detection based on adaptive template matching for extracellular neural recordings. Journal of Neuroscience Methods 165:165-174

Klumpp R, Eady H (1956) Some measurements of interaural time difference thresholds. The Journal of the Acoustical Society of America 28:215-232

Koch C, Segev I (2000) The role of single neurons in information processing. Nat Neurosci 3:1171-1177

Kollmeier B, Gilkey RH (1990) Binaural forward and backward masking: Evidence for sluggishness in binaural detection. J. Acoust. Soc. Am. 87:1709-1719

Kraszewski K, Daniell L, Mundigl O, De Camilli P (1996) Mobility of Synaptic Vesicles in Nerve Endings Monitored by Recovery from Photobleaching of Synaptic Vesicle-Associated Fluorescence. J. Neurosci. 16:5905-5913

Krishna BS (2002) A Unified Mechanism for Spontaneous-Rate and First-Spike Timing in the Auditory Nerve. Journal of Computational Neuroscience 13:71-91

Kros CJ, Ruppersberg JP, Rüsch A (1998) Expression of a potassium current in inner hair cells during development of hearing in mice. Nature 394:281-284

Larsen E (2008) Slow modulation of cochlear response by the olivocochlear efferent system elicited by sustained noise or threshold elevation in the contralateral ear.

Lass Y, Abeles M (1975) Transmission of information by the axon: I. Noise and memory in the myelinated nerve fiber of the frog. Biological Cybernetics 19:61-67

Leal-Ortiz S, Waites CL, Terry-Lorenzo R, Zamorano P, Gundelfinger ED, Garner CC (2008) Piccolo modulation of Synapsin1a dynamics regulates synaptic vesicle exocytosis. J. Cell Biol. 181:831-846

Lenzi D, Crum J, Ellisman MH, Roberts WM (2002) Depolarization Redistributes Synaptic Membrane and Creates a Gradient of Vesicles on the Synaptic Body at a Ribbon Synapse. Neuron 36:649-659

Lenzi D, Runyeon JW, Crum J, Ellisman MH, Roberts WM (1999) Synaptic Vesicle Populations in Saccular Hair Cells Reconstructed by Electron Tomography. J. Neurosci. 19:119-132

Lesica NA, Grothe B (2008) Efficient Temporal Processing of Naturalistic Sounds. PLoS ONE 3:e1655

Li J, Young ED (1993) Discharge-rate dependence of refractory behavior of cat auditory-nerve fibers. Hearing Research 69:151-162

Liberman MC (1980) Morphological differences among radial afferent fibers in the cat cochlea: An electron-microscopic study of serial sections. Hearing Research 3:45-63

Liberman MC, Chesney C, Kujawa SG (1997) Effects of selective inner hair cell loss on DPOAE and CAP in carboplatin-treated chinchillas. Auditory Neuroscience 3:255-268

Liberman MC (1978) Auditory-nerve response from cats raised in a low-noise chamber. J. Acoust. Soc. Am. 63:442-455

Liberman MC (1990) Effects of chronic cochlear de-efferentation on auditory-nerve response. Hearing Research 49:209-223

Liberman MC, Dodds LW, Pierce S (1990) Afferent and efferent innervation of the cat cochlea: Quantitative analysis with light and electron microscopy. The Journal of Comparative Neurology 301:443-460

Liberman MC, Gao J, He DZZ, Wu X, Jia S, Zuo J (2002) Prestin is required for electromotility of the outer hair cell and for the cochlear amplifier. Nature 419:300-304

Lipscombe D, Helton TD, Xu W (2004) L-Type Calcium Channels: The Low Down. J Neurophysiol 92:2633-2641

Litovsky RY, Colburn HS, Yost WA, Guzman SJ (1999) The precedence effect. J. Acoust. Soc. Am. 106:1633-1654

Llano I, Gonzalez J, Caputo C, Lai FA, Blayney LM, Tan YP, Marty A (2000) Presynaptic calcium stores underlie large-amplitude miniature IPSCs and spontaneous calcium transients. Nat Neurosci 3:1256-1265

LoGiudice L, Sterling P, Matthews G (2008) Mobility and Turnover of Vesicles at the Synaptic Ribbon. J. Neurosci. 28:3150-3158

Lonsbury-Martin BL, Martin GK (1990) The clinical utility of distortion-product otoacoustic emissions. Ear Hear 11:144-54

Louage DHG, van der Heijden M, Joris PX (2004) Temporal Properties of Responses to Broadband Noise in the Auditory Nerve. J Neurophysiol 91:2051-2065

Ma WJ, Beck JM, Alex, Pouget R (2008) Spiking networks for Bayesian inference and choice. Current Opinion in Neurobiology 18:217-222

Ma WJ, Beck JM, Latham PE, Pouget A (2006) Bayesian inference with probabilistic population codes. Nature Neuroscience 9:1432-1438

Macpherson EA, Middlebrooks JC (2002) Listener weighting of cues for lateral angle: The duplex theory of sound localization revisited. J. Acoust. Soc. Am. 111:2219-2236

Mainen ZF, Sejnowski TJ (1995) Reliability of spike timing in neocortical neurons. Science 268:1503-6

Maison SF, Emeson RB, Adams JC, Luebke AE, Liberman MC (2003a) Loss of {alpha}CGRP Reduces Sound-Evoked Activity in the Cochlear Nerve. J Neurophysiol 90:2941-2949

Maison SF, Adams JC, Liberman MC (2003b) Olivocochlear Innervation in the Mouse: Immunocytochemical Maps, Crossed Versus Uncrossed Contributions, and Transmitter Colocalization. J Comp Neurol. 455:406–416

Mardia KV, Jupp PE (1999) Directional statistics. New York, NY: Wiley.

Matsubara A, Laake JH, Davanger S, Usami S, Ottersen OP (1996) Organization of AMPA Receptor Subunits at a Glutamate Synapse: A Quantitative Immunogold Analysis of Hair Cell Synapses in the Rat Organ of Corti. J. Neurosci. 16:4457-4467

Matthews G, Sterling P (2008) Evidence That Vesicles Undergo Compound Fusion on the Synaptic Ribbon. J. Neurosci. 28:5403-5411

McKay SM, Oleskevich S (2007) The role of spontaneous activity in development of the endbulb of Held synapse. Hearing Research 230:53-63

Melcher JR, Kiang NY (1996) Generators of the brainstem auditory evoked potential in cat III: identified cell populations. Hearing Research 93:52-71

Mennerick S, Matthews G (1996) Ultrafast Exocytosis Elicited by Calcium Current in Synaptic Terminals of Retinal Bipolar Neurons. Neuron 17:1241-1249

Merchan-Perez A, Liberman MC (1996) Ultrastructural differences among afferent synapses on cochlear hair cells: Correlations with spontaneous discharge rate. The Journal of Comparative Neurology 371:208-221

Moore BCJ, Glasberg BR, Plack CJ, Biswas AK (1988) The shape of the ear's temporal window. J. Acoust. Soc. Am. 83:1102-1116

Moser T, Beutner D (2000) Kinetics of exocytosis and endocytosis at the cochlear inner hair cell afferent synapse of the mouse. Proceedings of the National Academy of Sciences 97:883-888

Muresan V, Lyass A, Schnapp BJ (1999) The Kinesin Motor KIF3A Is a Component of the Presynaptic Ribbon in Vertebrate Photoreceptors. J. Neurosci. 19:1027-1037

Nadol JB (1990) Synaptic morphology of inner and outer hair cells of the human organ of Corti. Journal of Electron Microscopy Technique 15:187-196

Neher E (1998) Vesicle Pools and Ca2+ Microdomains: New Tools for Understanding Their Roles in Neurotransmitter Release. Neuron 20:389-399

Nicol MJ, Walmsley B (2002) Ultrastructural basis of synaptic transmission between endbulbs of Held and bushy cells in the rat cochlear nucleus. The Journal of Physiology 539:713-723

Nie L, Zhu J, Gratton MA, Liao A, Mu KJ, Nonner W, Richardson GP, Yamoah EN (2008) Molecular Identity and Functional Properties of a Novel T-Type Ca2+ Channel Cloned From the Sensory Epithelia of the Mouse Inner Ear. J Neurophysiol 100:2287-2299

Nouvian R, Beutner D, Parsons T, Moser T (2006) Structure and Function of the Hair Cell Ribbon Synapse. Journal of Membrane Biology 209:153-165

Ohlemiller KK, Gagnon PM (2004) Cellular correlates of progressive hearing loss in 129S6/SvEv mice. J Comp Neurol 469:377-90

Ohshima K, Hirai S, Nishida A, Hiramatsu K (1999) Ultrastructure and serotonin immunocytochemistry of the parietal-pineal complex in the Japanese grass lizard,Takydromus tachydromoides. Tissue and Cell 31:126-137

Oliphant TE (2007) Python for scientific computing. Computing in Science & Engineering 9:10-20

Oliver D, Knipper M, Derst C, Fakler B (2003) Resting Potential and Submembrane Calcium Concentration of Inner Hair Cells in the Isolated Mouse Cochlea Are Set by KCNQ-Type Potassium Channels. J. Neurosci. 23:2141-2149

Oliver D, Taberner AM, Thurm H, Sausbier M, Arntz C, Ruth P, Fakler B, Liberman MC (2006) The Role of BKCa Channels in Electrical Signal Encoding in the Mammalian Auditory Periphery. J. Neurosci. 26:6181-6189

Oliver DL, Beckius GE, Bishop DC, Kuwada S (1997) Simultaneous anterograde labeling of axonal layers from lateral superior olive and dorsal cochlear nucleus in the inferior colliculus of cat. The Journal of Comparative Neurology 382:215-229

Palmer AR, Evans EF (1980) Cochlear fibre rate--intensity functions: no evidence for basilar membrane nonlinearities. Hear Res 2:319-26

Palmer AR, Russell IJ (1986) Phase-locking in the cochlear nerve of the guinea-pig and its relation to the receptor potential of inner hair-cells. Hearing Research 24:1-15

Paninski L, Pillow J, Lewi J (2007) Statistical models for neural encoding, decoding, and optimal stimulus design. Prog Brain Res 165:493-507

Parsons TD, Sterling P (2003) Synaptic Ribbon: Conveyor Belt or Safety Belt? Neuron 37:379-382

Perkel DH, Gerstein GL, Moore GP (1967a) Neuronal Spike Trains and Stochastic Point Processes: I. The Single Spike Train. Biophys J. 7:391–418

Perkel DH, Gerstein GL, Moore GP (1967b) Neuronal Spike Trains and Stochastic Point Processes: II. Simultaneous Spike Trains. Biophys J. 7:419–440

Plack CJ, Moore BCJ (1990) Temporal window shape as a function of frequency and level. J. Acoust. Soc. Am. 87:2178-2187

Pouget A, Dayan P, Zemel RS (2003) Inference and computation with population codes. Annu Rev Neurosci 26:381-410

Prokop A, Meinertzhagen IA (2006) Development and structure of synaptic contacts in Drosophila. Seminars in Cell & Developmental Biology 17:20-30

Quandt F, Davis F (1992) Action potential refractory period in axonal demyelination: a computer simulation. Biological Cybernetics 67:545-552

Ramakrishnan NA, Drescher MJ, Drescher DG (2009) Direct Interaction of Otoferlin with Syntaxin 1A, SNAP-25, and the L-type Voltage-gated Calcium Channel CaV1.3. J. Biol. Chem. 284:1364-1372

Rao-Mirotznik R, Harkins AB, Buchsbaum G, Sterling P (1995) Mammalian rod terminal: Architecture of a binary synapse. Neuron 14:561-569

Rao-Mirotznik R, Buchsbaum G, Sterling P (1998) Transmitter Concentration at a Three-Dimensional Synapse. J Neurophysiol 80:3163-3172

Rea R, Li J, Dharia A, Levitan ES, Sterling P, Kramer RH (2004) Streamlined Synaptic Vesicle Cycle in Cone Photoreceptor Terminals. Neuron 41:755-766

Rhode WS, Smith PH (1986) Encoding timing and intensity in the ventral cochlear nucleus of the cat. J Neurophysiol 56:261-286

Rhode WS, Greenberg S (1992) Physiology of the cochlear nuclei In The mammalian auditory pathway: Neuroanatomy Springer Handbook of Auditory Research. New York, NY: Springer-Verlag, p. 94-152.

Richter K, Langnaese K, Kreutz MR, Olias G, Zhai R, Scheich H, Garner CC, Gundelfinger ED (1999) Presynaptic cytomatrix protein Bassoon is localized at both excitatory and inhibitory synapses of rat brain. The Journal of Comparative Neurology 408:437-448

Roberts WM, Jacobs RA, Hudspeth AJ (1990) Colocalization of ion channels involved in frequency selectivity and synaptic transmission at presynaptic active zones of hair cells. J Neurosci 10:3664-84

Rodriguez-Contreras A, Yamoah EN (2001) Direct measurement of single-channel Ca2+ currents in bullfrog hair cells reveals two distinct channel subtypes. J Physiol 534:669-689

Rose JE, Brugge JF, Anderson DJ, Hind JE (1967) Phase-locked response to low-frequency tones in single auditory nerve fibers of the squirrel monkey. J Neurophysiol 30:769-93

Roth GL, Aitkin LM, Andersen RA, Merzenich MM (1978) Some features of the spatial organization of the central nucleus of the inferior colliculus of the cat. J Comp Neurol 182:661-80

Roux I, Safieddine S, Nouvian R, Grati M, Simmler M, Bahloul A, Perfettini I, Gall ML, Rostaing P, Hamard G, Triller A, Avan P, Moser T, Petit C (2006) Otoferlin, Defective in a Human Deafness Form, Is Essential for Exocytosis at the Auditory Ribbon Synapse. Cell 127:277-289

Ruggero MA, Rich NC (1991) Furosemide alters organ of corti mechanics: evidence for feedback of outer hair cells upon the basilar membrane. J Neurosci 11:1057-67

Russell IJ, Sellick PM (1978) Intracellular studies of hair cells in the mammalian cochlea. J Physiol 284:261-90

Ryugo DK, Sento S (1991) Synaptic connections of the auditory nerve in cats: Relationship between endbulbs of held and spherical bushy cells. The Journal of Comparative Neurology 305:35-48

Sachs MB, Voigt HF, Young ED (1983) Auditory nerve representation of vowels in background noise. J Neurophysiol 50:27-45

Sachs MB, Abbas PJ (1974) Rate versus level functions for auditory-nerve fibers in cats: tone-burst stimuli. J. Acoust. Soc. Am. 56:1835-1847

Sachs MB, Winslow RL, Sokolowski BH (1989) A computational model for rate-level functions from cat auditory-nerve fibers. Hearing Research 41:61-69

Safieddine S, Wenthold RJ (1999) SNARE complex at the ribbon synapses of cochlear hair cells: analysis of synaptic vesicle- and synaptic membrane-associated proteins. European Journal of Neuroscience 11:803-812

Schalk TB, Sachs MB (1980) Nonlinearities in auditory-nerve fiber responses to bandlimited noise. J. Acoust. Soc. Am. 67:903-913

Schmitz F, Königstorfer A, Südhof TC (2000) RIBEYE, a Component of Synaptic Ribbons: A Protein's Journey through Evolution Provides Insight into Synaptic Ribbon Function. Neuron 28:857-872

Schoch S, Gundelfinger E (2006) Molecular organization of the presynaptic active zone. Cell and Tissue Research 326:379-391

Schwartz I (1992) The superior olivary complex and lateral lemniscal nuclei In D. Webster, A. N. Popper, & R. R. Fay, eds. The mammalian auditory pathway: Neuroanatomy New York, NY: Springer-Verlag.

Sejnowski TJ, Yodlowski ML (1982) A freeze-fracture study of the skate electro receptor. Journal of Neurocytology 11:897-912

Sewell WF (1984a) The relation between the endocochlear potential and spontaneous activity in auditory nerve fibres of the cat. J Physiol. 347:685–696

Sewell WF (1984b) The effects of furosemide on the endocochlear potential and auditory-nerve fiber tuning curves in cats. Hear Res 14:305-14

Sewell WF (1984c) Furosemide selectively reduces one component in rate-level functions from auditory-nerve fibers. Hearing Research 15:69-72

Siegel JH (1992) Spontaneous synaptic potentials from afferent terminals in the guinea pig cochlea. Hearing Research 59:85-92

Sjostrand FS (1958) Ultrastructure of retinal rod synapses of the guinea pig eye as revealed by three-dimensional reconstructions from serial sections. J Ultrastruct Res 2:122-70

Skinner LJ, Enee V, Beurg M, Jung HH, Ryan AF, Hafidi A, Aran J, Dulon D (2003) Contribution of BK Ca2+-Activated K+ Channels to Auditory Neurotransmission in the Guinea Pig Cochlea. J Neurophysiol 90:320-332

Smith PH, Rhode WS (1987) Characterization of HRP-labeled globular bushy cells in the cat anteroventral cochlear nucleus. The Journal of Comparative Neurology 266:360-375

Spanfo S, Silletta MG, Colanzi A, Alberti S, Fiucci G, Valente C, Fusella A, Salmona M, Mironov A, Luini A, Corda D (1999) Molecular Cloning and Functional Characterization of Brefeldin A-ADP-ribosylated Substrate. A Novel Protein Involved in the Maintenance of the Golgi Structure. J. Biol. Chem. 274:17705-17710

Spassova, Avissar, Furman AC, Crumling, Saunders, Parsons (2004) Evidence That Rapid Vesicle Replenishment of the Synaptic Ribbon Mediates Recovery from Short-Term Adaptation at the Hair Cell Afferent Synapse. JARO - Journal of the Association for Research in Otolaryngology 5:376-390

Spirou G, Rager J, Manis P (2005) Convergence of auditory-nerve fiber projections onto globular bushy cells. Neuroscience 136:843-863

Spitzer MW, Semple MN (1995) Neurons sensitive to interaural phase disparity in gerbil superior olive: diverse monaural and temporal response properties. J Neurophysiol 73:1668-1690

Spoendlin H (1969) Innervation patterns in the organ of corti of the cat. Acta Otolaryngol 67:239-54

Spoendlin H (1972) Innervation densities of the cochlea. Acta Otolaryngol 73:235-48

Spoendlin H, Schrott A (1988) The spiral ganglion and the innervation of the human organ of Corti. Acta Otolaryngol 105:403-10

Spongr VP, Flood DG, Frisina RD, Salvi RJ (1997) Quantitative measures of hair cell loss in CBA and C57BL/6 mice throughout their life spans. J. Acoust. Soc. Am. 101:3546-3553

Stamataki S, Francis HW, Lehar M, May BJ, Ryugo DK (2006) Synaptic alterations at inner hair cells precede spiral ganglion cell loss in aging C57BL/6J mice. Hearing Research 221:104-118

Stefanov-Wagner I (1994) EPL spike trigger.

Sterling P, Freed M, Smith R (1988) Architecture of rod and cone circuits to the on-beta ganglion cell. J. Neurosci. 8:623-642

Sterling P (2004) How retinal circuits optimize the transfer of visual information In L. M. Chalupa & J. S. Werner, eds. The visual neurosciences Cambridge, MA: MIT Press, p. 243-268.

Sterling P, Matthews G (2005) Structure and function of ribbon synapses. Trends in Neurosciences 28:20-29

Stevens CF, Tsujimoto T (1995) Estimates for the pool size of releasable quanta at a single central synapse and for the time required to refill the pool. Proc Natl Acad Sci U S A. 92:846–849

Sudhof TC (2004) The synaptic vesicle cycle. Annu Rev Neurosci 27:509-47

Sumner CJ, Meddis R, Winter IM (2009) The role of auditory nerve innervation and dendritic filtering in shaping onset responses in the ventral cochlear nucleus. Brain Res. 1247:221–234

Szabo T, Wersäll J (1970) Ultrastructure of an electroreceptor (mormyromast) in a mormyrid fish, Gnathonemus petersii. II. Journal of Ultrastructure Research 30:473-490

Szamier RB, Wachtel AW (1970) Special cutaneous receptor organs of fish: VI. Ampullary and tuberous organs of Hypopomus. Journal of Ultrastructure Research 30:450-471

Taberner AM, Liberman MC (2005) Response Properties of Single Auditory Nerve Fibers in the Mouse. J Neurophysiol 93:557-569

Tao HW, Poo M (2001) Retrograde signaling at central synapses. Proceedings of the National Academy of Sciences of the United States of America 98:11009-11015

Temchin AN, Recio-Spinoso A, van Dijk P, Ruggero MA (2005) Wiener Kernels of Chinchilla Auditory-Nerve Fibers: Verification Using Responses to Tones, Clicks, and Noise and Comparison With Basilar-Membrane Vibrations. J Neurophysiol 93:3635-3648

Thiers F, Nadol J, Liberman M (2008) Reciprocal Synapses Between Outer Hair Cells and their Afferent Terminals: Evidence for a Local Neural Network in the Mammalian Cochlea. JARO - Journal of the Association for Research in Otolaryngology 9:477-489

Thurm H, Fakler B, Oliver D (2005) Ca2+-independent activation of BKCa channels at negative potentials in mammalian inner hair cells. J Physiol 569:137-151

Tiesinga P, Fellous J, Sejnowski TJ (2008) Regulation of spike timing in visual cortical circuits. Nat Rev Neurosci 9:97-107

Tritsch NX, Yi E, Gale JE, Glowatzki E, Bergles DE (2007) The origin of spontaneous activity in the developing auditory system. Nature 450:50-55

Usukura J, Yamada E (1987) Ultrastructure of the synaptic ribbons in photoreceptor cells of Rana catesbeiana revealed by freeze-etching and freeze-substitution. Cell and Tissue Research 247:483-488

Voets T, Neher E, Moser T (1999) Mechanisms Underlying Phasic and Sustained Secretion in Chromaffin Cells from Mouse Adrenal Slices. Neuron 23:607-615

Vollrath L, Spiwoks-Becker I (1996) Plasticity of retinal ribbon synapses. Microscopy Research and Technique 35:472-487

Wakeford OS, Robinson DE (1974) Lateralization of tonal stimuli by the cat. J. Acoust. Soc. Am. 55:649-652

Wallach H, Newman E, Rosenzweig M (1949) The precedence effect in sound localization. Am J Psychol 62:315-36

Wang Y, Okamoto M, Schmitz F, Hofmann K, Sudhof TC (1997) Rim is a putative Rab3 effector in regulating synaptic-vesicle fusion. Nature 388:593-598

Wangemann P (2002) K+ cycling and the endocochlear potential. Hearing Research 165:1-9

Webster DB, Trune DR (1982) Cochlear nuclear complex of mice. American Journal of Anatomy 163:103-130

Westerman LA, Smith RL (1984) Rapid and short-term adaptation in auditory nerve responses. Hearing Research 15:249-260

Wiederhold ML, Kiang NY (1970) Effects of electric stimulation of the crossed olivocochlear bundle on single auditory-nerve fibers in the cat. J Acoust Soc Am 48:950-65

Wightman FL, Kistler DJ (1992) The dominant role of low-frequency interaural time differences in sound localization. J. Acoust. Soc. Am. 91:1648-1661

Winslow RL, Sachs MB (1988) Single-tone intensity discrimination based on auditory-nerve rate responses in backgrounds of quiet, noise, and with stimulation of the crossed olivocochlear bundle. Hearing Research 35:165-189

Wörgötter F, Daunicht WJ, Eckmiller R (1986) An on-line spike form discriminator for extracellular recordings based on an analog correlation technique. Journal of Neuroscience Methods 17:141-151

Yin TC, Chan JC (1990) Interaural time sensitivity in medial superior olive of cat. J Neurophysiol 64:465-488

Young ED, Robert JM, Shofner WP (1988) Regularity and latency of units in ventral cochlear nucleus: implications for unit classification and generation of response properties. J Neurophysiol 60:1-29

Young ED, Barta PE (1986) Rate responses of auditory nerve fibers to tones in noise near masked threshold. J. Acoust. Soc. Am. 79:426-442

Youssoufian M, Couchman K, Shivdasani MN, Paolini AG, Walmsley B (2008) Maturation of auditory brainstem projections and calyces in the congenitally deaf (dn/dn) mouse. The Journal of Comparative Neurology 506:442-451

Yu Y, Zuo J (2009) The Practical Use of Cre and loxP Technologies in Mouse Auditory Research In Auditory and Vestibular Research , p. 87-102. Available at: http://dx.doi.org/10.1007/978-1-59745-523-7_6.

Zenisek D, Steyer JA, Almers W (2000) Transport, capture and exocytosis of single synaptic vesicles at active zones. Nature 406:849-854

Zenisek D (2008) Vesicle association and exocytosis at ribbon and extraribbon sites in retinal bipolar cell presynaptic terminals. Proc Natl Acad Sci U S A

Zenisek D, Davila V, Wan L, Almers W (2003) Imaging Calcium Entry Sites and Ribbon Structures in Two Presynaptic Cells. J. Neurosci. 23:2538-2548

Zenisek D, Horst NK, Merrifield C, Sterling P, Matthews G (2004) Visualizing Synaptic Ribbons in the Living Cell. J. Neurosci. 24:9752-9759

Zhang X, Carney LH (2005) Response properties of an integrate-and-fire model that receives subthreshold inputs. Neural computation 17:2571-2601

Zheng QY, Johnson KR, Erway LC (1999) Assessment of hearing in 80 inbred strains of mice by ABR threshold analyses. Hearing Research 130:94-107

Zidanic M, Fuchs PA (1995) Kinetic analysis of barium currents in chick cochlear hair cells. Biophys. J. 68:1323-1336